Exploration of Novel Applications for Optical Communications using Silicon Nanophotonics

Asif Ahmed

Submitted in partial fulfillment of the
requirements for the degree of
Doctor of Philosophy
in the Graduate School of Arts and Sciences

COLUMBIA UNIVERSITY

2018

Abstract

Exploration of Novel Applications for Optical Communications using Silicon Nanophotonics

Asif Ahmed

Silicon photonics is considered to have the potential to enable future communication systems with optical input-outputs to circumvent the shortcomings of electronics. Today silicon is the material of choice for photonic and optoelectronic circuits, mainly due to its excellent material properties, established processing technology, low-cost, compact device footprint, and high-density integration. From sensing and detection to computing and communications, silicon photonics has advanced remarkably in the last couple of decades and found numerous applications.

This thesis work focusses on three novel applications of silicon photonics for optical communications. The first application is the design and demonstration of a differential phase shift keying (DPSK) demodulator circuit using a ring resonator. DPSK-based transceivers are being actively considered for short-haul optical communication systems due to their advantages in terms of high extinction ratio, dispersion tolerance, and improved sensitivity. The ring resonator utilizes the concept of coherent perfect absorption and results into a compact demodulator circuit that can be easily integrated into an all-optical system. The next application involves a nonlinear optical process, namely, four wave mixing (FWM) inside a silicon nanowire. For FWM to occur efficiently, phase matching between the real propagation constants of all the frequency components is a key requirement. However, this condition cannot be easily satisfied in integrated optics semiconductor platforms. We propose an altogether new approach to achieve signal gain within the context of non-Hermitian photonics and parity-time (PT) symmetry and show that the phase matching criterion is not necessary to achieve efficient nonlinear interactions. Instead by introducing losses only to the idler components while leaving the pump and signal waves intact, we analyze a coupled-wave system of silicon nanowires using finite difference time domain technique and find that signal gain is indeed possible in such a system, irrespective of the fulfillment of the phase-matching condition. The final application of silicon photonics in this thesis is the engineering of zero group velocity dispersion (GVD) point in the C-band of communication channel. The problem of pulse broadening due to chromatic dispersion is becoming an increasingly important factor for signal degradation. We propose a hybrid silicon/plasmonic waveguide that can change the zero-GVD point by altering the geometry and material of the waveguide components. In addition, such hybrid system also has the potential to transmit both optical and electronic signals along the same circuitry.

Contents

List of Figures

List of Tables

Acknowledgements

At this stage of my life when I am soon to finish my PhD, I can't help but think that this has been a collective effort, rather than my single endeavor. From the very first day that I started to attend in Columbia University till the very last day, I always felt the help, support, guidance, and appreciation of so many people.

My completion of this thesis could not have been accomplished without the ceaseless supervision and support of Professor Richard M. Osgood, Jr. I consider myself very lucky to have a thesis supervisor like him. Not only he guided me through the last four years, but also he did so in a very amiable manner. I have never met anyone who appreciated my efforts and encouraged me in going forward in such a positive way. I earnestly hope to keep in touch with him in the days to come.

Next I would like to acknowledge all my group members. In the first year of my graduate life it was Dr. Xiang Meng, himself a graduate student then, who was my mentor. I learnt the nooks and crannies of RSoft (the photonic simulation software that I used in my thesis) from him. I can't remember how many times I have asked him detailed questions not only about RSoft, but also about many academic problems. And he never failed to reply. Now when he's working as an Adjunct Professor in Columbia, he still has the time to help me in my research in any way he can. None of my research work would be complete without the constant help from Dr. Jerry Dadap. As a research scientist in our group, he was associated with all of our projects, but he always managed time to help each and every one of us individually. He helped me in many of my calculations and simulations, and interpretation of results. When Prof. Osgood retired and moved back to Boston, Jerry became my first immediate point of contact about my research, and he is still helping me even now by proof-reading my papers. In one of my project works, Hao Yang was an equal contributor. We used to go to Brookhaven National Laboratories for fabrication, and United States Military Academy for experimentation. It was not only fun working with him, but also instructive through all the brain-storming about the project. I would also like to think all other current and previous group members: Yi Lin, Peter Bullen, Jacob Rothenberg, and Wencan Jin who were part of our group through some or all the years I was at Columbia.

In 4 years of my PhD life, I also came across people outside Columbia. My heartiest gratitude to Dr. Brian Souhan who was working as an assistant professor in United States Military Academy when we decided to move forward with experimentation of one of our research projects. He openly invited us to use the laboratories over there. Not only that, edge coupling of fiber to a chip is almost an “art” that he taught us over there. On that note, I would also like to thank Lt. Col. Kirk Ingold for allowing us to work on their lab. In many simulations, design and post-analysis of that particular work, it was Dr. Richard Grote whom advice I first sought. Although he was working at University of Pennsylvania then, the amount of help that he gave remotely through email is unimaginable.

Collaboration with other groups is a common strait in PhD life. It was Dr. Christine P. Chen from whom I had the first learning experience of any kind of experimentation. While Brian taught me edge-coupling, it was Christine who taught me grating-coupling! To characterize a first prototype of one of our chip, she gave us her constant help and support in their lab. When she went to work at Intel after graduation, it was Nathan C. Abrams who started working with us in the next step of that project. He was not only resourceful in coming up with many equipment that we need, but also instrumental in setting up the experiment. I would also like to thank their supervisor Professor Keren Bergman for allowing us to use her laboratory. She was also one of my Integrative Graduate Education and Research Traineeship (IGERT) supervisor. Next, I acknowledge Professor Ramy El-Ganainy of Michigan Technological University for coming up with the fundamental idea of another of my research project. Our collaboration with his group led to many interesting and novel results. For a graduate student, funding is probably one of the important things in life. I am grateful to IGERT program at Columbia, led by Professor Irving Herman, for my academic and financial support for two years of my graduate life.

Outside research I have learnt so many things from the courses that I took at Columbia. I have known many basic principles in my research field from these courses. I also took courses outside my field which I must say helped in my job interview. Therefore, I would like to thank all my teachers, not only from Columbia, but also from Bangladesh University of Engineering and Technology, where I learnt all the ABC about electrical engineering.

Finally, my deepest gratitude to my caring, loving, and supportive family. Your encouragement when the times got rough is much appreciated and duly noted. To my parents, thank you for teaching me the value of hard-ship and honesty. To my sisters, thank you for being there for me always. To my friends, thank you for being a source of fun and excitement. To all my relatives, thank you for making me understand the beauty of family. And last but definitely not the least, thank you to my ever-supportive and ever-loving wife Kashfia Quader Khan. Being apart from her was hard for the last four years. But I know it was always the happy and meaningful future that kept us strong.

Dedication

To my family.

"You don't choose your family. They are God's gift to you, as you are to them."

- Desmond Tutu

"Rejoice with your family in the beautiful land of life!"

- Albert Einstein

Chapter 1

Introduction

Silicon photonics is the optical equivalent of silicon microelectronics. It entails the use of photons to transmit, modulate, process and detect information more efficiently than electrical signals. Excellent material properties, low-cost manufacturing, high yields and unified on-chip integration with electronics as a result of using conventional silicon-integrated-circuit processes are the most crucial benefits of silicon photonics [1]. The novel hypothesis for silicon based photonic and optoelectronic integrated circuits is that these chip-scale networks, after going through careful design steps, will operate at a wavelength anywhere within a very broad spectral range of $1.2 - 100$ μm [2]. Silicon photonics dense wavelength division multiplexing (DWDM) brings an additional spatial dimension to electronics, as it permits many wavelength data channels to coexist spatially, with practically no electromagnetic cross talk or power dissipation among various wavelength channels [3]. Therefore, the field of silicon photonics has grown significantly in recent years and turned out to be progressively diverse in its applications. Today, silicon-based platforms support the realization of a wide variety of applications, including but not limited to, photonic interconnects [4], telecommunication [5], signal processing [6], switched networks [7], imaging [8], displays [9], radio frequecny/wireless photonics [10], medical diagnosis [11], spectrometer-on-a-chip [12], photonic sensing of chemical/biological/physical variables [13], neural networks [14], solar cells [15], and optical logic [16].

1.1 Silicon as a Photonic Material

Silicon (Si) is the second most (after oxygen) abundant element on earth. It has a simple cubic crystal structure that can be used to make wafers with a staggering degree of purity without defects. Such inexpensive and high-quality silicon wafers are the basis of integrated circuit (IC) industry that has become pervasive and can be found in virtually every day-to-day appliance and device in the modern world. In addition, silicon's large thermal conductivity, hardness, and low density are useful in semiconductor devices. For photonic platform consideration, silicon has a high refractive index of 3.476 at 1550 nm and is transparent to infrared light with wavelengths above approximately 1100 nm [17]. Furthermore, silicon's high-quality oxide, SiO_2, offers one of the major advantages of silicon over germanium and other semiconductors for integrated circuits. It has a relatively low refractive index of 1.45 at 1550 nm and optical transparency in the telecommunication wavelengths. Therefore, silicon, along with its oxide, constitute a very high index difference that results into high confinement of propagating light inside silicon waveguide with oxide cladding, stimulating the downscaling of device footprint to the order of submicron and nanometer sizes [18].

Silicon has an indirect bandgap structure. Thus, free electrons tend to recombine with holes by emitting phonons (heat) rather than photons, resulting in extremely poor internal quantum efficiency for light emission in silicon. In order to achieve stimulated emission, energy and momentum must be conserved for optical transitions. This conservation can be easily realized in direct bandgap materials where the lowest energy point of conduction band and highest energy point of valence band line up vertically along the wave vector axis, resulting in rapid and efficient emission of photons through electron-hole pair recombination (EHR), as illustrated in Fig. 1.1(a) [18]. On the other hand, in an indirect bandgap material

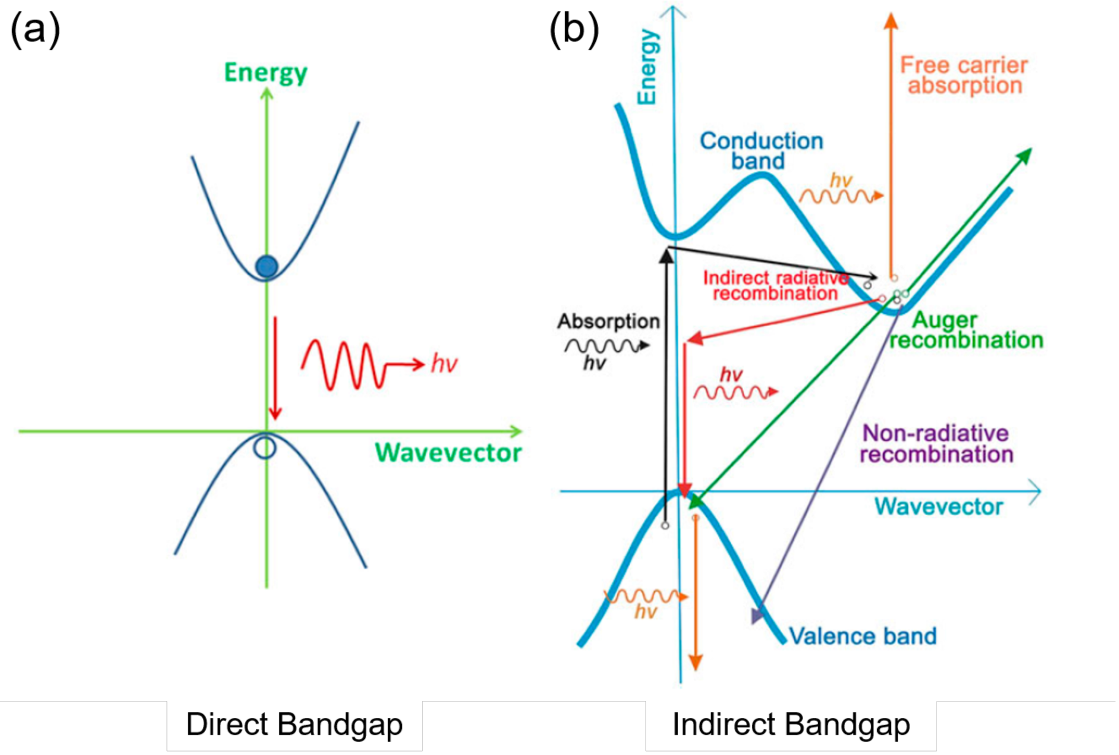

Figure 1.1: Schematic energy band diagram of (a) a direct bandgap material, (such as GaAs) (b) an indirect bandgap material (such as Si). In (b), absorption of photon elevates an electron from the valence band to the conduction band from where it shifts to the lowest valley of the conduction band through the assistance of a phonon. Two recombination processes can occur in this stage: (1) non-radiative recombination, (2) Auger recombination. In addition, the electron can also experience free carrier absorption [18].

such as silicon (Fig. 1.1(b)), free electrons stabilize in the lower valley of the conduction band, that is not vertically aligned with the highest peak of valence band. Therefore, to achieve stimulated emission, phonon absorption is required to satisfy the momentum conservation condition and to emit photons; the probability of which is much smaller than that of a single-step recombination process in direct bandgap materials. Typically, two kinds of non-radiation processes are associated with EHR in a silicon material: (i) Auger recombination (Excitation of a free electron to a higher energy level by absorbing the released energy from an EHR) and (ii) Free-carrier absorption (Elevation of free electrons in conduction band to higher energy levels by absorbing photons). Therefore, in order to realize a silicon-based light source, various methods have been exploited to overcome the material limitation of silicon, namely its indirect bandgap. Some of the methods include hybrid integration of III-V semiconductor [19] or germanium [20] gain medium with a silicon platform and silicon lasers and amplifiers by using stimulated Raman scattering [21]. The motivation behind this is that if one can find methods to achieve one's goals using silicon with CMOS processes, it would be difficult for other technologies to compete.

In the case of photodetector, where incident photons are absorbed and free electron-hole pairs are generated, silicon can be an excellent material as long as the energy of incident photons are equal to or greater than that of the bandgap, i.e., $E_{\text{photon}} \geq E_g$. However, due to the material transparency at the communication wavelength range, optical detection on the silicon platform requires the incorporation of other active materials, such as group III-V materials [22, 23] and germanium [24, 25]. While III-V materials usually offer low dark current, high speed, and high sensitivity for photodetection, germanium, on the other hand, not only exhibits strong photon absorption in the entire communication wavelength range, but also is highly compatible with Si CMOS fabrication processes, thus enabling monolithic integration of Ge/SiGe photodetectors [26]. Recently, an all-Si ion-implanted p-i-n waveguide photodetector has also been demonstrated without any other material incorporated into the device [27, 28].

Another significant feature in photonic circuits is nonlinearity; which essentially corresponds to such optical medium where the dielectric polarization responds nonlinearly to the electric field of the light. Nonlinear optics is also highly realistic, with hundreds of applications being pursued in the commercial arena, including wavelength converters for telecommunications, optical signal processing, and optical switching [29]. The traditional linear electro-optical effect, or Pockels effect, is absent in pure silicon since it has a centrosymmetric crystal structure [30]. Although several novel techniques have been applied to instigate Pockels effect in crystalline silicon, e.g., applying an asymmetric strain [31] and utilizing plasma dispersion effect for modulation [32], the susceptibility value is still lower than that obtained in conventional lithium niobate ($LiNbO_3$) platforms [18]. However, silicon does have an extremely large third-order nonlinear optical susceptibility in the near infrared (about 34 orders of magnitude larger than that of silica) [30]. This large cubic nonlinearity in silicon, along with its strong optical confinement, leads to further enhancement of the effective optical nonlinearity. Consequently, many nonlinear optical processes occur in silicon photonics as summarized in Fig. 1.2.

Based on such aforementioned material properties and cost effectiveness, it can be surmised that silicon photonics is in a superlative status to play a major role in the next generation devices and systems.

1.2 History of Silicon Photonics

There have been predictions of an optical superchip integrating various optical components for light generation, modulation, manipulation, amplification, and detection ever since the earliest research on optical circuits in the 1970s [33]. The early research was focussed primarily on $LiNbO_3$ due to its large electro-optic coefficient and III-V semiconductors due to the relative ease of laser fabrication [34]. However, as mentioned previously, the potential integration with electronics in a cost effective manner and utilization of the CMOS fabrication infrastructure eventually led to the investigation of silicon photonic circuits in the mid 1980s. While the IC industry relied mostly on crystalline silicon wafers, in the late 1980s and mid 1990s, a new type of wafer, silicon-on-insulator (SOI), was fabricated by three novel approaches. They were separation by implanted oxygen (SIMOX) [35], bonded and etch-back SOI (BESOI) [36], and smart cut [37]. The SOI substrate is ideal for waveguides since it can highly confine light within the top silicon layer, and has favorable thermal and electrical properties [38].

In 1993, Soref [39] presented a concept of a silicon opto-electronic integrated circuit (OEIC) ‘superchip’ using silicon optical waveguides, as shown in Fig. 1.3. This superchip integrated opto-electronic devices such as Si bipolar, BiCMOS, and SiGe/Si heterobipolar

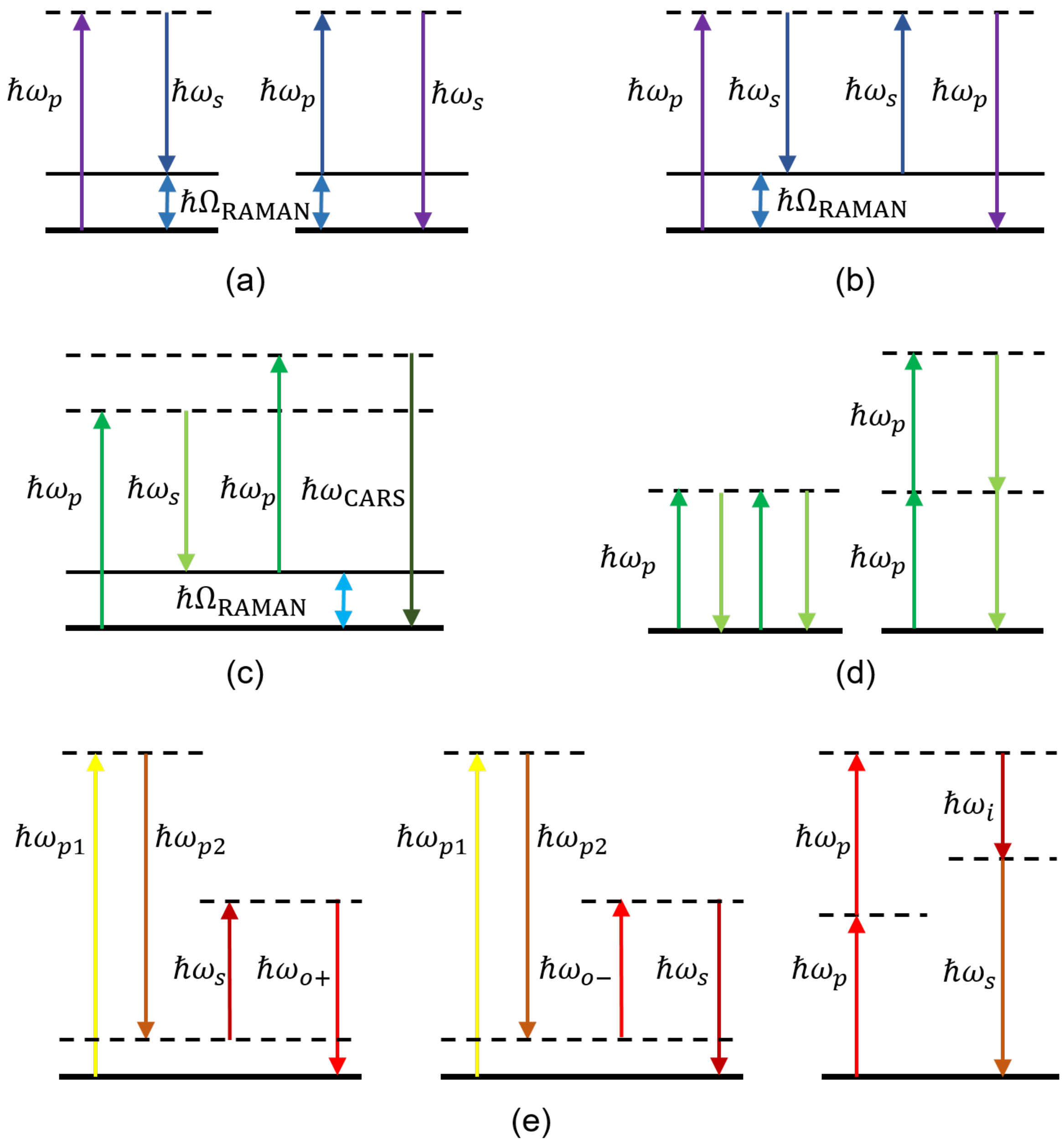

Figure 1.2: Relevant nonlinear optical processes in Si photonics: (a) spontaneous Raman (Stokes and anti-Stokes) emission, (b) stimulated Raman emission, (c) Coherent Anti-Stokes Raman Scattering, (d) Kerr effect and Two-Photon Absorption, and (e) Four Wave Mixing [29].

transistors all onto a common substrate. However, advances in OEIC were hampered due to inefficient silicon light emission. Over the period from 1993 to 2003, silicon photonics progressed in a relatively small pace [18]. The pace quickened since 2004 due to investment

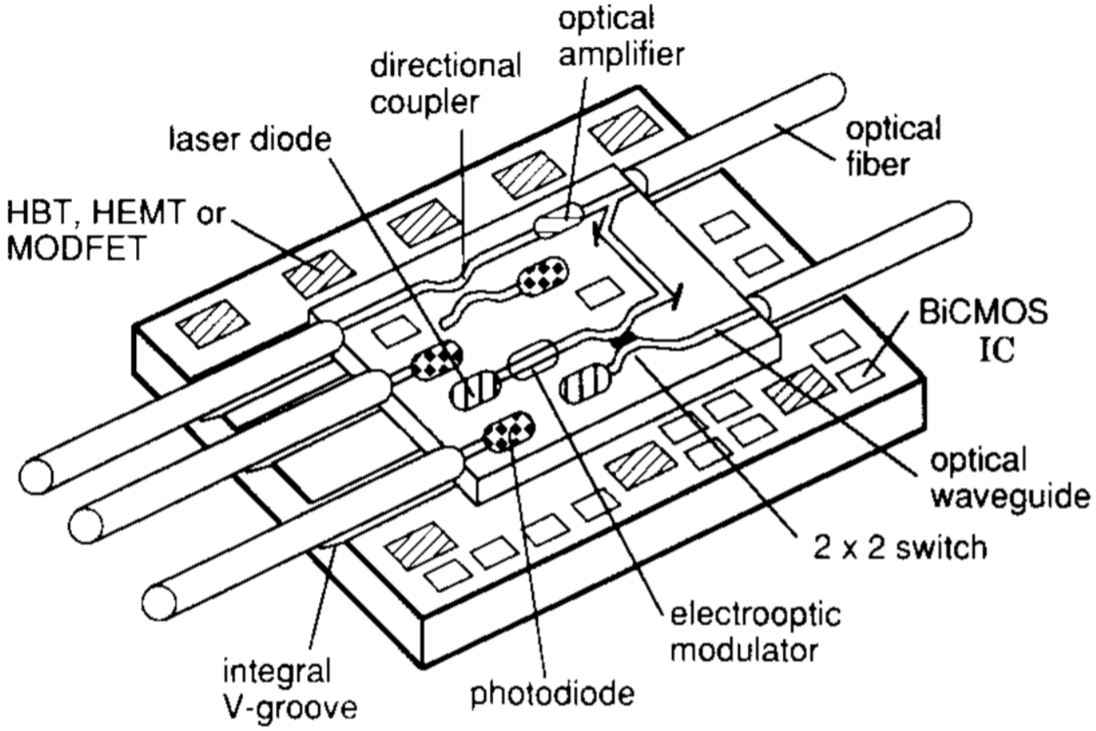

Figure 1.3: Early example of a silicon-based optoelectronic integrated circuits superchip [39].

by industry and government [2]. From this time research efforts have been put towards not only discrete photonic devices, but also hybrid integration techniques.

On the subsequent sections, the development of several building blocks of the silicon photonic circuit, which are essential to this thesis work, is summarized briefly.

1.2.1 Waveguides

The waveguide is one of the most fundamental building blocks in silicon photonic circuits. For waveguides to be useful in photonic circuits, they need to be single-mode, polarization independent and producible using conventional processes [3]. The first silicon waveguide was reported in the 1980s [40] (Fig. 1.4(a)). Since it was a silicon-on-silicon rib waveguide, where the substrate and the core are both made of silicon with different doping densities, the refractive index step between the substrate and the guiding silicon layer was very small, around 0.01, resulting in low light confinement and a large propagation loss of 15 dB/cm at

1.3 μm [40]. As mentioned previously, the SOI platform was introduced in the late 1980s and was suitable for waveguide applications in the communication wavelength range due to their low substrate leakage radiation loss. The early waveguides had a width and height of several microns, e.g., the rib waveguide pictured in Fig. 1.4(a) has a width of 10 μm and a height of 7 μm. Further reduction of waveguide dimension was possible after introducing strip or channel waveguides in the 1990s [41]. The strip waveguide in Fig. 1.4(b) has a width of 450 nm and a height of 220 nm [42].

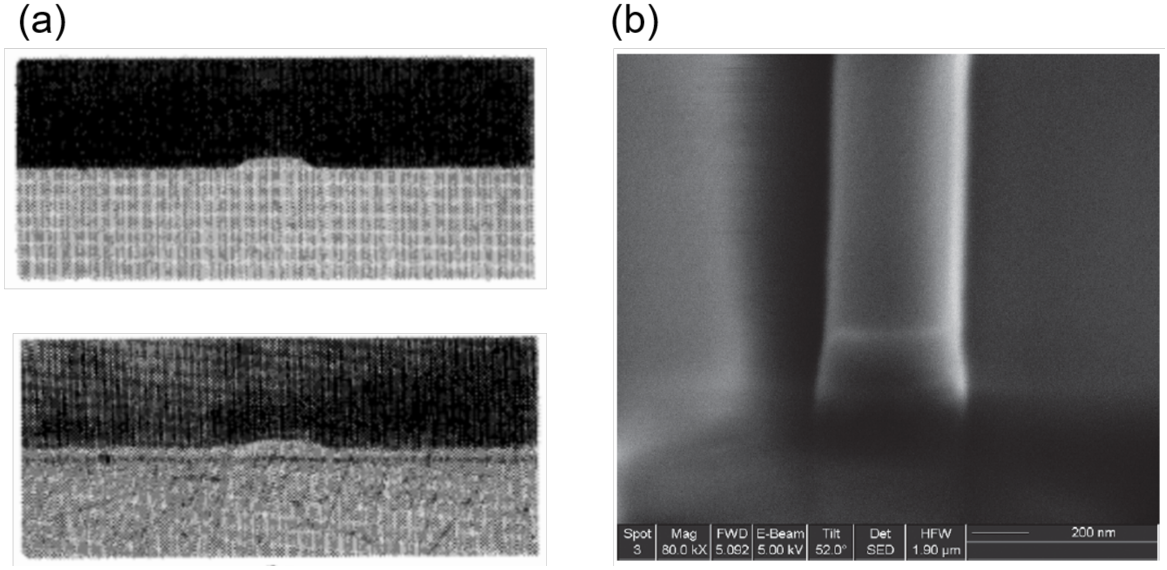

Figure 1.4: (a) Photomicrograph of a rib channel waveguide before (top) and after (bottom) acid etch [40]. (b) Scanning electron microscope cross-sectional image of a strip waveguide [42].

Although SOI waveguides have drawbacks in terms of large waveguide birefringence [43] and temperature sensitivity [18], several novel techniques like stress modification in the upper cladding layer [44] and subwavelength gratings [45] have been demonstrated to tackle the issues of birefringence and temperature sensitivity, respectively. With these fundamental issues resolved, the research on silicon photonics moved towards more complex circuits and devices.

1.2.2 Ring Resonators

Optical ring resonators have showed great potential as fundamental building blocks for a multitude of applications in photonics. In a simple sense, a ring resonator consists of an ordinary curved waveguide that channels light in a closed loop. But in general, the loop can take the form of other closed shapes, such as a disk, racetrack, or ellipse. Placement of a microresonator near a waveguide enables access to modes of the resonant cavity through evanescent coupling a phenomena analogous to tunneling in solid-state physics [46]. Wavelengths of an optical signal propagating inside a waveguide are resonant with the cavity if its effective circumference supports an integer number of wavelengths. These wavelengths can then experience an increased intensity due to build up inside the resonator. A second waveguide coupled to the ring allows extraction of the power from the resonator. Since wavelengths that do not resonate with the ring circumvent it altogether, ring resonators ,at their most basic level, act as a spectral filter. Although functionally similar to FabryPerot resonators, ring resonators have several advantages [46]: 1) Compatibility with monolithic microfabrication technologies due to their planar architecture, 2) No multilayer or distributed Bragg reflectors required to achieve high finesse, 3) No need for costly Faraday circulators since the injected, transmitted, and reflected waves occupy spatially distinct channels, 4) Integration of many devices on the same chip due to their small dimensions or footprint.

The first report on a curved pathway for acoustic waves was reported in 1910 by Lord Rayleigh in 1910 as “whispering gallery” [47]. In the optical domain, Marcatili first proposed integrated ring resonators in 1969 [48] and Weber and Ulrich first demonstrated guided optical ring resonator in 1971 [49]. The early works on ring resonators were performed using glass fiber resulting in a very large radius in the order of several mm, even cm, due to very small index difference. In the early 1990s, several groups demonstrated ring resonators in III-V semiconductors [50, 51]. As mentioned previously, the high index contrast between Si and SiO_2 results in tight confinement of light inside the waveguide/resonator and it results into much smaller bending radius. Consequently, Si-SiO_2 became the platform of choice for single-mode microring resonators [46].

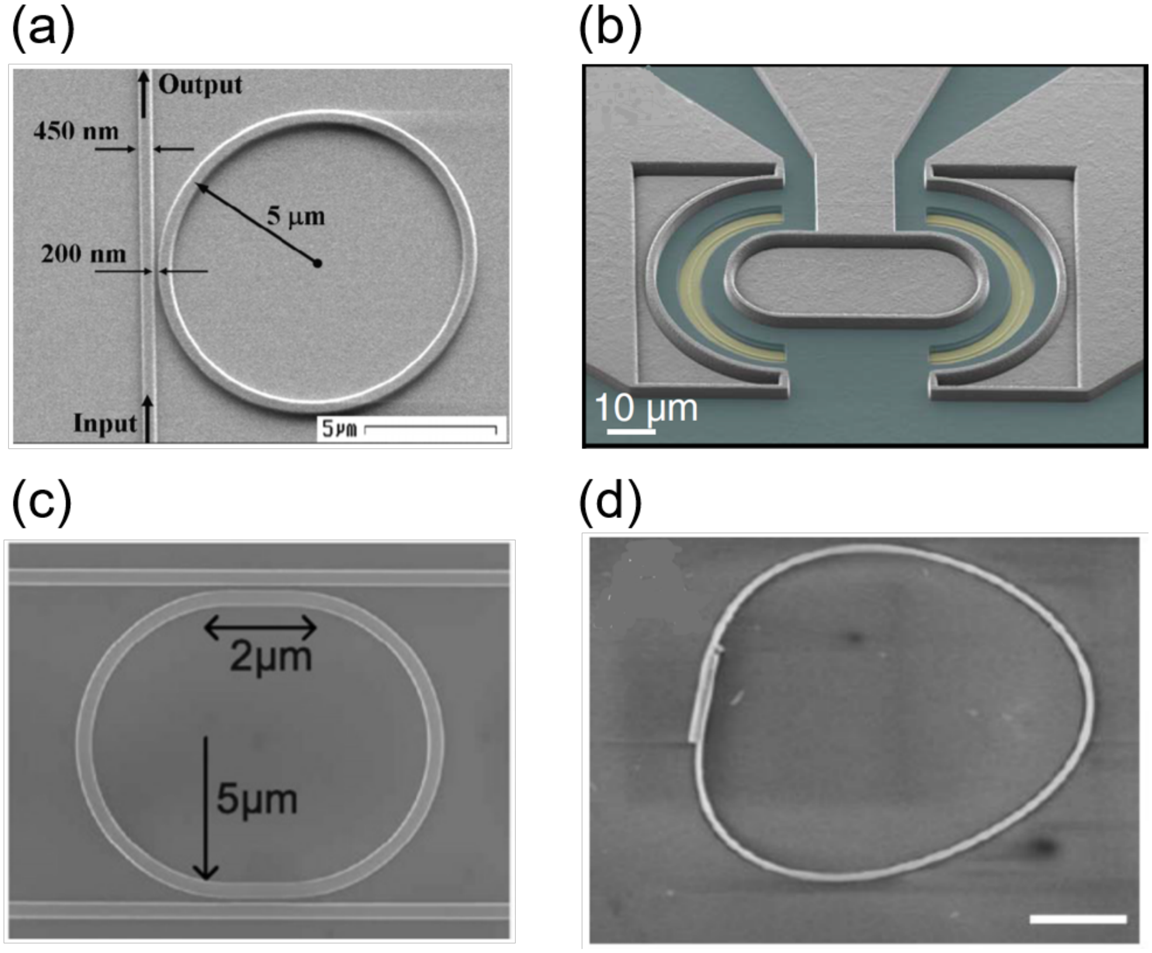

Figure 1.5: Scanning Electron Microscope images of ring resonators being used as a part of a (a) logic gate [52], (b) modulator [53], (c) sensor [54], (d) laser [55].

Today ring resonators have found applications in diverse devices such as lasers [50], amplifiers [56], sensors [54], optical channel dropping filters [57], optical add/drop (de)multiplexers [58], modulators [53], switches [59], routers [60], and logic gates [52]. Some of the ring resonators used in such applications are shown in Fig. 1.5.

1.2.3 Directional Couplers

Directional couplers are passive devices that were used mostly in the field of radio technology before the advent of micro-electronic and photonic circuits. In a directional coupler or coupled waveguides setting, two waveguides are brought into close proximity to each other with a gap in between them. The evanescent field of one guide extends out and partially overlaps the adjacent guide so that energy can tunnel from one guide to the other through the interaction of the evanescent tail. Being symmetric, energy can flow either way in this structure. Structures of this type serve as mode combiners for heterodyne receivers, and optical taps [61].

The first proposal of a guide, suitable for integrated optical circuitry and consisting of a dielectric rod with rectangular cross section surrounded by several dielectrics of smaller refractive indices was introduced in 1969 [62]. It showed promise due to its size, single-mode operation, mechanical stability, simplicity, and precise construction. Later, in 1976, Kogelnik put forward theoretical details of a coupled waveguide structure in which complete conversion of light from one guide to the other can be achieved by an electrical adjustment [63]. These structures had potential to be used to make photonic switches, modulators, splitters, and combiners. After the realization of the potential of SOI platform for integrated photonic devices, directional couplers fabricated using silicon have been widely used as power couplers due to their simple configurations [64].

1.3 Roadmap for Silicon Photonics

It is clear that silicon photonics has a bright future. Based on the expectation that silicon photonic interconnects will out perform electrical and multi-mode-fiber interconnects due to their reduced cost of $1/Gbps, the mega-datacenter and high-performance computing companies are launching a large-scale deployment of silicon-photonics based interconnects starting in 2018 [65]. It is anticipated that the total revenue of silicon photonics will reach several hundreds of millions of US dollars (Fig. 1.6).

During the early decades, the first stage of silicon photonics research was mainly focused on preliminary devices and building-block circuits. Researchers investigated several funda-

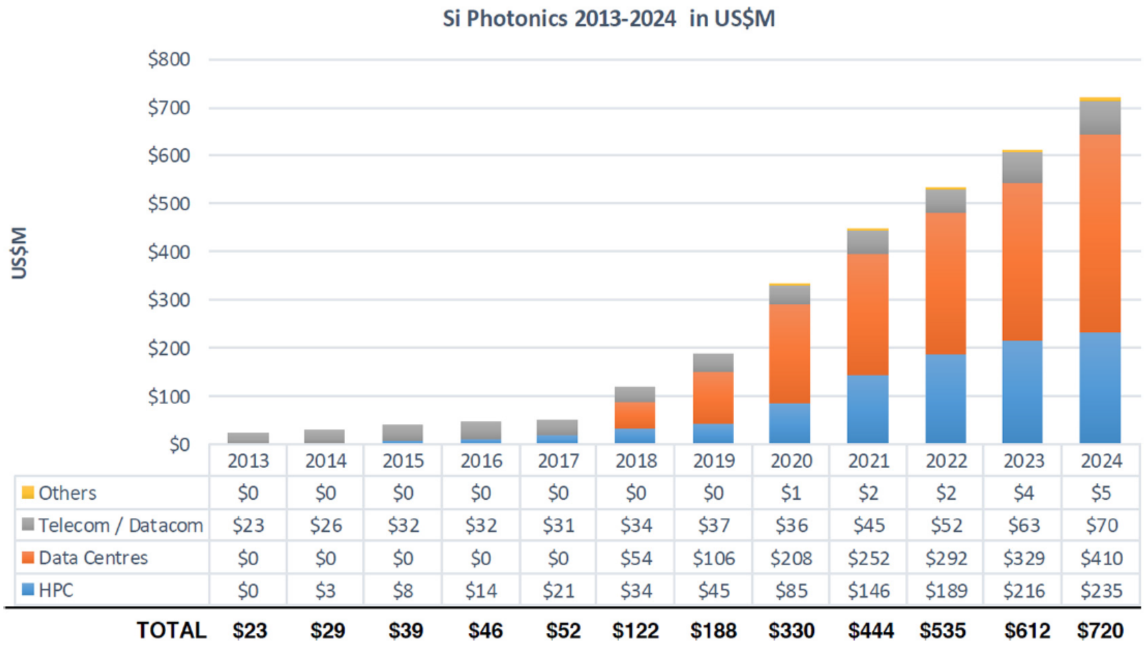

	2013	2014	2015	2016	2017	2018	2019	2020	2021	2022	2023	2024
🟨 Others	$0	$0	$0	$0	$0	$0	$0	$1	$2	$2	$4	$5
◼ Telecom / Datacom	$23	$26	$32	$32	$31	$34	$37	$36	$45	$52	$63	$70
🟧 Data Centres	$0	$0	$0	$0	$0	$54	$106	$208	$252	$292	$329	$410
🟦 HPC	$0	$3	$8	$14	$21	$34	$45	$85	$146	$189	$216	$235
TOTAL	**$23**	**$29**	**$39**	**$46**	**$52**	**$122**	**$188**	**$330**	**$444**	**$535**	**$612**	**$720**

Figure 1.6: Silicon photonics 2013-2024 market forecast [65].

mental problems such as fiber-to-waveguide coupling and duplicating photonic components developed on other material platforms [18]. While many practical devices have now been perfected and fully commercialized, there are still shortcomings of silicon as a photonic material, such as, its inefficiency to produce light sources. Nowadays, researchers from both academia and industry are shifting their efforts towards the optimization of the existing components and expansion of applications. In the following subsections a brief overview of the future challenges to be solved in the silicon photonic platform is presented.

1.3.1 Data Communications

The motivations to adopt silicon photonics into datacenters and other data-communications markets are low cost per data lane (~$1/Gbps), low power consumption per data line (few pJ/bit), and good manufacturability and reliability [65]. Some of the major silicon photonic technologies involved and challenges to meet the future data communications and datacenter requirements are modulators and detectors, on-chip power efficient lasers, CMOS integration, fiber attach and (de)multiplexers [65]. Modulators need to be high-speed, CMOS drivable, and remain manufacturable with high throughputs when integrated. Grating couplers and edge couplers need to have less insertion loss and larger optical bandwidth. Multiplexers need to be low-loss and polarization insensitive.

1.3.2 Light Sources

As mentioned previously, electrically pumped efficient sources on silicon are a challenge due to the indirect bandgap of silicon. To circumvent this problem, currently, the majority of light sources in silicon photonics use III-V gain regions directly onto silicon wafers (Fig. 1.7). While the silicon platform offers low propagation loss, low bending radius and high integration densities, III-V materials offer advantages of direct bandgap, high gain values and bandgap tuning [65].

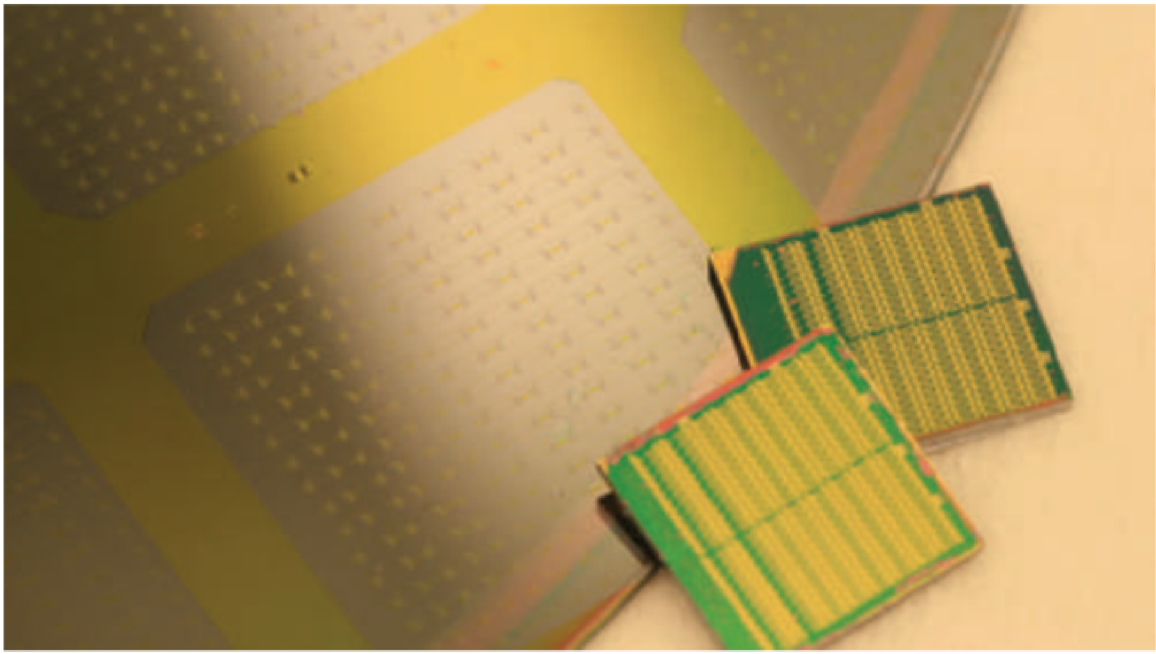

Figure 1.7: A portion of a 150 mm-diameter IIIV-on-SOI wafer containing ring cavity lasers (left) and 1 cm^2 chips containing 400 micro-ring lasers (right) [66].

The three major improvements required for future light sources for interconnects are bandwidth density, energy efficiency and latency. In addition, power efficiency and high-temperature operation are extremely important in future integration efforts.

1.3.3 Optical Modulators

The optical modulator is an essential element in most silicon photonic circuits. While impressive performances have been demonstrated in various material platforms like graphene [67], organics [68] and III-V compounds [69], these platforms lack easy CMOS compatibility like silicon.

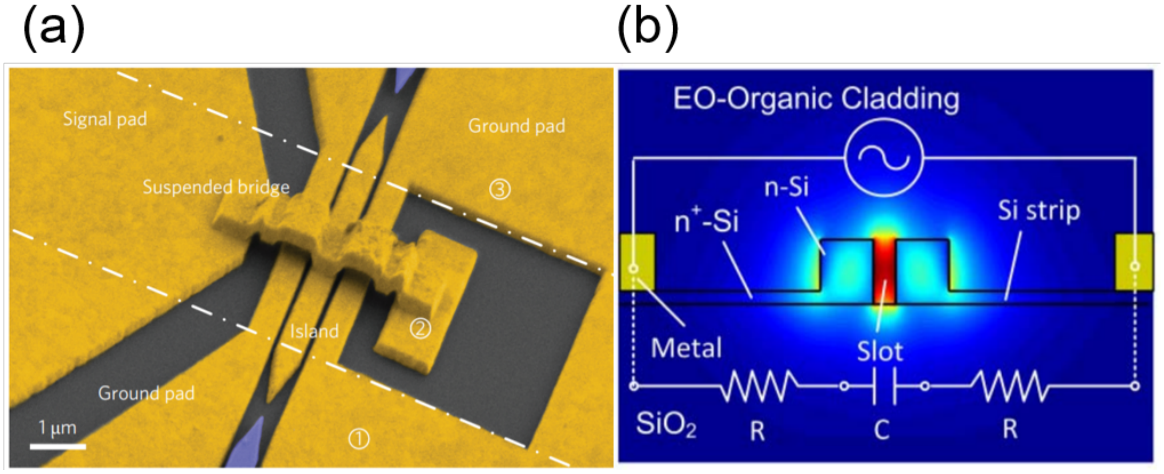

Figure 1.8: (a)Microscope image of a plasmonic modulator [70] and (b) diagram of a silicon-organic modulator cross section [68].

The most common modulator in silicon photonics is the Mach-Zehnder interferometer (MZI) based modulator [71]. As applications for silicon photonics become more complex in terms of the amount of channels involved, low power consumption and temperature sensitivity are becoming increasingly the major factors. In this regard, new materials, if efficiently integrated with the silicon waveguide can yield significant advancements in performance. Examples include plasmonic modulator [70] and silicon-organic modulator [68], as shown in Figs. 1.8(a) and (b), respectively.

1.3.4 Photodetectors

The main requirement for active devices of photodetectors for silicon photonics is to be compatible with silicon technology and to maintain high bandwidth, efficiency and low loss while consuming low power. Since silicon is transparent for wavelengths larger than 1100 nm, several novel techniques have been employed to offer detection of light in the communication band of wavelengths ranging from 1300 to 1550 nm. These include Ge-on-Si [72] and Si$^+$-implantation [73].

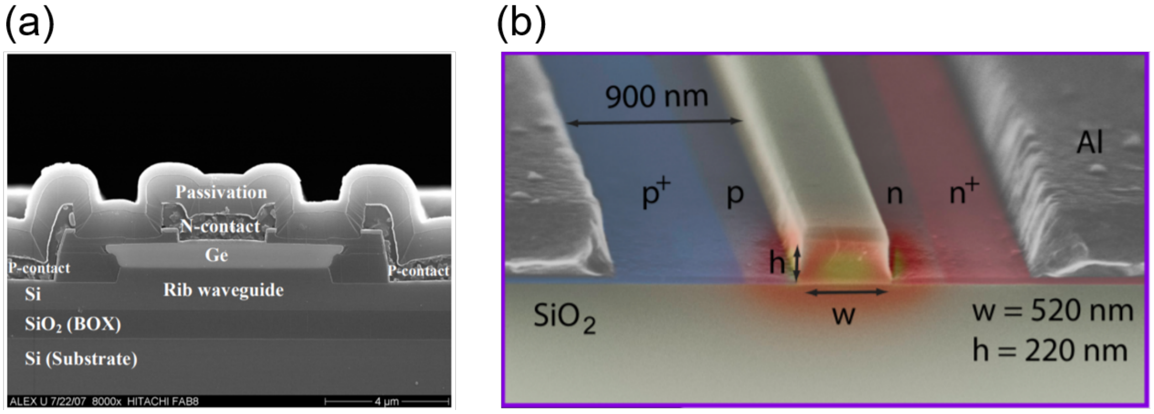

Figure 1.9: (a) Cross-section SEM image of a Ge waveguide photodetector [72], (b) False color SEM crosssection of a p-i-n device [73].

The Ge waveguide photodetectors currently have satisfactory performance to address numerous applications including optical communications [65]. One major advantage of Ge is that it is a silicon-foundry-compatible element. However, several challenges are still to be solved that include further reduction of detector noise, increase of detector sensitivity and data rate, and extension to mid-infrared range.

1.4 Advancements in Fabrication Technology

Advances in the development of CMOS-based photonic systems in recent years have promised commercial development of such systems on a large scale. This has become possible due to different modifications of silicon-based materials including silicon-on-insulator, SiGe alloys, and strained Si. The most vital reasoning to utilize microelectronics silicon foundries for photonics is that silicon foundry offers the lowest processing cost (per unit area) and the highest quality of silicon wafers compared to any other semiconductor materials [74]. And history has showed that if it is possible to realize one's objective through silicon, it becomes difficult for other technologies to compete [3].

Considerable research work is going on currently that addresses the need for integrating a plethora of components on a common waveguide platform (e.g., SOI) with high yield. There exist silicon foundries that produce highly controlled wafers (Fig. 1.10) for photonic circuits. Several silicon photonics foundries that offering multi-project wafers are IMEC, LETI and A*Star/IME. In these foundries SOI substrates with a silicon device layer thickness of 220 nm have become the standard waveguide height [75]. However, this height can be changed locally by etching or overlayer deposition. Although the platform with 300 nm silicon thickness appears to be somewhat superior to that with 220 nm silicon, further improvement is needed in terms of phase accuracy and bend radii [65].

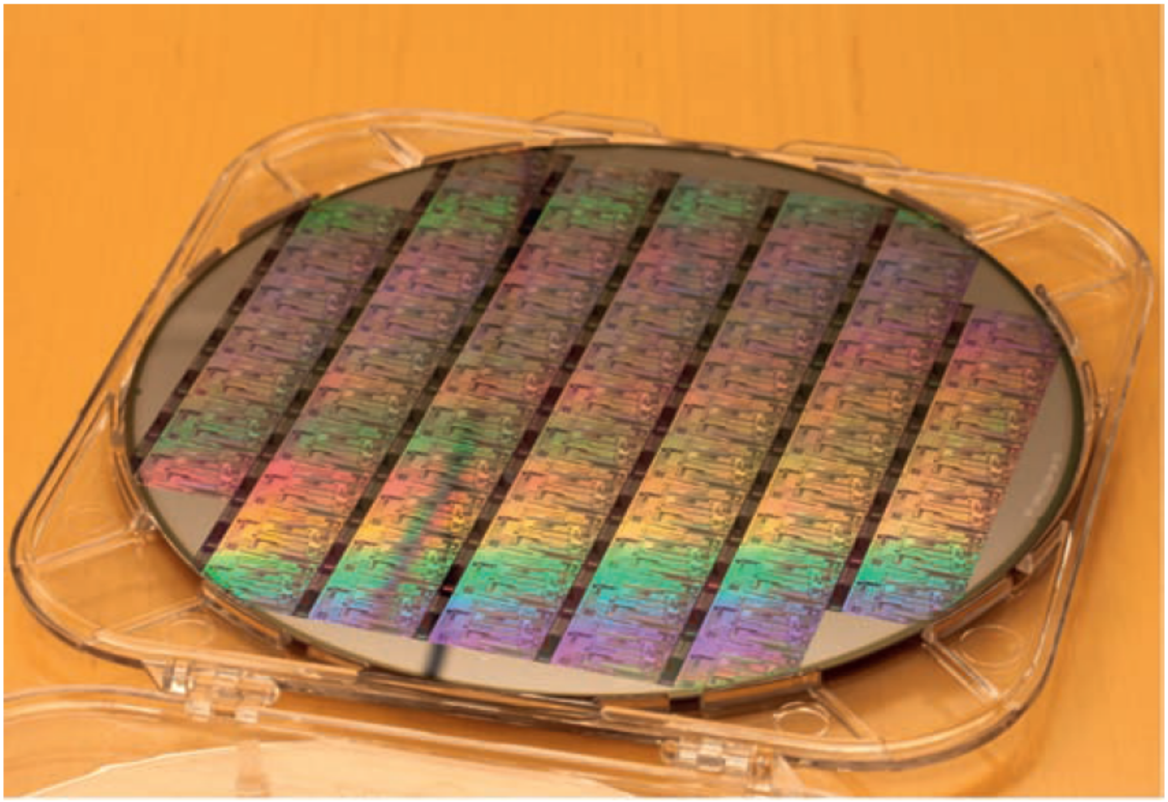

Figure 1.10: Photograph of 8” SOI wafer with various photonic components and circuits [76].

Concurrently, link price, performance and power consumption need to be improved in order to decrease the technology cost ($) and the energy cost (pJ/bit) of data transmission. Increasing the integration density of the photonic components is the main way to achieve this goal. This requires the implementation of several new process steps (Fig. 1.11) that include multiple SOI patterning, allowing the integration of strip-and rib-waveguides with varying SOI and slab thicknesses, integrating new material layers.

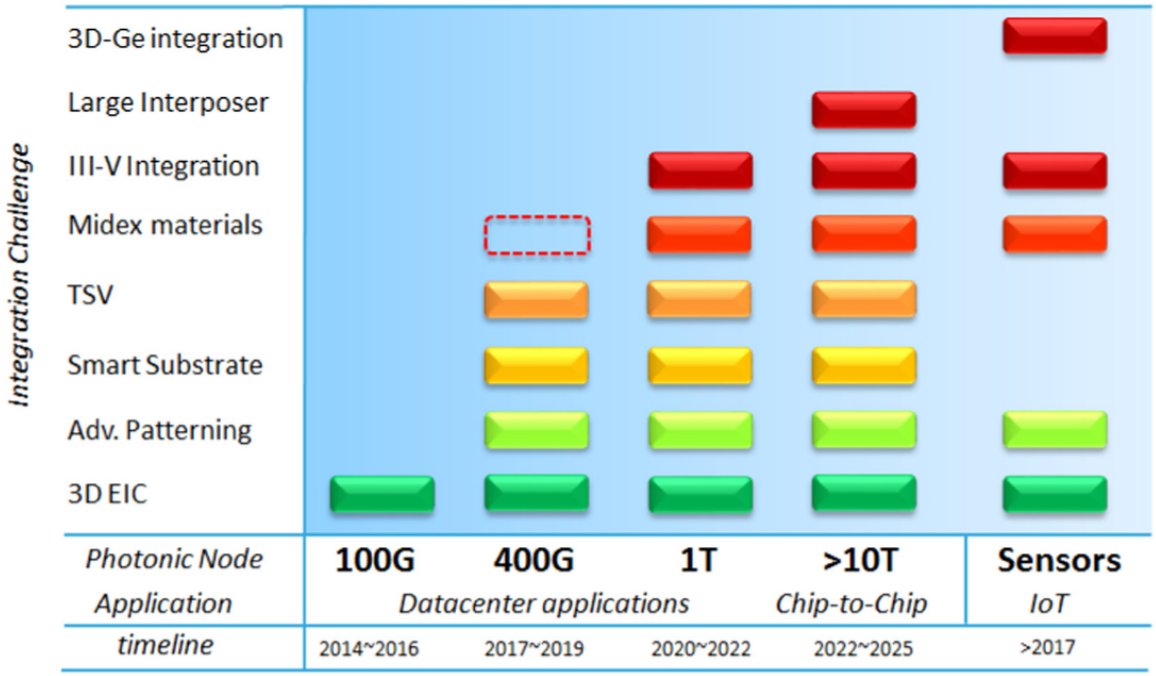

Figure 1.11: Process integration roadmap versus photonic node [65].

Another major point for silicon photonics from fabrication point of view is packaging that can significantly affect the performance and cost of the overall photonic module. The main challenges associated with packaging include packaging of single mode fibers, integration of sources and control electronics, management of thermal effects and development of fast, automated and high-volume packaging equipment. After these challenges are met, the associated design rules are implemented within software tools such as Mentor Graphics and Phoenix Software [77]. The main purpose of these efforts is to ensure that packaging is not the weak link in the supply chain.

1.5 Scope of Dissertation

The application field of silicon photonics is vast and continually expansive; few of which have been mentioned above. In terms of communication applications, silicon photonic circuits have the potential to be used as (de)modulators, amplifiers and dispersion controlling element in interconnects. In this dissertation these three aspects of silicon photonics for optical communication are analyzed.

Chapter 2 discusses a theoretical overview as well as computational and experimental framework for designing silicon-based nanophotonic devices. **Chapter 3** examines is coherent-perfect-absorption based differential phase shift keying (DPSK) demodulator circuit utilizing a ring resonator. By controlling the absorption in the ring and matching it with the coupling coefficient of the two bus waveguides, the phase response of the device is controlled. In addition, a delay line is used as required for a typical DPSK demodulator circuit. The result is a compact, CMOS-compatible on-chip circuit to decode DPSK encoded signal. **Chapter 4** presents non-Hermitian parametric amplification via four wave mixing (FWM). For FWM process to occur efficiently, a phase matching condition between the real propagation constants of the pump, signal, and idler beams must be satisfied. However, if some extra dissipation to the idler component can be added then the phase matching requirement can be relaxed. In simple terms, it means we are adding loss for the idler in order to achieve gain for the signal; irrespective of their wavelengths and waveguide geometry. **Chapter 5** centers onto the dispersion engineering of Si/plasmonics hybrid optical interconnections. Basically, here we investigate the dispersion properties of such device and see how the waveguide geometry can effectively change the dispersion properties of the hybrid mode. This method can potentially be used to tune the wavelength for zero group velocity dispersion in the communication C-band.

Chapter 2

Theory and Methodology

2.1 Theoretical Overview

In this section several theoretical concepts are briefly reviewed that are essential to this thesis. They are differential phase shift keying, coherent perfect absorption, four wave mixing, and dispersion.

2.1.1 Differential Phase Shift Keying

During most of the last century majority of the communication systems was in the analog form. However, the digital format gained popularity in the 1990s. In transmitting and receiving digital carrier signals, there are three basic forms of modulation [78]: amplitude shift keying (ASK), frequency shift keying (FSK), phase shift keying (PSK), as shown in Fig. 2.1. In ASK, the amplitude of the carrier is varied in proportion to the input data signal. When the bit is **0**, the carrier is off and when the bit is **1**, the carrier is on. In FSK, the frequency of the carrier is varied in proportion to the input data signal. A **0** is transmitted by a pulse of frequency ω_1, and **1** is transmitted by a frequency of ω_2. In PSK, we add a phase difference to the carrier frequency for **1** bit with respect to that of the **0** bit, or vice versa. Compared to ASK and FSK schemes, PSK is more power efficient and also less susceptible to errors.

Also, a higher data rate of transmission can be achieved using a high level of PSK modulations such as Quadrature PSK (represents 2 bits per constellation), 16-Quadrature Amplitude Modulation (represents 4 bits per constellation) etc.

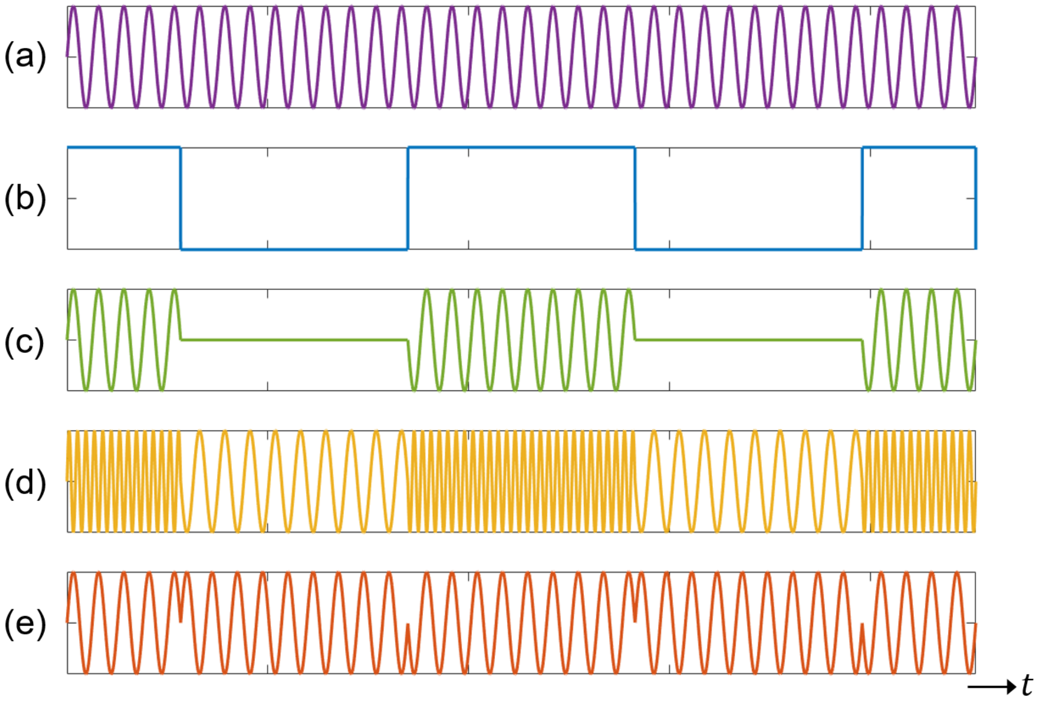

Figure 2.1: Digital modulation schemes where a (a) carrier frequency is being modulated by the (b) data bit stream and results into (c) amplitude shift keying, (d) frequency shift keying, and (e) phase shift keying.

The straight-forward demodulation scheme for ASK signals is envelope detection. FSK signals can also be decoded in this way after converting to ASK through bandpass filters. Although envelope detection cannot be used for PSK encoded signal, it is still possible to demodulate PSK signals noncoherently by means of a clever method known as differential PSK (DPSK). The main advantage of DPSK modulation scheme is that it facilitates noncoherent demodulation. Regular PSK typically does not support this, and therefore requires coherent demodulation only. Coherent demodulation means that the carrier sinusoid which is modulated by the message signal to get the passband signal has to somehow be reproduced at the receiver end and thereby used for demodulation of the passband signal to obtain the message. This can become tricky because more often than not, the received signal's carrier frequency has deviated from the original because of Doppler and other effects. Thus using the same carrier frequency as the transmitted signal will give a noisy demodulated message signal. But since the receiver has no knowledge of what transpired during transmission, generating the received carrier is not easy.

DPSK modulation offers a way out by encoding the information data into the phase difference for two successive bits, $k-1$ and k. Since the phase value in PSK is finite (equaling to 0 and π in binary PSK), the information data can be encoded into the phase difference ($\Delta\phi = \phi_k - \phi_{k-1}$) by the transmitter. This technique is known as differential encoding (Fig. 2.2(a)), where the input data (I_k) is added with its one bit delayed version to get the modulated data (q_k). For example, a phase difference of zero represents **0** bit whereas a phase difference of π means **1** bit. The polar line code in Fig. 2.2(a) simply outputs the differentially encoded bit pattern (a_k) as $+1$ and -1. It is then input into a regular PSK modulator and we get $\pm\cos\omega_c t$ as the differentially encoded signal.

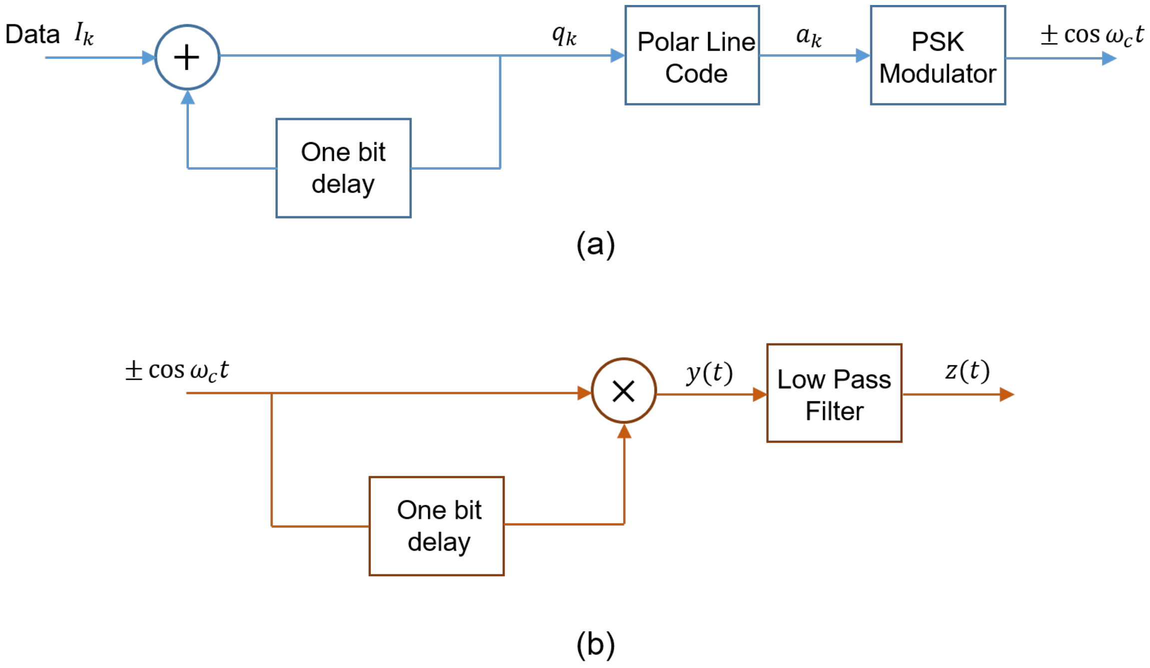

(a)

(b)

Figure 2.2: Differential Phase Shift Keying (a) Modulator and (b) Demodulator.

If the data bit is **0**, both the present and previous pulses have the same phase (both pulses being either $\cos\omega_c t$ or $-\cos\omega_c t$). If the data bit is **1**, the present and previous pulses are of opposite polarities (one being $\cos\omega_c t$, while the other being $-\cos\omega_c t$).

Table 2.1: Differential encoding and decoding of DPSK signals

Time k	0	1	2	3	4	5	6	7	8	9	10
I_k		1	0	1	0	0	1	1	1	0	0
q_k	0	1	1	0	0	0	1	0	1	1	1
a_k	-1	1	1	-1	-1	-1	1	-1	1	1	1
ϕ_k	π	0	0	π	π	π	0	π	0	0	0
$\phi_k - \phi_{k-1}$		π	0	π	0	0	π	π	π	0	0
Detected bits		1	0	1	0	0	1	1	1	0	0

In demodulating DPSK encoded signal (Fig. 2.2(b)), a local carrier is not required to be generated since the received modulated signal itself is a carrier ($\pm\cos\omega_c t$). So, at first, the received signal is delayed by one bit interval. If the received pulse is identical to the previous pulse, the product $y(t) = \cos^2\omega_c t = (1/2)(1+\cos 2\omega_c t)$, and the low pass filter output $z(t) = 1/2$. And the present bit is detected as **0**. If the received and previous pulses are of opposite polarity, then $y(t) = -\cos^2\omega_c t$ and $z(t) = -1/2$. And the present bit is detected as **1**. Table 2.1 and Figure 2.3 illustrate examples of the encoding and decoding.

By using such noncoherent detection scheme, DPSK modulation format has recently become of interest for on-chip optical communication systems. This interest is due to its 3-dB improvement in receiver sensitivity in comparison to an intensity modulated direct detection (IMDD) systems, thus enabling increased system margin and reduced input power to the fiber spans and an increasing length of the fiber link [79]. In addition, DPSK scheme is more tolerant to fiber nonlinearities [80].

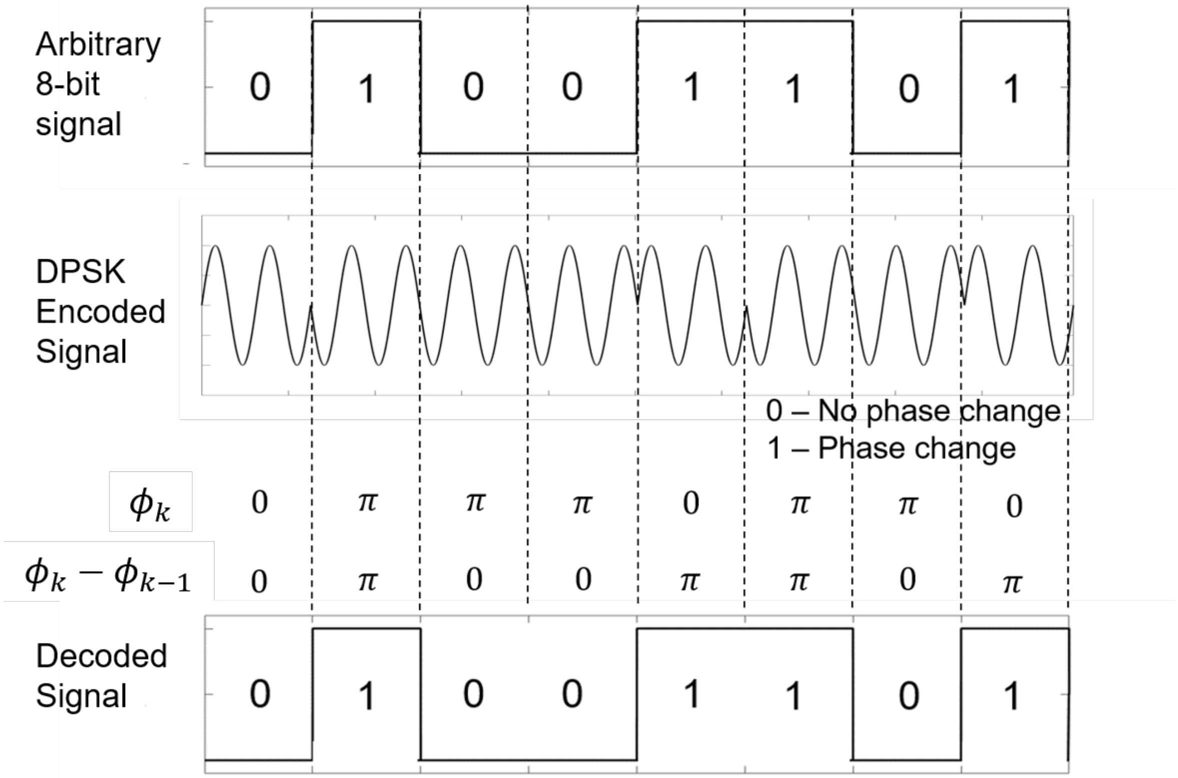

Figure 2.3: The process of differential phase shift keying modulation and demodulation. DPSK encodes an arbitrary bit pattern into a carrier sinusoid in such a way that it changes its phase by 180° only for bit **1**. For demodulation of the signal, the relative phase of the two successive bits are measured and the phase pattern for this differential signal correctly corresponds to the main bit pattern.

2.1.2 Coherent Perfect Absorption

The concept of coherent perfect absorption was first introduced by a group from Yale University [81]. It is nothing but a time-reversed counterpart of laser emission. In the lasing process, a cavity with gain produces outgoing optical fields with a definite frequency and phase relationship, without being illuminated by coherent incoming fields at that frequency. The laser is coupled to an energy source (the pump) that inverts the electron population of the gain medium, causing the onset of coherent radiation at a threshold value of the pump. Because of the property of time reversal, it follows that the same cavity, with the gain medium replaced by an equivalent absorbing medium, will perfectly absorb the same frequency of light, if it is illuminated with incoming waves with the same field pattern. This phenomenon is known as coherent perfect absorption (CPA).

The concept of CPA has been utilized in our group previously to propose an integrated optical modulator using a ring resonator (RR) based device [82]. The schematic of the device is shown in Fig. 2.4(a). In particular, the input to the ring resonator is evenly split into two signals, with a phase shift ($\Delta\phi$) introduced into one of them. The two signals are then coupled to the ring through the two bus waveguides. The ring has an internal loss rate, γ_i, which represents round-trip losses within the resonator, such as absorption, scattering, and bending loss. The steady-state power to the ring resonator from the two bus waveguides has a coupling coefficient of γ_c. To achieve efficient power transfer between the ring and the waveguide, the device must operate such that $2\gamma_c = \gamma_i$, which is a condition known as critical coupling [83, 84]. Under this condition, the transmitted signal ideally drops to zero.

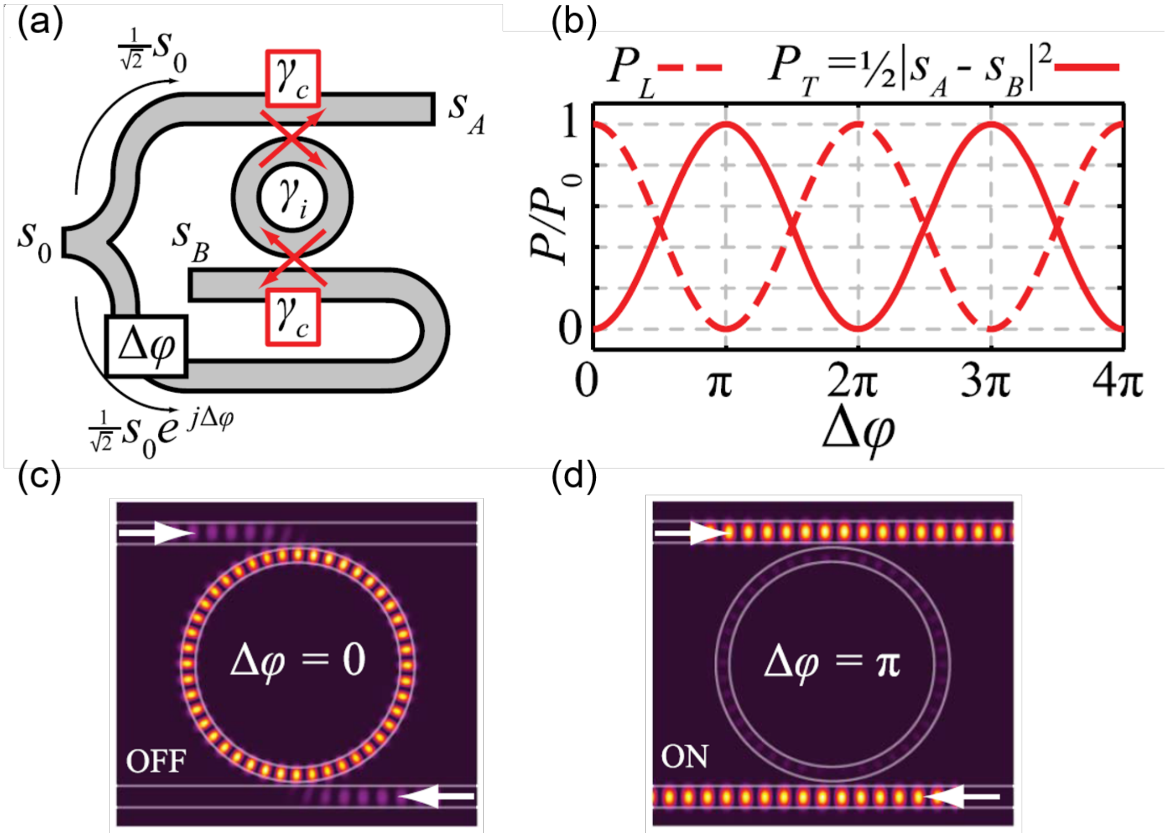

Figure 2.4: (a) Schematic of a RR-CPA modulator, (b) Power loss and transmission from the CPA modulator as a function of phase shift, (c) ON and (d) OFF states field profiles of the modulator [82].

Using temporal coupled mode theory [83], the time-dependent-coupling equation for the positive frequency component of the complex mode amplitude, a, of the resonator can be written as [82]

$$\frac{da(t)}{dt} = j\omega_0 a - \frac{1}{2}\gamma_{\text{tot}} a + \sqrt{\frac{\gamma_c}{2}}\left(1 + e^{j\Delta\phi}\right) s_0 \tag{2.1}$$

where ω_0 is the resonant frequency, $\gamma_{\text{tot}} = 2\gamma_c + \gamma_i$ is the total loss rate, $s_0 = \sqrt{P_0}$, and P_0 is the input optical power. The steady-state frequency response of the resonator is derived from Eq. 2.1 as

$$a(\omega) = \frac{\sqrt{\frac{\gamma_c}{2}}\left(1 + e^{j\Delta\phi}\right) s_0}{\frac{1}{2}\gamma_{\text{tot}} + j(\omega - \omega_0)}. \tag{2.2}$$

Using conservation of energy, the complex power amplitude escaping from ports A and B can be expressed as

$$s_A = \frac{1}{\sqrt{2}} s_0 - \sqrt{\gamma_c} a \tag{2.3}$$

$$s_B = \frac{1}{\sqrt{2}} s_0 e^{j\Delta\phi} - \sqrt{\gamma_c} a. \tag{2.4}$$

When the device is critically coupled then power through any of the bus waveguides at resonant frequency ($\omega = \omega_0$) is defined as

$$P_T = \frac{|s_A - s_B|^2}{2} = P_0 \sin^2\left(\frac{\Delta\phi}{2}\right). \tag{2.5}$$

Similarly, the steady-state power loss inside the ring is found from Eq. 2.2,

$$P_L = \gamma_i |a|^2 = P_0 \cos^2\left(\frac{\Delta\phi}{2}\right). \tag{2.6}$$

Equations 2.5 and 2.6 are plotted as a function of phase shift ($\Delta\phi$) in Fig. 2.4(b). Therefore, the power escaping from the resonator can be modulated to be between 0% and 100% of the input power by controlling the phase difference of two balanced input beams. The field profiles of the two extreme cases of the phase difference, namely 0 and π, are shown in

Figs. 2.4(c) and (d), respectively. When $\Delta\phi = 0$, the ring is in resonance and when $\Delta\phi = \pi$, the ring is out of resonance. To differentiate it with the typical ring resonance ($\Delta\omega = 0$) condition, we term this resonance condition as CPA resonance.

2.1.3 Four Wave Mixing

Four wave mixing (FWM) is a nonlinear optical phenomenon that occurs inside a third-order nonlinear medium. We consider three waves of angular frequencies ω_1, ω_2, and ω_3 and complex amplitudes A_1, A_2, and A_3 travelling inside such a third-order medium with a nonlinear coefficient of $\chi^{(3)}$. The combined electric field can be written as [85]

$$\mathcal{E}(t) = \sum_{q=1,2,3,4} \mathrm{Re}\left[A_q e^{j\omega_q t}\right]. \tag{2.7}$$

The dominant nonlinear polarization inside the medium is of third-order and can be expressed as

$$\mathcal{P}_{\mathrm{NL}} = 4\chi^{(3)}\mathcal{E}^3. \tag{2.8}$$

The corresponding source of radiation, $\mathcal{S} = -\mu_o \partial^2 \mathcal{P}_{\mathrm{NL}}/\partial t^2$, is therefore a sum of $8^3 = 512$ terms,

$$\mathcal{S} = \frac{1}{2}\mu_o \chi^{(3)} \sum_{q,p,r=\pm1,\pm2,\pm3,\pm4} \left(\omega_q + \omega_p + \omega_r\right)^2 A_q A_p A_r e^{\left[j\left(\omega_q+\omega_p+\omega_r\right)t\right]}. \tag{2.9}$$

Now, wave propagation in a nonlinear medium is governed by the basic wave equation [85],

$$\nabla^2\mathcal{E} - \frac{1}{c^2}\frac{\partial^2\mathcal{E}}{\partial t^2} = -\mathcal{S}, \tag{2.10}$$

where c is the speed of light inside the medium. Substituting Eq. 2.7 and 2.9 into the wave equation 2.10, we obtain four Helmholtz equations with associated sources [85],

$$\left(\nabla^2 + k_q^2\right) A_q = -S_q, \tag{2.11}$$

where S_q is the amplitide of the component of $\mathcal{S}$ at frequency ω_q. For the four waves to be coupled, their frequencies must satisfy conservation of energy,

$$\omega_1 + \omega_2 = \omega_3 + \omega_4. \tag{2.12}$$

In other words, if these frequencies are distinct, then three waves can combine and create a source at the fourth frequency. In the degenerate case for which two of the four waves have the same frequency $\omega_3 = \omega_4 \equiv \omega_p$, we have three waves with frequencies related by $\omega_s + \omega_i = 2\omega_p$, where we have replaced 1 and 2 with s and i, respectively to be consistent with the notations mentioned in chapter 4. For collinear waves travelling in the z direction, using slowly varying envelope approximation, we can find the following set of coupled equations [85],

$$\frac{dE_p}{dz} = i\kappa'_p[2E_sE_iE_p^*e^{-i\Delta kz} + E_p(|E_p|^2 + 2|E_s|^2 + 2|E_i|^2)], \tag{2.13}$$

$$\frac{dE_s}{dz} = i\kappa'_s[E_p^2E_i^*e^{i\Delta kz} + E_s(|E_s|^2 + 2|E_i|^2 + 2|E_p|^2)], \tag{2.14}$$

$$\frac{dE_i}{dz} = i\kappa'_i[E_p^2E_i^*e^{i\Delta kz} + E_i(|E_i|^2 + 2|E_s|^2 + 2|E_p|^2)] \tag{2.15}$$

where $E_{p,s,i}$ are the pump, signal, and idler waves, $\kappa'_{p,s,i} = 3\mu_0\omega_{p,s,i}^2\chi^{(3)}/2k_{p,s,i}$, $\Delta k = 2k_p - k_s - k_i$ is the phase-mismatch, and the asterisks denote complex conjugation. In order for this process to occur efficiently, the phase mismatch, Δk should be equal to zero. In this case, the signal and idler component will grow at the expense of the pump wave. Equations 2.13, 2.14, and 2.15 are the basis for non-Hermitian FWM process described in chapter 4.

2.1.4 Dispersion

The most prominent limitation on the fundamental bandwidth in optical waveguides is dispersion [61]. Dispersion essentially implies the broadening of an optical signal pulse in time. Figure 2.5 illustrates how dispersion can potentially limit the data rate of a communication channel. At the input, a pulse (representing a binary information) is launched onto an optical waveguide. Dispersion causes the pulse to spread in time. When it arrives atthe output, the pulse has broadened to the extent that it will seriously overlap adjacent pulses. This temporal broadening effectively establishes the maximum information capacity for a communication link.

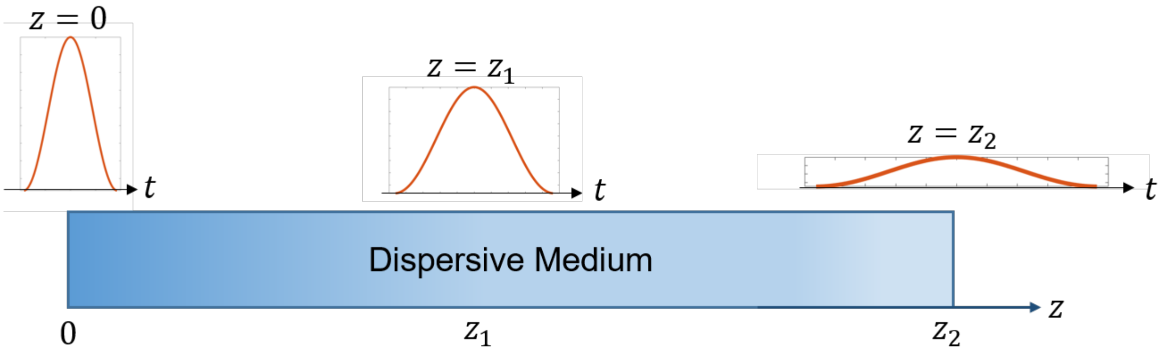

Figure 2.5: Broadening of an optical pulse traveling in a dispersive medium. Figure recreated following [85].

Optical waveguides display three types of dispersion [61]: material dispersion, modal dispersion and waveguide dispersion. In material dispersion, different wavelengths of light travel at different velocities within a given medium. So each wavelength component of a pulse that has a finite spectral bandwidth will travel at a different velocity. The pulse effectively will spreads out in time and space. Modal dispersion occurs in waveguides with more than one propagating mode. Each allowed mode in the waveguide will travel with a different group velocity. The modes arrive at the end of the waveguide slightly delayed relative to each other. This effectively spreads the temporal duration of the pulse. Waveguide dispersion, on the other hand, becomes significant in single mode systems operating near the zero material dispersion point.

The frequency-dependent propagation constant β is defined as $\beta = \omega n(\omega)/c$. Here, n refers to the effective index of the waveguide that is a function of the material of the waveguide and its geometry. For considering wavelengths that are spectrally far from each other, higher order dispersion terms become significant in the calculation of dispersion. These higher order terms as a function of wavelength λ are given by,

$$\beta_1 = \frac{d\beta}{d\omega} = \frac{1}{c}\left(n - \lambda\frac{dn}{d\lambda}\right) \tag{2.16}$$

$$\beta_2 = \frac{d^2\beta}{d\omega^2} = \frac{\lambda^3}{2\pi c^2}\frac{d^2n}{d\lambda^2} \tag{2.17}$$

$$\beta_3 = \frac{d^3\beta}{d\omega^3} = -\frac{\lambda^4}{4\pi^2c^3}\left[\lambda\frac{d^3n}{d\lambda^3} + 3\frac{d^2n}{d\lambda^2}\right] \tag{2.18}$$

Another important parameter for quantifying dispersion is group velocity dispersion (GVD), D, defined as $D = -2\pi c\beta_2/\lambda^2$. D is usually specified in units of ps/km-nm: the pulse broadening is measured in picoseconds, the length of the medium in kilometers, and the source spectral width in nanometers. It is a strong function of the waveguide geometry as plotted using finite element method in Fig. 2.6. The black curve in Fig. 2.6 refers to GVD of bulk silicon. As the waveguide cross-section is increased the mode is more confined inside the waveguide. This results into the GVD behavior approaching that of the bulk silicon, as indicated by the arrows in Fig. 2.6.

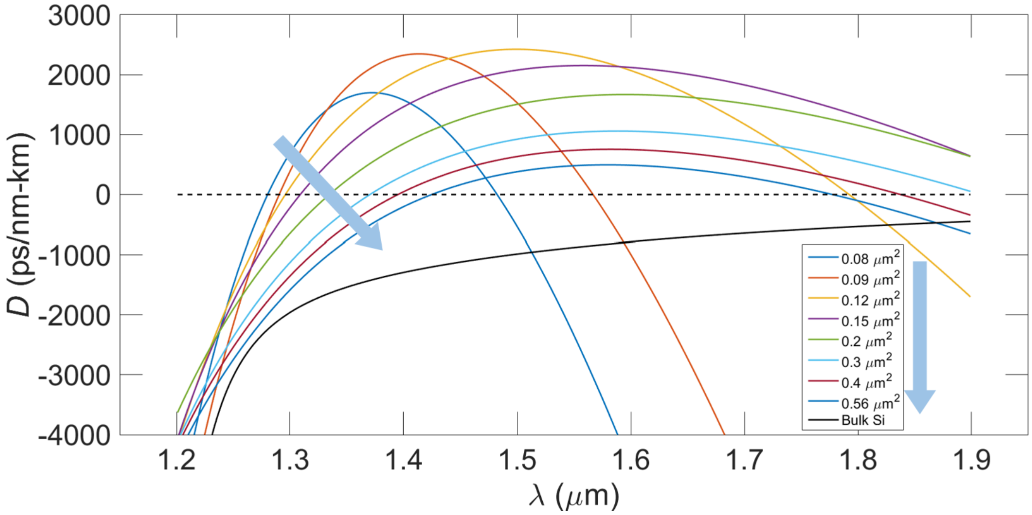

Figure 2.6: Group velocity dispersion as a function of wavelength for waveguides of various geometry in a silicon waveguide.

In a single-mode waveguide, modal dispersion is absent. Therefore, material and waveguide dispersions are the only dominating effects. Since most single-mode optical communication links operate near λ_0, obviously waveguide dispersion is an important parameter to consider while designing dispersion compensated optical devices.

2.2 Computational Methods

In this section we succinctly discuss several well-known numerical methods to study properties and propagation of electromagnetic waves in waveguide structures. These are finite element method, finite difference time domain, and effective index method. These computational methods work as a virtual replacement of the experimental method, where one is performing all the relevant 'experiments' on computer reducing development cost and quickening development of new products [86]. In designing and optimizing photonic devices, simulations indeed play a very important role. In fact, applications of computational electromagnetics goes well beyond photonics [87] in diversified applications including, but not limited to, biological and medical science, quantum information science, antenna analysis and design, microwave devices to name a few.

2.2.1 Finite Element Method

The finite element method (FEM) is generally advantageous in complex geometries and/or high index contrast materials. It is a full-vector implementation for both propagating and leaky waveguide modes, and cavity modes for 1D and 2D Cartesian cross-sections and 3D bodies of revolution in cylindrical coordinates. It may be used to find all the modes or a small group of modes about a given wavelength.

In this method, the entire continuous domain is divided into a finite number of subdomains and trial functions defined over each subdomain are used [88]. The unknown function is represented by simple interpolation functions with unknown coefficients. Therefore, the original boundary-value problem with an infinite number of degrees of freedom is con-

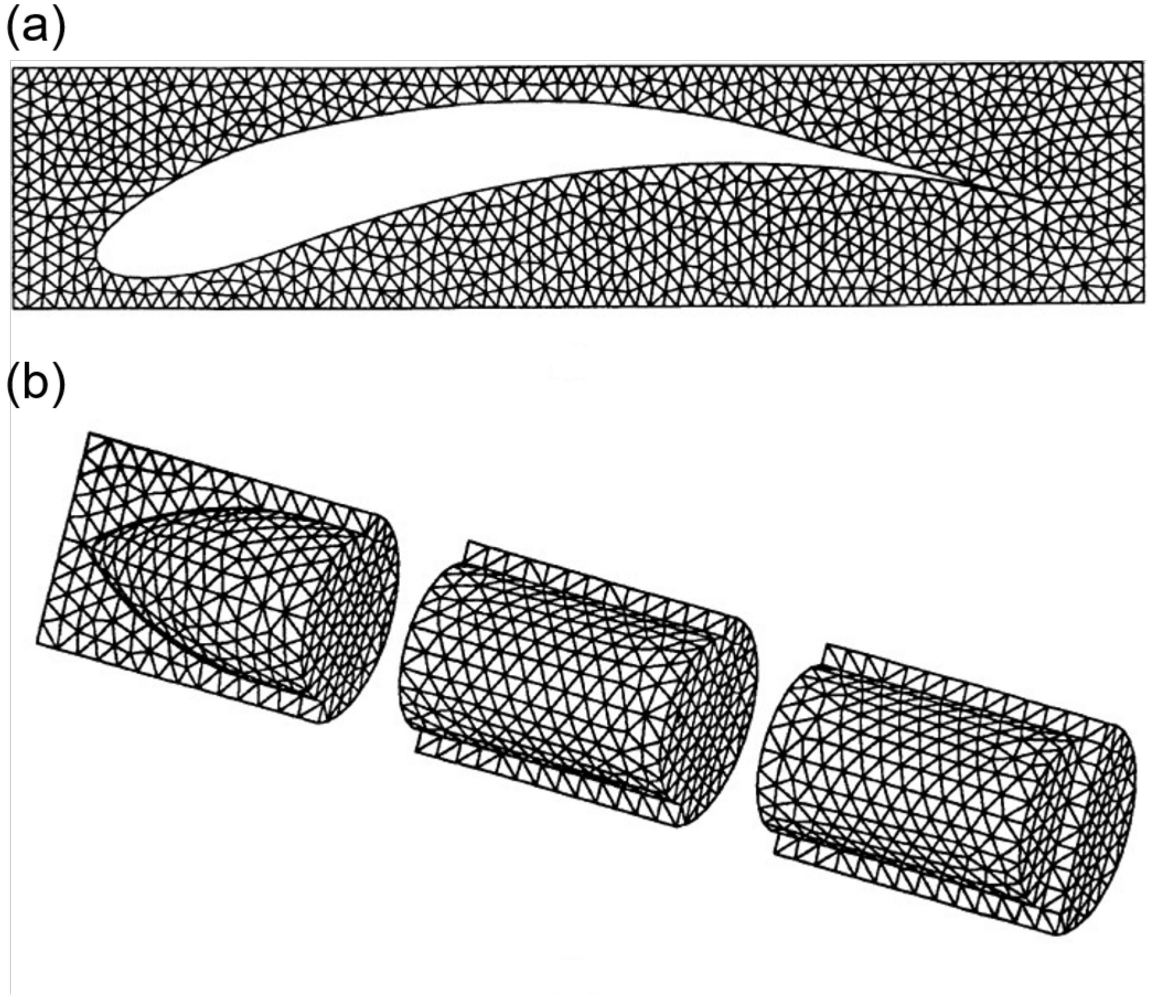

Figure 2.7: Examples of finite element discretization. (a) Two-dimensional with triangular elements. (b) Three-dimensional with tetrahedral elements. Figure from [88].

verted into a problem with a finite number of degrees of freedom, or in other words, the solution of the entire system is approximated by a finite number of unknown coefficients. Then a system of algebraic equations is obtained, and finally, a solution of the boundary-value problem is achieved by solving the system of equations.

Linear line segments, triangles, and tetrahedra are the basic one-, two-, and three-dimensional elements that model curved lines or surfaces by straight line segments or planar patches. Figure 2.7 gives two examples showing the finite element discretization of a two- and three-dimensional domain.

2.2.2 Finite Difference Time Domain

The finite-difference time-domain (FDTD) method is a very popular numerical scheme to rigorously solve Maxwell's equations without having any approximations or theoretical restrictions. This method is widely used as a propagation solution technique in integrated optics, especially in situations where solutions obtained via other methods such as the Beam Propagation Method (BPM) cannot cope with the structure geometry or are not adequate solutions. Since FDTD is a direct solution of Maxwell's curl equations, it therefore includes many more effects than other approximate methods.

2.2.2.1 General formulation

Assuming a nonmagnetic material ($\mu = \mu_0$) and source-free region ($J = 0$ and $\rho = 0$), Maxwell's curl equations are [85]

$$\nabla \times \mathbf{H} = \frac{\partial \mathbf{D}}{\partial t} \tag{2.19}$$

$$\nabla \times \mathbf{E} = -\mu_0 \frac{\partial \mathbf{H}}{\partial t} \tag{2.20}$$

where **E** and **H** are electric and magnetic fields, respectively and **D** is the electric displacement flux density. In simulating the various structures for this thesis, we have employed two-dimensional (2D) FDTD methods. In this case, the medium is considered to be infinite in the z-direction and no change is considered in z-direction, resulting in $\frac{\partial}{\partial z} = 0$. Therefore, Maxwell's equations 2.19 and 2.20 in terms of components become

$$\mathbf{a}_x \frac{\partial H_z}{\partial y} - \mathbf{a}_y \frac{\partial H_z}{\partial x} + \mathbf{a}_z \left(\frac{\partial H_y}{\partial x} - \frac{\partial H_x}{\partial y} \right) = \mathbf{a}_x \frac{\partial D_x}{\partial t} + \mathbf{a}_y \frac{\partial D_y}{\partial t} + \mathbf{a}_z \frac{\partial D_z}{\partial t} \tag{2.21}$$

$$\mathbf{a}_x \frac{\partial E_z}{\partial y} - \mathbf{a}_y \frac{\partial E_z}{\partial x} + \mathbf{a}_z \left(\frac{\partial E_y}{\partial x} - \frac{\partial E_x}{\partial y} \right) = -\mu_0 \left(\mathbf{a}_x \frac{\partial H_x}{\partial t} + \mathbf{a}_y \frac{\partial H_y}{\partial t} + \mathbf{a}_z \frac{\partial H_z}{\partial t} \right) \tag{2.22}$$

The above equations are then usually split into two groups [89],

Group 1:

$$\frac{\partial D_x}{\partial t} = \frac{\partial H_z}{\partial y} \tag{2.23}$$

$$\frac{\partial D_y}{\partial t} = -\frac{\partial H_z}{\partial x} \tag{2.24}$$

$$\frac{\partial H_z}{\partial t} = -\mu_0 \left(\frac{\partial E_y}{\partial x} - \frac{\partial E_x}{\partial y} \right) \tag{2.25}$$

Group 2:

$$\frac{\partial H_x}{\partial t} = -\frac{1}{\mu_0} \frac{\partial H_z}{\partial y} \tag{2.26}$$

$$\frac{\partial H_y}{\partial t} = \frac{1}{\mu_0} \frac{\partial E_z}{\partial x} \tag{2.27}$$

$$\frac{\partial D_z}{\partial t} = \left(\frac{\partial H_y}{\partial x} - \frac{\partial H_x}{\partial y} \right) \tag{2.28}$$

The first group is called TE to z polarization and the second group is called TM to z polarization [89].

2.2.2.2 Two-dimensional Yee implementation

The basic implementation of FDTD method was first proposed by Yee [90] and is known as the Yee algorithm. For 2D discretization using the TM mode (Group 2) in the previous section, we introduce the Yee mesh in Fig. 2.8. A Yee cell is formed around point (i, j). The electric field distribution within each cell is assumed to be constant and the z-component E_z of electric field is defined at the midpoint of each cell. The above Maxwell's equations are approximated as [86]

$$\begin{aligned} \frac{E_z^{n+1}(i,j) - E_z^{n}(i,j)}{\Delta t} \quad = \quad & \frac{1}{\varepsilon_0 \varepsilon_r(i,j)} \frac{H_y^{n+1/2}(i+1/2,j) - H_y^{n+1/2}(i-1/2,j)}{\Delta x} \\ & - \frac{1}{\varepsilon_0 \varepsilon_r(i,j)} \frac{H_x^{n+1/2}(i,j+1/2) - H_x^{n+1/2}(i,j-1/2)}{\Delta y} \end{aligned}$$

$$\frac{H_x^{n+1/2}(i,j+1/2)-H_x^{n-1/2}(i,j+1/2)}{\Delta t}=-\frac{1}{\mu_0}\frac{E_z^n(i,j+1)-E_z^n(i,j)}{\Delta y} \tag{2.29}$$

$$\frac{H_y^{n+1/2}(i+1/2,j)-H_y^{n-1/2}(i+1/2,j)}{\Delta t}=\frac{1}{\mu_0}\frac{E_z^n(i+1,j)-E_z^n(i,j)}{\Delta x}$$

From the above equations the time-stepping numerical algorithm for the interior region is

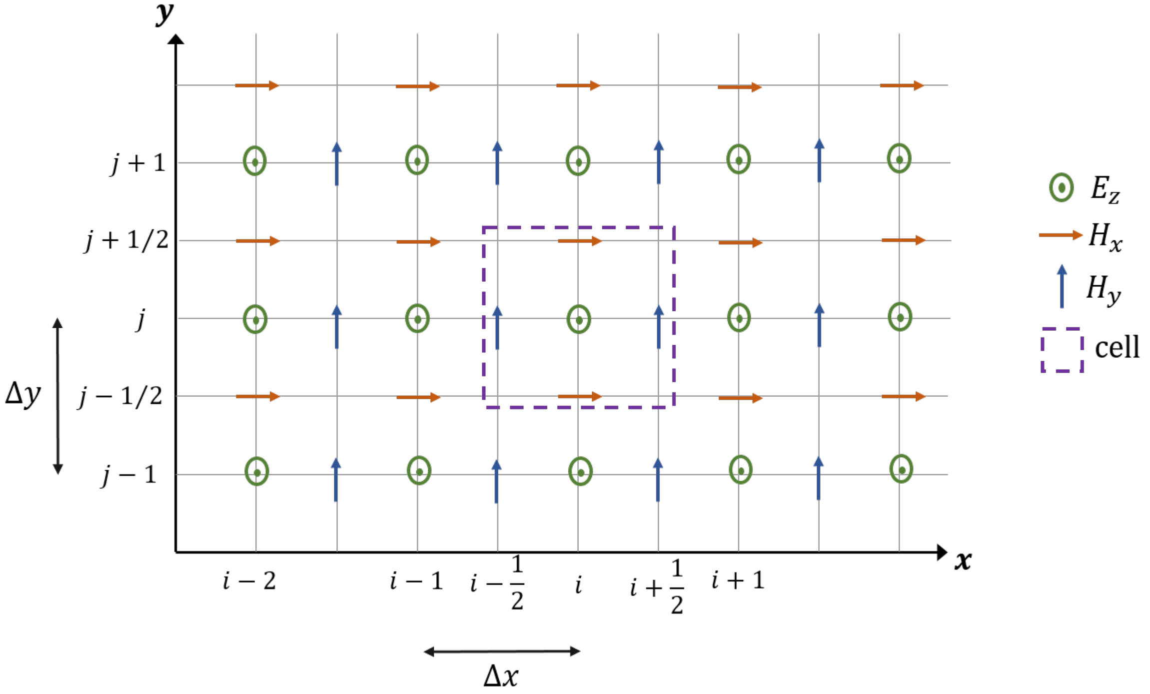

Figure 2.8: Yee mesh in 2D for the TM mode.

determined. Since the constants ε_0 and μ_0 appearing in these equations differ by several orders of magnitude, these equations are first scaled and then iteratively solved in a leapfrog manner, alternating between computing the **E** and **H** fields at subsequent intervals. In order to utilize the FDTD implementation we use Synopsys RSoft FullWAVE, where both physical and numerical parameters are required. The physical parameters include the relative permittivity and relative permeability as a function of space and/or frequency, and the electromagnetic field excitation. The numerical parameters include a finite computational domain, the boundary condition(s), and the spatial grid and temporal grid sizes. For our purpose, we assume a perfectly matched layer (PML) boundary condition, whereby electromagnetic fields incident on the simulation boundary are perfectly absorbed without any backward reflection that might cause disturbance to the forward travelling waves.

2.2.3 Effective Index Method

The complete, rigorous, and exact analysis of the mode structure of a dielectric waveguide can involve rather extensive and computationally expensive calculations. To circumvent this problem, a method known as the effective index method (EIM) has been developed [91]. It essentially converts a single three dimensional problem into two two-dimensional problems or a single two dimensional problem into two one-dimensional problems [61].

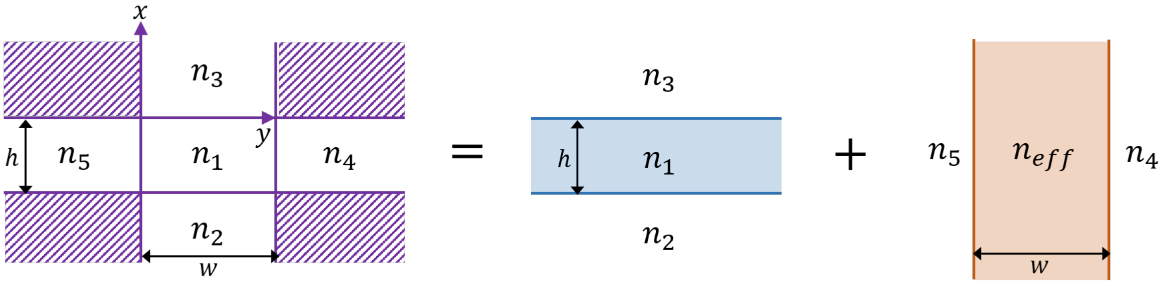

Figure 2.9: A buried dielectric waveguide can be decomposed into two spatially orthogonal waveguides: a horizontal and a vertical slab waveguide. The thin waveguide is analyzed in terms of the actual indices that form the structure. The thick waveguide is analyzed using the effective index found from the first waveguide analysis. Schematic diagram recreated from [61].

Let us consider the buried rectangular waveguide shown in Fig. 2.9. In order to use the effective index method, the first step is to elongate the waveguide out along its thin axis, in this case along the y-axis, forming a planar slab waveguide. The thin one-dimensional slab waveguide can be analyzed in terms of TE or TM modes to find the allowed value of the propagation constant, β, for the desired wavelength and mode of interest. Once β is found, the effective index of the slab is determined through the relation $n_{eff} = \beta/k_0$, where k_0 is the wavevector of the light being guided in vacuum. After this effective index is determined, we return to the original structure, and elongate it along the thick axis (in this case vertical), forming a slab waveguide in the x-direction. The modes for this waveguide can now be found, only instead of using the original value of the index for the guiding film, the effective index found in the first step must be used. The value of β found from this last step is the actual propagation constant value for the mode. However, it must be remembered that to be accurate, the aspect ratio of the width/height or vice versa of the waveguide must be equal to or exceed a factor of three to be accurate [61]. This is due to the fact that the electromagnetic mode is usually tightly confined within the core, and the amount of energy in the corner regions becomes negligible, so the wave equation can be solved using standard separation of variables as described here. However, if the core cross-section is much small, then the mode will have a significant amount of power in the corner. In this case, the x and y dependent solutions will be strongly coupled through the boundary conditions in the corner regions, making them mathematically inseparable.

The effective index method is perhaps the most popular and commonly employed technique for waveguide design. It is relatively straightforward to understand and apply, and its results are not too far from those generated from exact analysis using rigorous Maxwell's equations.

2.3 Fabrication Overview

In this section, we briefly describe the fabrication of some elementary silicon photonic components for testing that were performed at Brookhaven National Laboratories. We designed simple waveguides, ring resonators, Y-splitters, delay lines; fabricated them at BNL and characterized them in order to match with the design parameters. The purpose of this experimentation was to confirm that our proposed DPSK demodulator circuit (Chapter 3), that has all these discrete elements inside it, has well-characterized components. In addition, we can measure the effect of the variation of these components on the demodulator circuit. For example, the length of the delay line affects the bit rate and the circumference of the ring affects the critical coupling condition.

2.3.1 Base Wafer

The base wafer type that we worked on was that of Soitec SOI wafers [92]. It consisted of a 220 nm Si top layer followed by a 3 μm SiO_2 insulating layer and a 625 μm Si carrier wafer. The purpose of the 3 μm SiO_2 layer is to ensure that no coupling occurs to the substrate. The top layer of Si had a resistivity of 10-20 Ω-cm with a slight *p*-doping of $\sim 1 \times 10^{15}$ cm^{-3}. This base wafer was cut into several 1 cm × 1 cm pieces. Each piece then underwent the fabrication steps, summarized briefly in Fig. 2.10.

2.3.2 Wafer Preparation

As a first step, the silicon wafer pieces were subject to a cleaning process that consisted of three immersive baths for 5 minutes each. The initial bath was in acetone, followed by methanol, and then isopropanol alcohol. While they were immersed, they were sonicated to ensure that the surface was free of fine particulates which could distort and add roughness to the nano-scale components. Following the baths, compressed N_2 was used to dry the chips. They were then subjected to a baking process. The bake process was performed at 450 $\circ C$ for 30 minutes to ensure that any surface moisture was removed that could potentially prevent good adhesion of the resist. Next, the chips were subjected to an O_2 plasma cleaning at 100 W for 2 minutes. A hexamethyldisilizane (HMDS) monolayer was then applied on top of the wafer chips utilizing a Yield Engineering Systems HMDS oven [93]. HMDS was needed to promote the chemical adhesion of an organic compound (photoresist) to a non-organic substrate (wafer). It acts as a sort of a transition layer, with favorable bonding properties to both the photoresist and wafer surface.

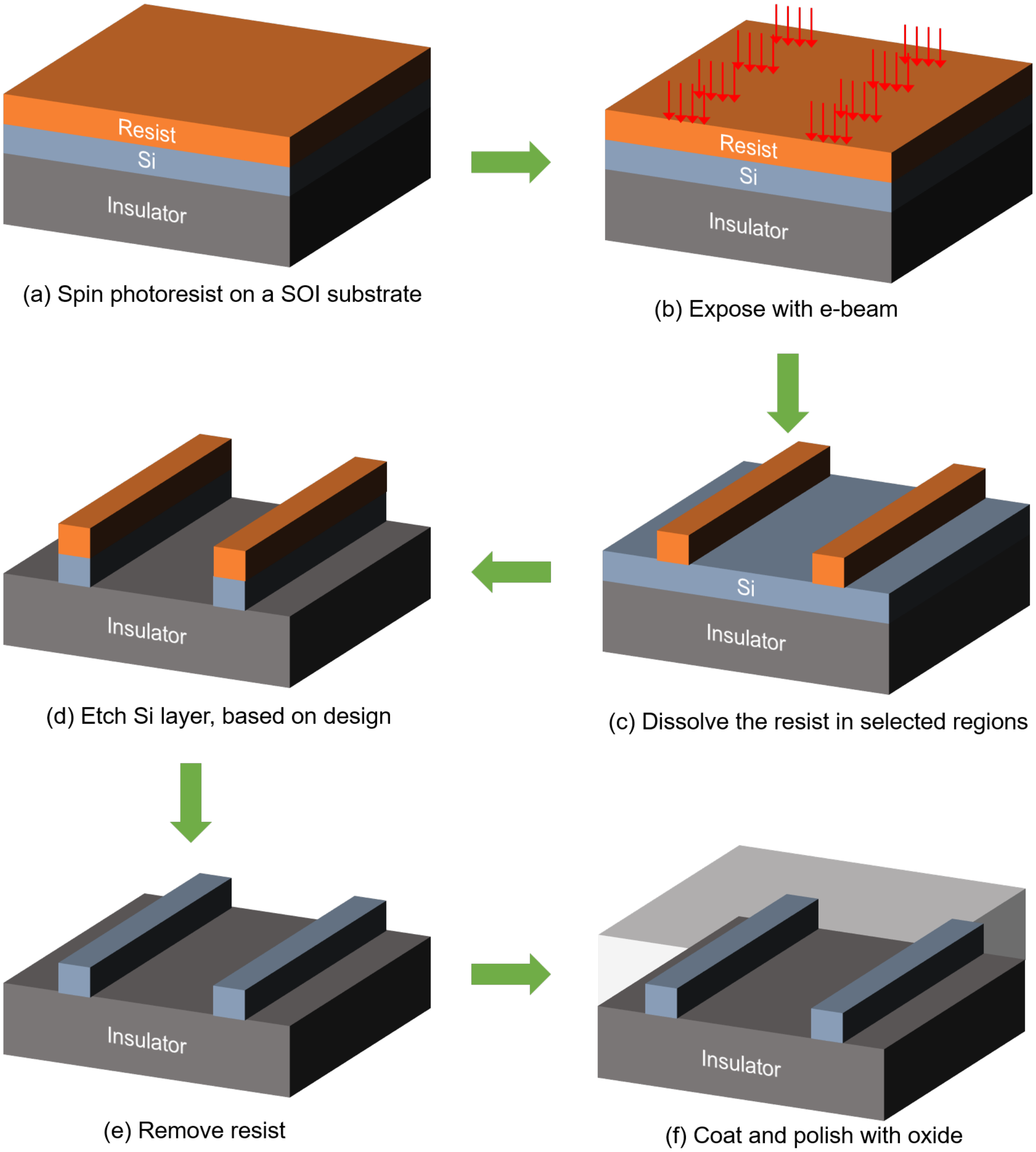

(a) Spin photoresist on a SOI substrate

(b) Expose with e-beam

(c) Dissolve the resist in selected regions

(d) Etch Si layer, based on design

(e) Remove resist

(f) Coat and polish with oxide

Figure 2.10: Silicon photonics fabrication steps: (a) After cleaning, photoresist (HSQ) was applied on the wafer. (b) The wafer then underwent e-beam lithography. (c) After exposure, the resist is dissolved in selected regions. (d) Based on design, parts of the top silicon layer are etched off. (e) After removal of resist, (f) a top layer of oxide is deposited.

2.3.3 Spin-coating of Resist

After cleaning and the application of an HMDS layer, the chips were then spin coated with Dow Corning XR1541-006 at 4500 rpm for 60 seconds, resulting in a layer between 90-120 nm of hydrogen silsesquioxane (HSQ). XR1541-006 is a type of flowable oxide composed of a 6% concentration of HSQ [94], which provides excellent etch resistance and is suitable to be used as a hard mask. It is also a negative resist requiring exposure along the waveguide themselves [95]. In addition, HSQ has the ability to make high contrast ratio structures resulting in nearly vertical waveguide sidewalls and to produce repeatable and reliable pattern definitions [95, 96]. After applying the resist, the chips were then baked at 80 °C for 4 minutes to ensure that all solvent was removed from the resist.

2.3.4 E-beam Writing

The pattern transfer was done utilizing a JEOL 6300FS electron-beam lithography tool [97] with a 100 kV acceleration voltage, a 2 nm spot size and 4 nA beam current. The pattern was created using Synopsys RSoft [98] that can convert the design file into the Graphic Data System (.gds) file. Layout BEAMER software [99] was used to transfer the .gds file containing the write pattern to the e-beam writer. It also featured Proximity Effect Correction, important for these waveguide structures, as the layer of HSQ acts as a charging layer that can distort and/or deflect the electron beam[99].

2.3.5 Pattern Development

After writing the pattern, the chips were then developed using a salty developer. The salty developer consisted of a mix of 1.5 grams of NaOH and 6 grams of NaCl in 150 mL of de-ionized (DI) water. The chips were subjected to a series of sonication steps during development [95]. After an initial placement in a bath of the salty developer and sonicated for 5 s, the chips were immediately removed from the bath and then placed into a second bath of salty developer and sonicated for 5 s. They remained in the second bath for 10 minutes for full development. After the second bath of salty developer, they were then placed in a bath of DI water, sonicated for 5 s, and remained in the water bath for another 10 minutes. The sonication steps were necessary to enure that all the stray particles landing on the chip were eliminated.

2.3.6 Etching

To selectively etch the top layer of silicon, SF_6/O_2 was used via a cryogenically cooled process at $-100 \ \circ C$ using Oxford Plasmalab etcher [100]. The process relies on reactive ion etching process that uses chemically reactive plasma to remove material deposited on wafers, in this case, silicon. The plasma is generated under low pressure (vacuum). High-energy ions from the plasma attack the wafer surface and react with it.

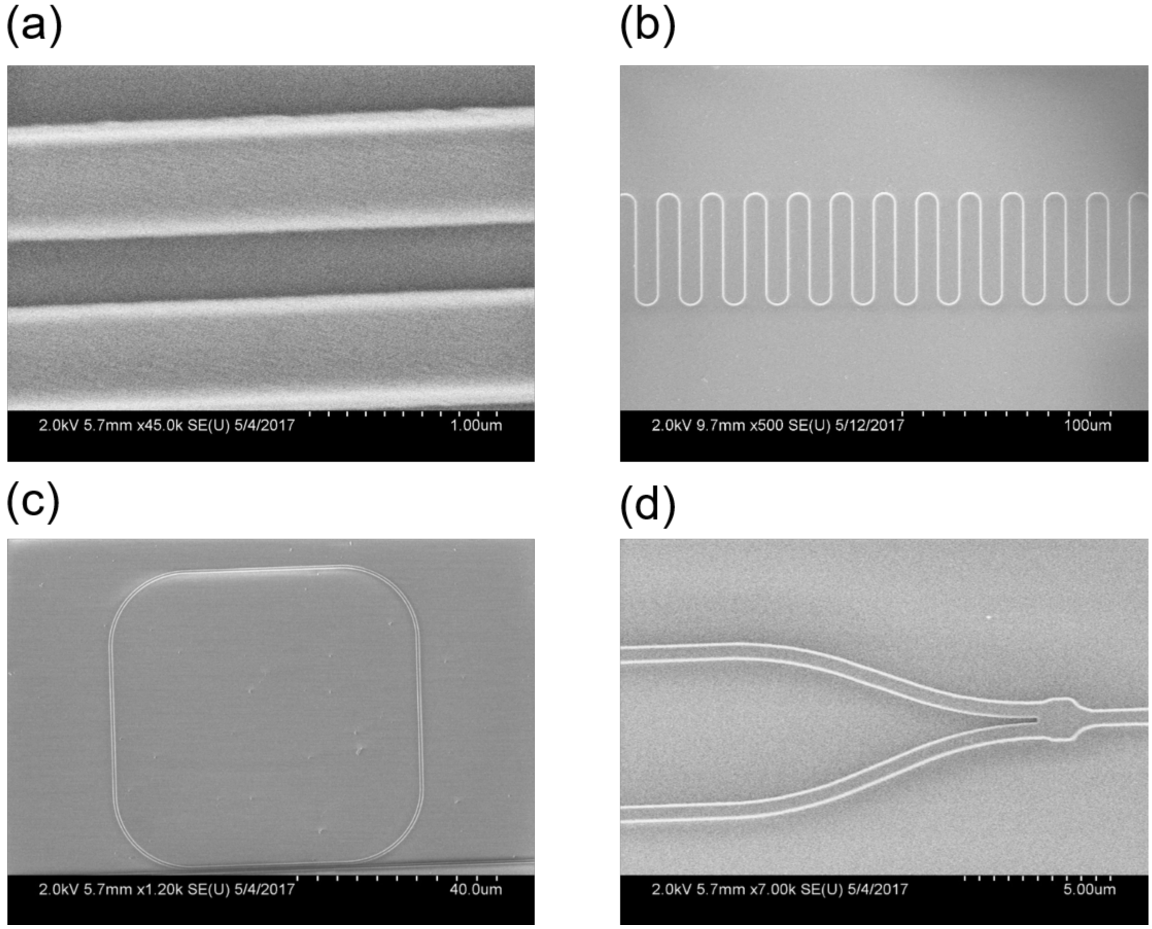

Figure 2.11: Scanning electron microscope images of (a) straight waveguide, (b) bent waveguide, (c) ring resonator, and (d) Y-splitter.

2.3.7 Oxide Deposition

The final step in the fabrication was to deposit a layer of SiO_2 through plasma enhanced chemical vapor deposition (PECVD) process using Trion Orion III PECVD tool [101]. This layer works as the top cladding of the silicon waveguides, while the buried oxide layer in the wafer works as the bottom cladding.

2.3.8 SEM Images

In Figure 2.11 we present the SEM images of several nano-photonic components fabricated using the above steps. The components were, namely, straight waveguide, bent waveguides, ring resonator, and Y-splitter. These elementary components were used to validate our design values. For example, from the straight waveguide, we can determine the absorption coefficient and thus the propagation loss inside the waveguide. The bent waveguide can give us an estimation of the bending loss. The ring resonator, which is in the core of the demodulator circuit used in Chapter 3, can tell us about the transmission spectrum, from which we can get the free spectral range. Also, we can measure the power-splitting ratio of the two arms from the basic Y-splitter.

Chapter 3

DPSK Demodulator using Coherent Perfect Absorption

3.1 Introduction

Differential phase shift keying (DPSK) has become a promising modulation format for on-chip optical communications. It offers several key advantages for data communication systems including improved resistance to nonlinear effects and a $\sim$ 3-dB enhanced sensitivity over that of intensity modulated direct detection (IMDD) systems [80, 102]. It also offers a relatively high extinction ratio and dispersion tolerance [103]. These advantages have led to DPSK-based transceivers being actively considered for short-haul optical communication systems. Many approaches to DPSK demodulation have been implemented, which include controlling the birefringence of a fiber loop mirror filter [104], employing a delayed path-length based Mach-Zehnder interferometer [105], and using a compact preamplified receiver based on Gaussian filtering [106].

Because of the aforementioned advantages, there has been a growing interest in moving toward a fully integrated chip-based systems for DPSK modulation and demodulation. Of the possible materials platforms for such integration, silicon photonics is particularly attractive due to its great potential for high quality large scale systems [29, 107, 108, 109]. Silicon-based microring (de)modulators, switches and filters, fabricated in silicon-on-insulator (SOI) platform, have been demonstrated previously [110, 111, 112, 113]. Recently, a Si photonic DPSK demodulation scheme based on ring resonators has been proposed. This scheme uses coherent perfect absorption (CPA) [81], where absorption in such a system can be coherently controlled by manipulating internal field interference by tuning the absorption and scattering loss of the ring resonator, which in turn modifies the critical coupling of the ring with bus and receiver waveguide [53, 82]. Such CPA-based devices have the advantages of independent switching of adjacent resonances, direct heterodyne detection, and smaller footprint over conventional methods that use periodically poled lithium niobate [82]. In addition, microring based structures are easy to fabricate into arrays which is essential for wavelength division multiplexed (WDM) systems.

In our previous works, we conceptually proposed a CPA based integrated optical modulator using a ring resonator [82] and experimentally demonstrated similar racetrack shaped resonator in SOI platform at telecom wavelengths [53]. In this chapter, we report the fabrication and testing of a fully integrated DPSK demodulator optical circuit. The chip is designed for a bit rate of 10 Gbps at C-band communication wavelengths using a 1-bit integrated delay line between the two bus waveguide inputs of the ring resonator. We measure this system at 10 Gbps and quantify its performance as a function of bit rate and symbol duty ratio (DR).

3.2 Device Physics

A schematic layout of photonic circuit is shown in Fig. 3.1 along with the experimental setup for characterization. Here the fundamental operating parameters are briefly laid out; a more extensive discussion of the design of this DPSK demodulator has been presented in literature [53, 82]. In particular, the input to the ring resonator is evenly split into two signals, with a phase shift ($\Delta\phi$) introduced into one of them by a delay line. The two signals are then coupled to the ring through the two bus waveguides. To achieve efficient power transfer between the ring and the waveguide, we must achieve the critical coupling condition [83, 84] that occurs when steady-state power coupling to the resonator from the two bus waveguides ($2\gamma_c$) equals the steady-state power loss rate inside the ring due to material absorption and scattering loss(γ_i). Under this condition, the transmitted signal drops to zero. In our device, we achieve the critical coupling condition by changing the gap between the waveguide and the ring, thereby controlling the coupling parameter (γ_c).

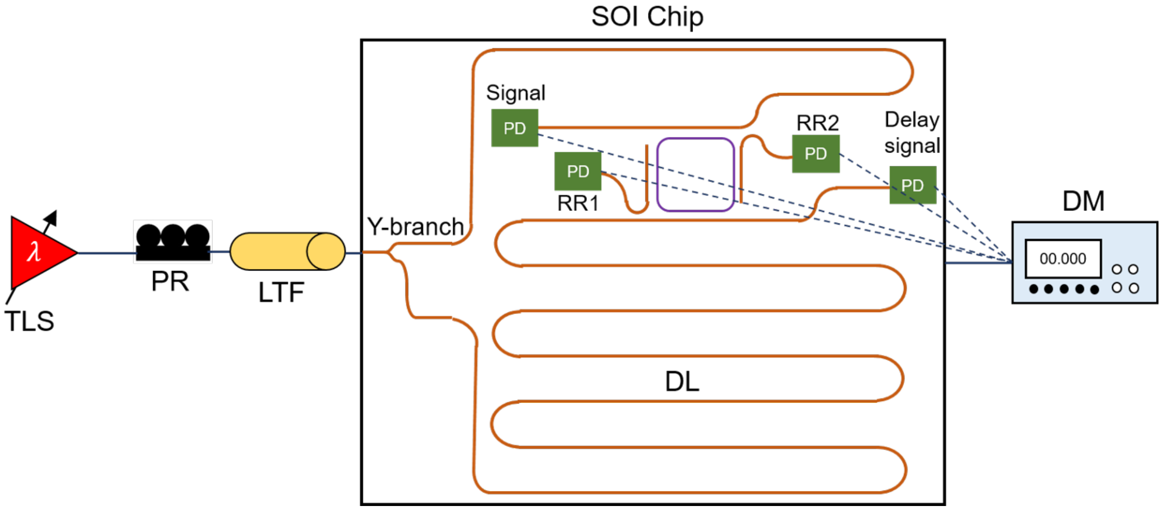

Figure 3.1: Experimental setup used to characterize the demodulator circuit. The input light from a tunable laser source (TLS) is edge coupled to the chip using a 2.5 μm spot lens-tapered fiber (LTF). A polarization rotator (PR) is used to maximize the current output. An inverted taper of 180 nm width is used to couple the light from the fiber to the SOI chip. The schematic of the photonic circuit shows the Y-branch where one signal branch is routed directly to the ring, while the other signal goes through a bit-rate-dependent delay line (DL). The two signals are coupled into the ring resonator. Four photodiodes (PDs) collect the photocurrent from the two signal buses and the two ring resonator ports. The photocurrents are measured using a digital multimeter (DM) through a 150 μm pitch electrical probe.

Using temporal coupled mode theory [83], we find that the steady state power transmission through any of the signal waveguides varies as [82]

$$P_{\text{signal}} = \frac{P_0}{2}\left(\frac{\gamma_c^2 + \frac{\gamma_i^2}{4} - \gamma_c\gamma_i\cos(\Delta\phi) + \Delta\omega^2 \pm 2\gamma_c\Delta\omega\sin(\Delta\phi)}{\Delta\omega^2 + \frac{1}{4}\gamma_{\text{tot}}^2}\right) \tag{3.1}$$

where $\Delta\omega = \omega - \omega_0$, ω is the angular frequency, ω_0 is the resonant angular frequency, and $\gamma_{\text{tot}} = 2\gamma_c + \gamma_i$ is the total loss rate of the cavity. Under the critical coupling condition ($\gamma_i = 2\gamma_c$) and on-resonance ($\Delta\omega = 0$), the above equation simplifies to [81, 82, 114] $P_{\text{signal}} = (P_0/2)\sin^2(\Delta\phi/2)$, while the power inside the ring varies as $P_{\text{RR1}} = P_{\text{RR2}} = P_0\cos^2(\Delta\phi/2)$ as shown in Fig. 3.2. Therefore, we make use of differential detection by measuring the relative phase change ($\Delta\phi$) between successive modulated phases of the received signal. A delay line is integrated into the chip that corresponds to one bit interval. The bit rate ($1/\Delta T$) is related to the phase difference through the length of the delay line (ΔL) and can be expressed as $\Delta\phi = 2\pi c\Delta T/\lambda n_g$, where c is the speed of light, λ is the resonant wavelength of the ring and n_g is the waveguide group index. The two signals are then coupled inside the ring resonator through CPA effect such that based on the value of the phase difference ($\Delta\phi$) of two successive bits, the demodulator will have power at either the bus waveguide or the ring itself.

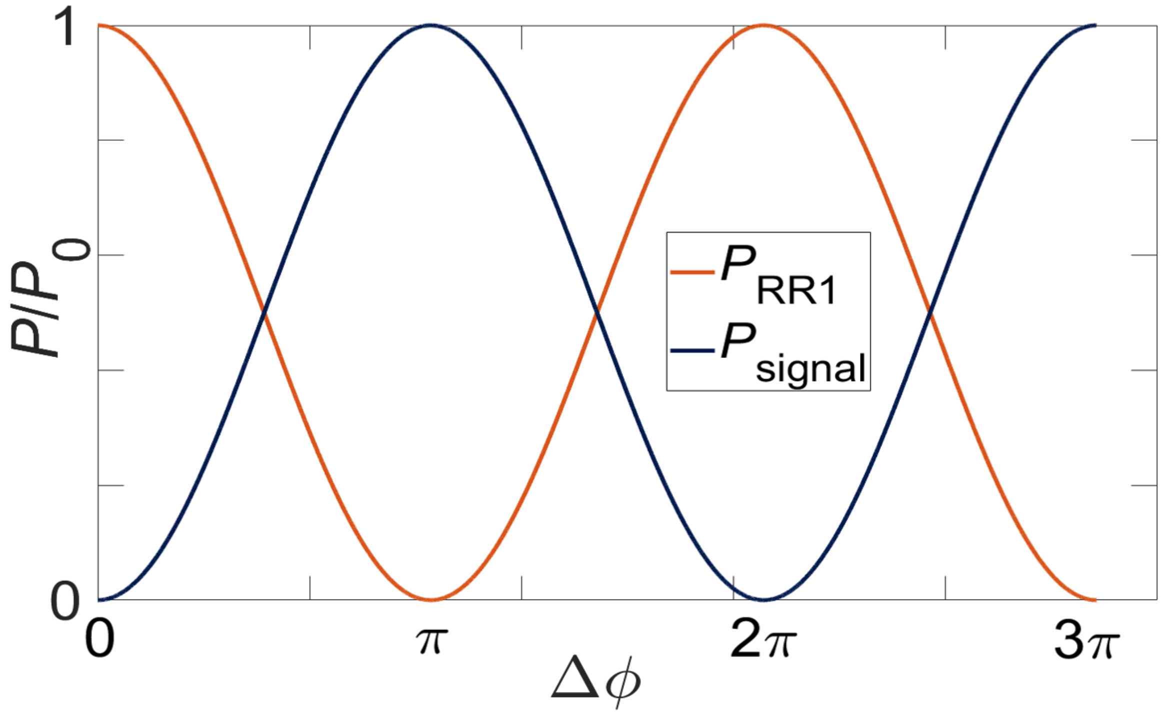

Figure 3.2: Calculated power transmission through the signal bus and the ring resonator as a function of phase shift ($\Delta\phi$).

The patterned circuit used here was fabricated in a commercial Si photonics foundry at the Singapore Institute of Microelectronics (IME). The structure is based on standard SOI technology consisting of a 220-nm thick silicon device layer and a 2 μm buried oxide (SiO_2) layer. The entire chip is clad with SiO_2. The waveguide and the ring are comprised of oxide-clad Si channel waveguides with cross-sectional dimensions of 500 nm × 220 nm. In Fig. 3.3, we plot the finite element method calculated (RSoft, FemSIM) value of the effective and group indices of the fundamental TE mode at communication wavelengths near 1.55 μm. The inset shows the mode profile at a wavelength of 1.55 μm where the effective index and group index are 2.43 and 4.14, respectively.

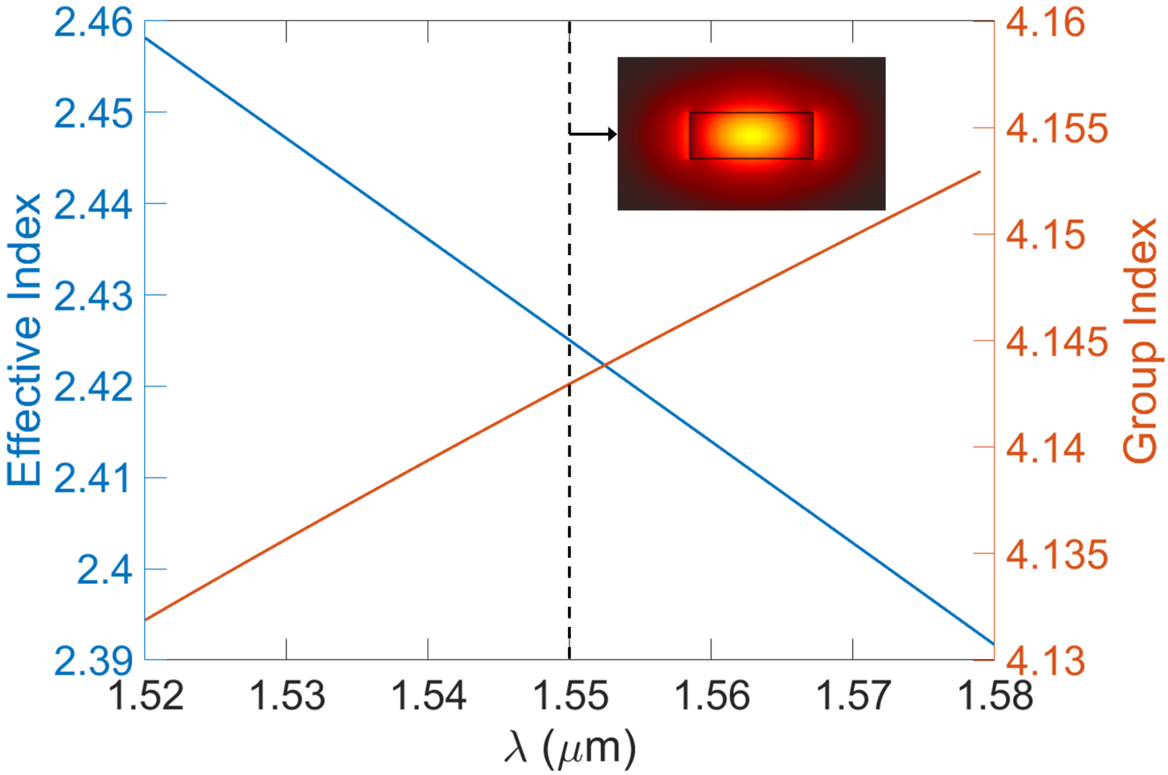

Figure 3.3: Effective and Group index for a Si waveguide of 500 nm× 200 nm cross-section, buried inside SiO_2. The inset shows the fundamental TE mode profile at a wavelength of 1.5 μm.

The loss coefficient α of the fundamental waveguide TE mode due to material absorption as calculated using RSoft FemSIM is 0.049 cm^{-1}. To first-order approximation, the loss rate is related to α according to $\gamma_i = 2\pi R\alpha v_g/L_{\text{tot}}$ and the coupling rate to the length of the coupling region (L_c according to $\gamma_c = \sin^2(\kappa L_c)v_g/L_{\text{tot}}$, where R is the radius of the ring, v_g is the group velocity, L_{tot} is the total linear length of the waveguide, and κ is the bus-to-resonator coupling coefficient [115]. Using a coupling gap of 434 nm, we find that the device is nearly critically coupled with $\gamma_i \approx 2.3\gamma_c$. The calculated delay based on the waveguide geometry and dispersion was ~ 0.1 ns, corresponding to a bit rate of 10 Gbps.

As shown in Fig. 3.1, a Y- branch and delay line (DL) are used to split the input signal into the two paths, such that a relative delay of one bit slot is imparted. Thus, the corresponding delay length ($\Delta L = c\Delta T/n_g$) for $1/\Delta T = 10$ Gbps is $\Delta T \approx 7.2$ mm. For detection of the DPSK signals, four identical Ge p-i-n photodiodes are incorporated onto the chip because of their high speed, broad detection spectrum and the compatibility of their processing (primarily thermal management in growth) compatibility with Si CMOS technology. The Ge-photodiode length has been reduced to increase the bandwidth of these photodetectors. Eight Al contacts were fabricated to measure the electrical photo current out of the chip. There are four 10 Gbps devices with varying gaps from 404-494 nm between the bus waveguides and the ring. This results into varying coupling coefficient (γ_c) values ranging from 2 cm^{-1} to 6 cm^{-1}. An optical microscope image of one of the fabricated devices is shown in Fig. 3.4. The device has a footprint of 1.26 mm × 0.72 mm. For higher bit rates, it can be smaller since the length of the delay line is inversely proportional to the bit rate.

3.3 Device Operation

To investigate *a priori* the DPSK demodulation behavior of our proposed structure, we perform 2D-FDTD simulations (RSoft, FullWAVE) using the on-chip dimensions of the ring. In this simulation, an arbitrary eight-bit sequence was launched into the structure, resulting in the powers shown (Fig. 3.5) for the photodiodes labeled signal and RR1 in Fig. 3.1.

When $\Delta\phi = 0$, the two inputs are identical and the ring is in CPA resonance condition,

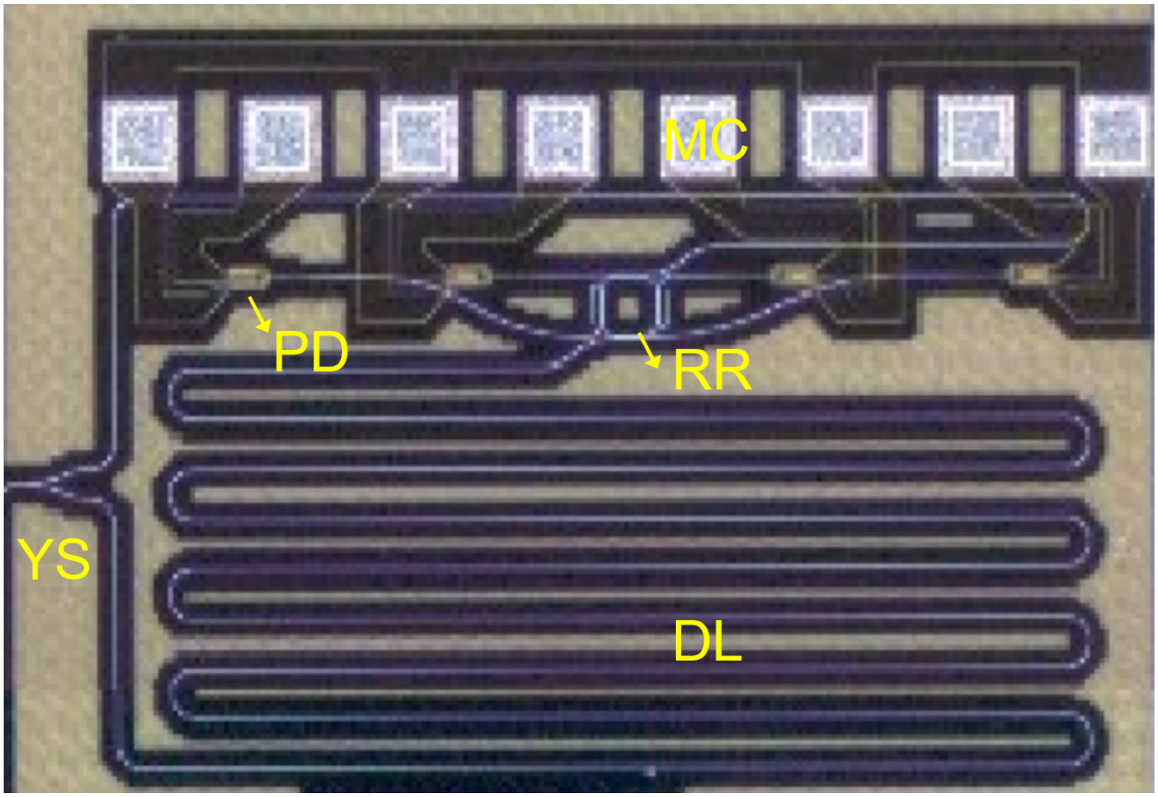

Figure 3.4: Optical Microscope Image of a 10 Gbps device. RR: Ring Resonator, DL: Delay Line, YS: Y-Splitter, PD: Photo Detector, MC: Metallic (Al) contact.

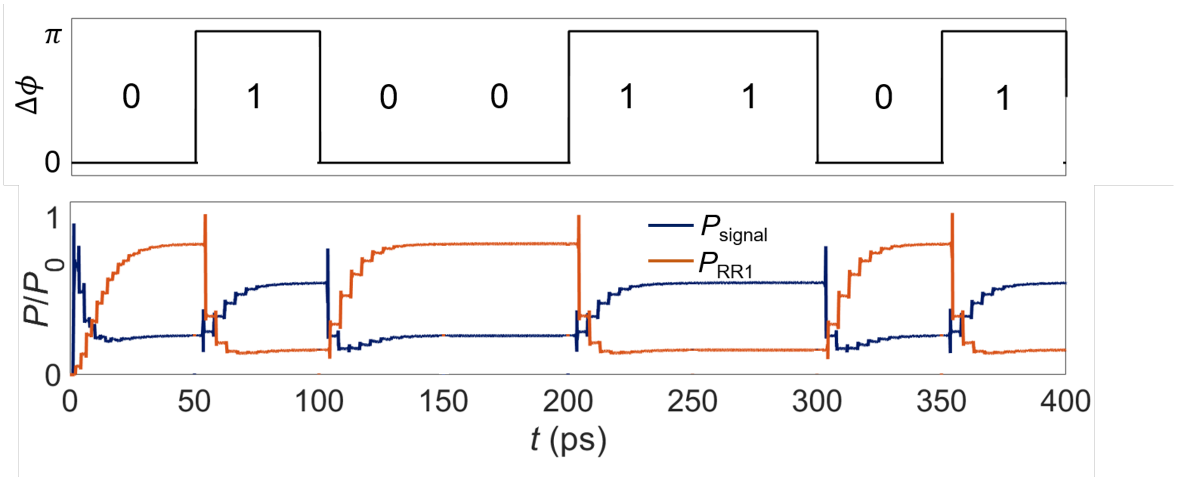

Figure 3.5: Theoretical DPSK bit sequence and simulated resultant power absorption. The blue curve represents power through the signal bus while the red curve represents power inside the ring. When $\Delta\phi = 0$, the two inputs are identical and the ring is in resonance resulting in full power loading of the ring and extinguishing power in the signal bus. This situation is reversed for $\Delta\phi = \pi$.

resulting in power absorption within the ring and nothing transmitted out of the signal bus. When $\Delta\phi = \pi$, the ring is not in CPA resonance condition and thus the power of the ring decreases and the transmitted power in the signal bus increases. Thus, for DPSK signals, where the bit information is stored inside the relative phase of the successive bits, this device can extract that information using the delay line and its RR-CPA response. The step response in the power signal corresponds to the stabilization of the round-trip transit time of the electric field inside the ring resonator. It is important to remember that the device is always in ring resonance condition ($\Delta\omega = 0$) in both cases. We differentiate between the two cases as ring resonance ($\Delta\omega = 0$) and CPA resonance $\Delta\phi = 0$. From prior discussion and Eq. 3.1, it is clear that ring resonance is a necessary condition for CPA resonance.

3.4 Device Characterization

Prior to high-frequency testing of DPSK demodulation, the transmission spectrum of the device was measured via the experimental setup outlined in Fig. 3.1. The measurement was performed with a continuous wave tunable laser source (TLS) (APEX AP3350A) set at 0 dBm and the polarization rotator was set to ensure maximum signal strength at the photodiodes. The input light from the TLS was edge coupled onto the chip using lensed-tapered fiber (LTF) that yields a 2.5 μm spot size. An inverted taper of 180 nm width was used to couple the light from the fiber to the 500 nm wide waveguide. The generated photocurrent was measured using a MATLAB program to control an APEX AP1000-8 Mainframe controller with an Agilent 34410A multimeter. A photograph of part of the experimental setup is shown in Fig. 3.6(a). Figure 3.6(b) shows a CCD image of the device under illumination. The propagation of 1.55 μm light through the delay line is clear from the figure as well as the photodetectors. At resonant condition, the ring is bright since most of the field is circulating inside it as shown in Fig. 3.6(c).

The resultant photocurrent transmission spectra are shown in Fig. 3.7 for the signal and

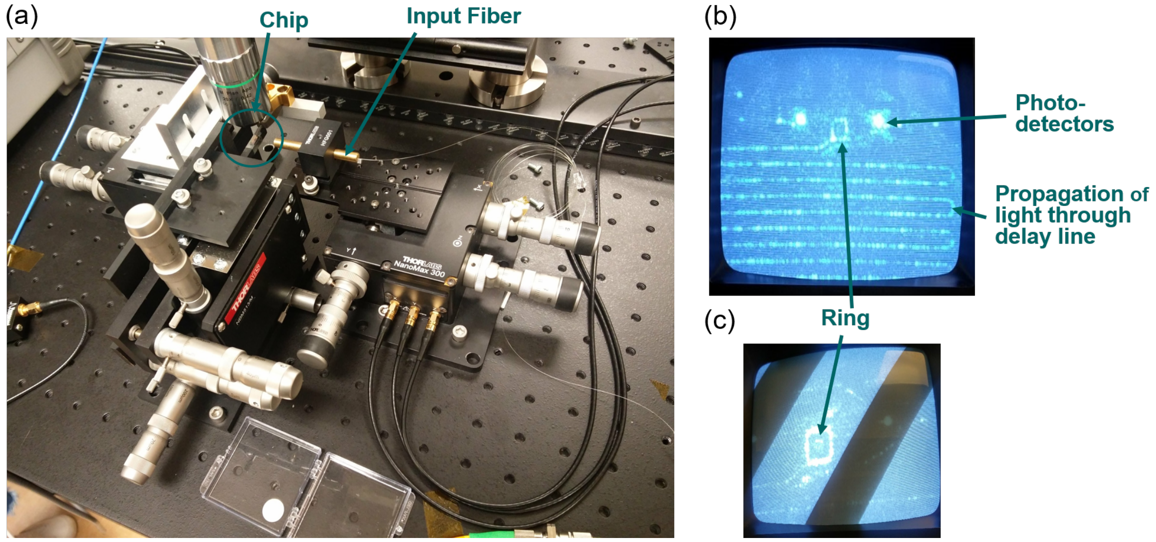

Figure 3.6: (a) Photograph of part of the experimental setup. The locations of the photonic chip and input lensed-tapered fiber are indicated. (b) The photonic chip under illumination with a 1.55 μm input signal. (c) Resonant condition of the resonator.

the RR1 ports with 0.02 nm resolution. With a group index (n_g) of 4.14 and a circumference (L) of 214.25 μm, the free spectral range (FSR) of the ring resonator is calculated to be ($\mathrm{FSR} = \lambda^2/n_g L$) 2.7 nm at $\lambda = 1.55$ μm. The calculated Q factor ($= \tau\omega_0/2$) for the ring resonator is obtained from the FDTD simulation of Fig. 3.5 to be 2.8 $\times 10^4$. From Fig. 3.7, the measured FSR is found to be 2.68 nm for a device with a 434 nm gap between bus and ring. The top-right inset of Fig. 3.7 shows a dip in the delay signal in the green shaded region of the figure with a 0.001 nm resolution. The measured quality (Q) factor of the ring ($= \lambda_{res}/\Delta\lambda$) as seen in the upper right inset of Fig. 3.7 is 3.2 $\times 10^4$, in good agreement with the calculated value.

In addition, the wavelength dependence of the phase difference between two arms is calculated to be -24.6π rad/nm based upon the usual expression $\frac{\partial}{\partial\lambda}\Delta\phi = -\frac{2\pi\Delta d}{\lambda^2} n_g$. Thus, the phase difference changes by 2π every 0.08 nm of wavelength, which agrees closely with the measured phase change of 0.07 nm from the photocurrent values as shown in the bottom-right inset of Fig. 3.7.

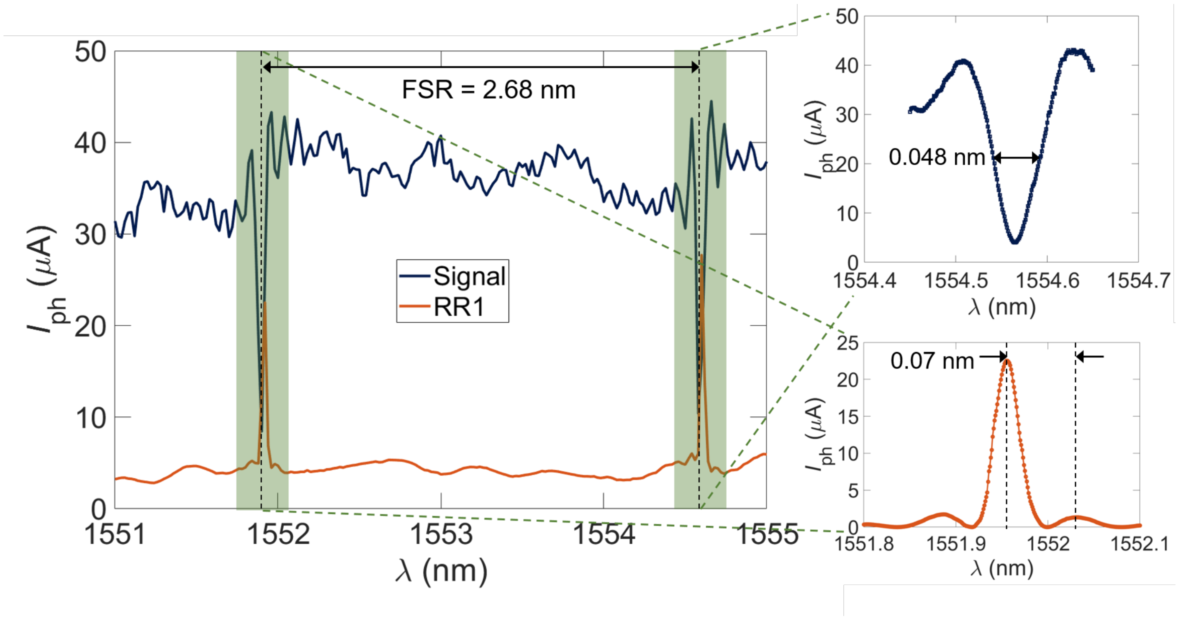

Figure 3.7: Measured photocurrent vs. wavelength for the signal and the RR1 port for a 10 Gbps device with a 434 nm bus and ring gap. The top right inset shows one resonant dip of the delayed signal port used to calculate the Q-factor of the device. The bottom right inset shows the photocurrent inside the ring used to calculate the wavelength change for a 2π phase shift.

3.5 Eye Diagram Measurement

In order to assess the quality of our demodulator circuit, the eye diagrams of the received signal were measured for different wavelengths, data rates and duty ratios. The experimental setup for eye extraction is shown in Fig. 3.8. In this set up, a pulse pattern generator is used to generate a random bit sequence with a bit pattern length of $2^{15}-1$ and a peak-to-peak voltage of 0.95 V at a particular clock frequency set by the clock signal generator. The bit sequence is fed to the phase modulator through a RF amplifier. RF amplification is required since the voltage required for the phase modulator for a π phase shift exceeds that available from the PPG; i.e., 7 V for the former vs 2 V for the latter. The phase modulator modulates the input optical phase based on the bit pattern. The laser light is fixed at a resonant wavelength of 1551.88 nm. For a ring of a given radius, the resonant wavelength leads to the best performance for demodulation. The light then passes through the chip so as to demodulate the encoded signal. The photodiodes are reverse biased at 1.34 V through a bias-tee for high speed operation. Also, the laser light is amplified by ~4 dB using an EDFA and optical grating filter before being its input to the chip.

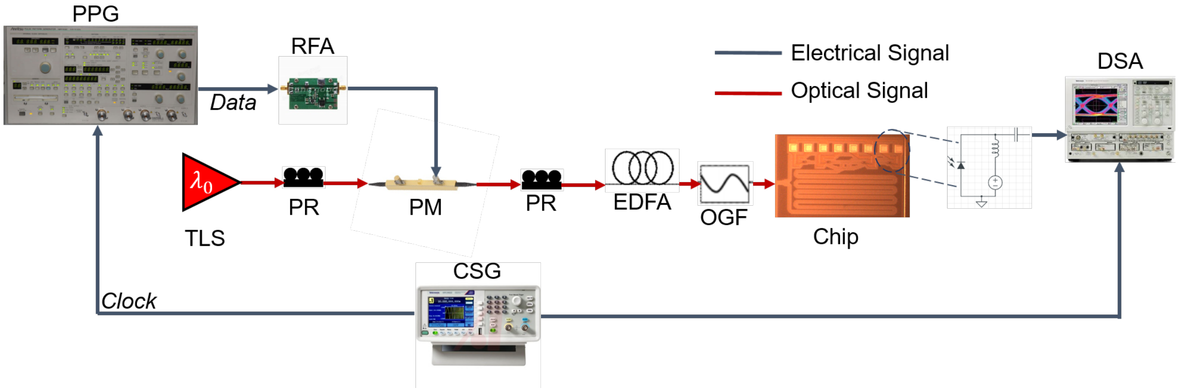

Figure 3.8: Experimental setup for eye diagram. PPG: Pulse Pattern Generator, RFA: RF Amplifier, TLS: Tunable Laser Source, PR: Polarization Rotator, PM: Phase Modulator, EDFA: Er-Doped Fiber Amplifier, OGF: Optical Grating Filter, CSG: Clock Signal Generator, DSA: Digital Serial Analyzer.

In Fig. 3.9, we plot the eye opening amplitude for eyes obtained at a data rate of $9-11$ Gbps with a 0.5 Gbps increment. Three typical eye diagrams after demodulation are shown in the insets of Fig. 3.9. As mentioned previously, the device was designed for a data rate of 10 Gbps. As the data rate deviates from this optimal rate, the eyes degrade and appear more closed and distorted. Note the rise and the fall times of this eye are ~0.09ns. These settings thus limit the device data rate to ~10 Gbps. This speed limitation comes from stabilization time of the ring and the LC or RC constant of the external electrical measurement system. The minimum BER and maximum extinction ratio occur at the designed data rates, i.e., 10 Gbps, which demonstrates the applicability of our device for high speed data rates. Note that shorter delay lines can be expected to yield data rates of 20 Gbps.

In addition to the frequency response of the eye diagrams, we also investigated their response to the relative abundance of the symbols in order to ensure that our device is demodulating differentially encoded signals rather than basic phase-shift encoded signal. The top eye diagram in Fig. 3.10 is obtained with a duty ratio, i.e., ratio of ‘1’ bit to ‘0’ bit in the randomly generated bit pattern of 50%. Operation under different duty ratios was then

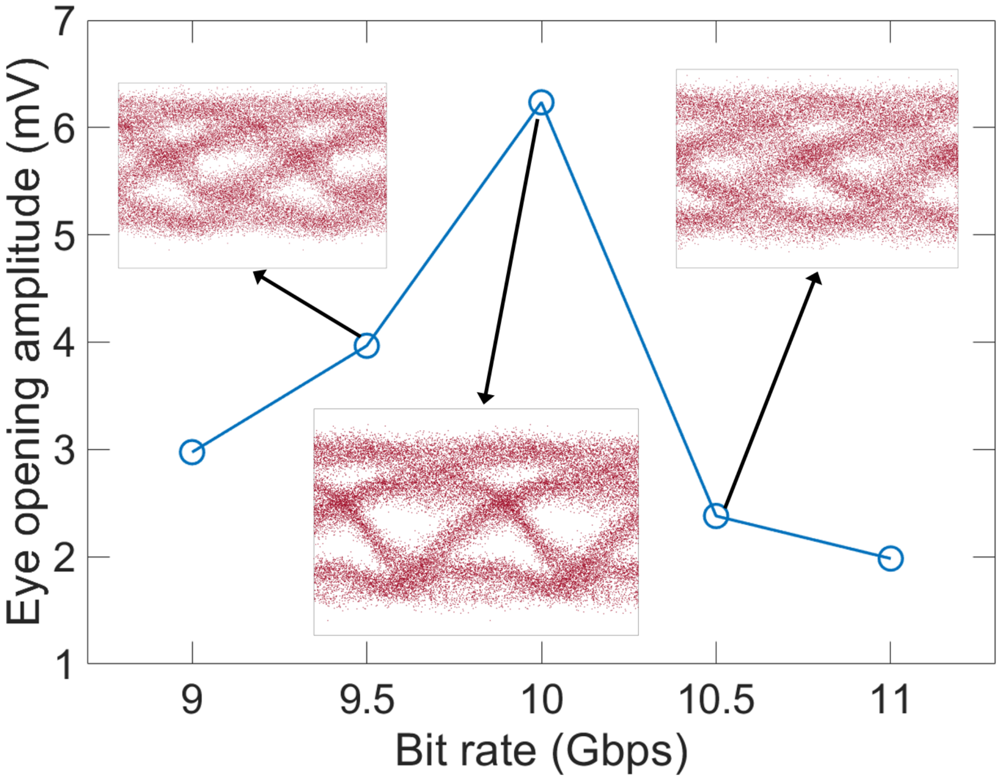

Figure 3.9: Tolerance of DPSK demodulator circuit to varied signal bit-rate. The minimum BER and maximum extinction ratio occurs at 10 Gbps, i.e., the designed value.

examined, namely, 75% and 87.5% by increasing the number of ‘1′ bits in the input bit stream. Since DPSK demodulation operates by decoding the message from phase difference of successive bits, it results in a higher number of ‘1′ bits than that of ‘0′ bits as shown in the bottom two eye diagrams of Fig. 3.10 for duty ratios of 75% and 87.5%, respectively. The resulting dependence of measured extinction ratio on the occupation ratio of bit ‘1′, as shown in Fig. 3.10, is weak. Finally, we attribute the rippled top (bit ‘1′) and bottom (bit ‘0′) of the eye diagrams to the electrical stabilization time of the ring. Note that this effect has also been described by Dong *et al.* [116]. This effect can be stabilized with an electrical filter.

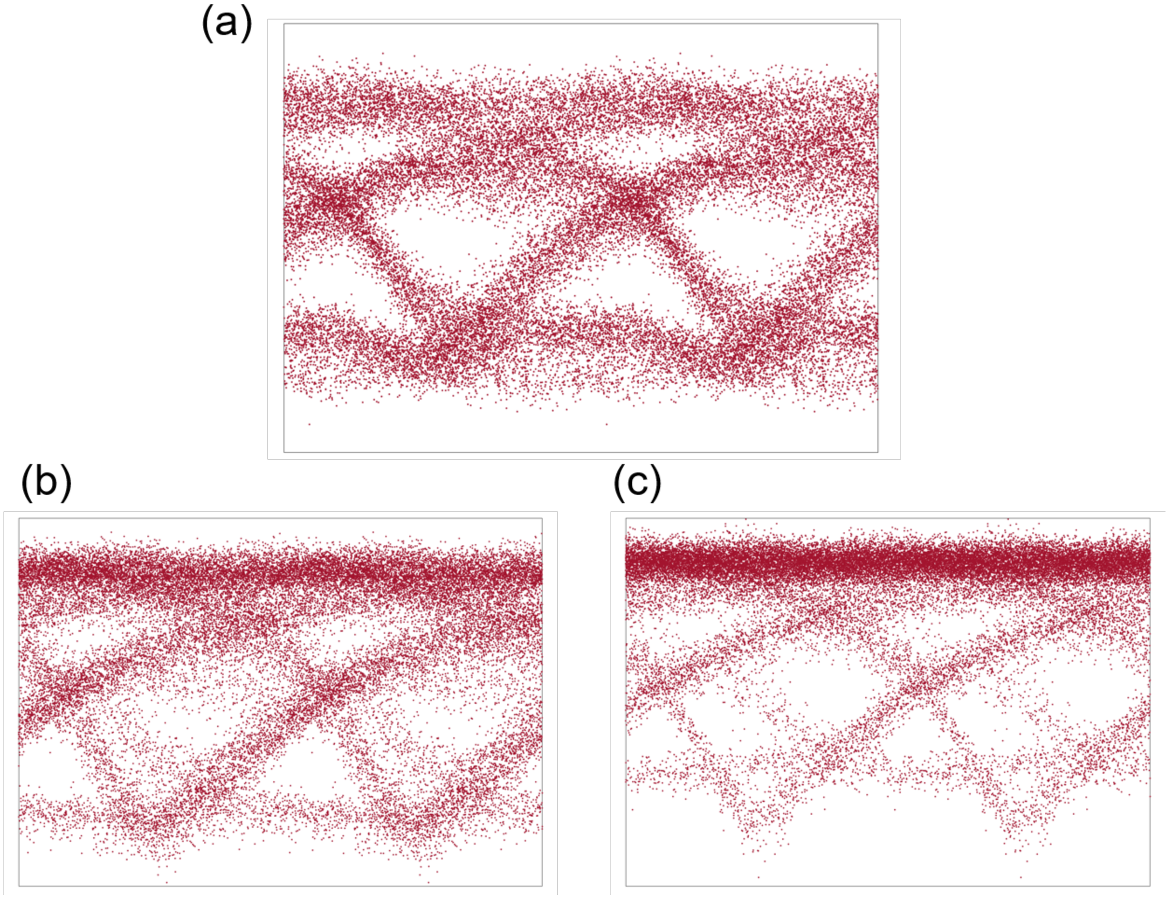

Figure 3.10: Eye diagrams with different duty ratios of (a) 50%, (b) 75%, and (c) 87.5%.

3.6 Concluding Remarks

The above results demonstrate the robustness of our DPSK demodulator at different input levels. Note that this characterization of this monolithic integration of the PD with a passive CPA DPSK-demodulator is done without the use of post chip electrical amplification. In addition, it is anticipated that the performance of the DPSK device can be further improved with the help of post processing. More generally, our results show clearly that coherent absorption can be used to realize a functional and robust demodulator method for high-speed data transport. Further, our results show that this device is readily fabricated in a commercial foundry.

Chapter 4

Non-Hermitian Signal Amplification via Four Wave Mixing

4.1 Introduction

In nonlinear optical processes that involve parametric mixing, phase matching is a key requirement for conversion efficiency [30]. However, due to several practical considerations, this condition cannot be easily satisfied in integrated optics semiconductor platforms. In typical silicon nanowire waveguides a typical phase matching bandwidth is $< 10\,\mathrm{nm}$ [117, 118]. Over the past few years, several novel technologies have been employed for implementing efficient phase matching in four-wave mixing(FWM) processes. These include for example, dispersion engineering in silicon nanowire waveguides [119, 120], width-modulation of Si photonic wires [121], graphene-silicon slow-light photonic crystal waveguides [122], intermodal FWM in few-mode fibers [123], using multiple exfoliated graphite nano-particles [124] and metamaterials [125]. However, these approaches often cause stringent geometric limitations on the optical waveguide dimensions and otherwise restrict the device functionality.

Recently, within the context of non-Hermitian photonics and parity-time (PT) symmetry

[126, 127], our groups have proposed an altogether new approach to overcome the aforementioned difficulties, essentially showing that the often cited phase matching criterion is not necessary to achieve efficient nonlinear interactions [128, 129]. Instead we showed that a careful engineering of the spectral distribution of the optical losses in the system can be utilized to build optical parametric amplifiers even without satisfying the usual phase matching condition [128, 129]. Furthermore, we have shown that our approach, which we call non-Hermitian phase matching, can work well in both second and third-order nonlinear optical processes [128, 129, 130]. More specifically, this idea relies on introducing losses only to the idler components while leaving the pump and signal waves intact. This in turn forces the nonlinear interaction to proceed only in one direction, which in the case of FWM is symbolically expressed as $2\omega_p \rightarrow \omega_s + \omega_i$ (two pump photons fuse and produce a signal and an idler photons). In the absence of idler losses, this process is reversible. However, if the idler photon is swept out of the system quickly, it becomes irreversible. In principle, there are several methods for introducing optical loss into the idler beam, for instance through out-coupling elements such as Bragg gratings designed to couple only the idler mode to radiation continuum [131] or absorptive material such as dopants, which absorb light only at the desired idler optical frequency [28]. Importantly, the introduction of losses may also alter the dispersive properties of the system and a successful device design must account for that.

A particular promising design that we considered recently is a structure based on a quasi-PT symmetric coupled waveguides where the nonlinear interaction occurs in one channel (the main channel) and the loss is introduced via coupling to the second (auxiliary channel) [129]. If the system is designed such as only the idler frequency couples to the auxiliary waveguide, then only the idler component will suffer from loss. We note that despite various recent studies on PT-symmetry concept, to our knowledge there has been no experimental works on parametric amplification via FWM process using the coupled-waveguide non-Hermitian phase-matching technique. Even though one could assume that this phenomenon can be readily observed in other phenomena, such as THz and supercontinuum generation, these processes would lack vital design element for signal gain, namely, addition of loss in a properly designed waveguide.

Encouraged by these preliminary results, here in this chapter, we first present the analytical results for both single and coupled medium and next we consider a variant of the coupler structure together with realistic material systems and we demonstrate that realizing optical parametric amplifiers based on non-Hermitian engineer is practically possible in silicon-based materials platform; this silicon photonics system is rapidly becoming an industry standard for many chip-scale photonics system. The novel hypothesis for silicon based photonic and optoelectronic integrated circuits is that these chip-scale networks, after going through careful design steps, will operate at a wavelength anywhere within a very broad spectral range of $1.2 - 100$ μm [2]. We focus on the nonlinear gain of the signal component to ensure that we achieve an observable level of gain to be considered as practical, similar to [132, 133, 134].

This chapter is organized as follows: We first briefly explain the theory behind non-Hermitian phase matching. Next we describe the material system, device structure, and mode profiles of the three fundamental waves, then we present extensive simulations results by using rigorous vectorial finite difference time domain (FDTD) calculations to confirm our predictions and demonstrate the feasibility of such device. This rigorous simulation allows us to perform detailed examination of realistic device implementations.

4.2 Theoretical Analysis

4.2.1 Single Medium

To add loss to the idler component, the equations in Sec. 2.1.3 are adjusted by adding a loss coefficient in the idler electric field equation. The three equations are then given by

(rewriting Δk as $\Delta\beta$)

$$\frac{dE_p}{dz} = i\kappa_p'[2E_sE_iE_p^*e^{-i\Delta\beta z} + E_p(|E_p|^2 + 2|E_s|^2 + 2|E_i|^2)], \tag{4.1}$$

$$\frac{dE_s}{dz} = i\kappa_s'[E_p^2E_i^*e^{i\Delta\beta z} + E_s(|E_s|^2 + 2|E_i|^2 + 2|E_p|^2)], \tag{4.2}$$

$$\frac{dE_i}{dz} = i\kappa_i'[E_p^2E_i^*e^{i\Delta\beta z} + E_i(|E_i|^2 + 2|E_s|^2 + 2|E_p|^2)] - \gamma_iE_i \tag{4.3}$$

where γ_i is the idler loss coefficient. In absence of γ_i, both the signal and idler beams oscillate between bounded values without any increase in the average amplification. With γ_i present, there is a net energy transfer from the pump to the signal beam and amplification takes place at the expense of reduction of the idler component.

We first consider the undepleted pump approximation, whereby $E_p \gg E_s, E_i$. Therefore, Eq. 4.1 becomes $\frac{dE_p}{dz} = i\kappa_p'|E_p|^2E_p$. If we assume the pump power is constant at its initial value, then $|E_p|^2 = E_{p0}^2$. Now, defining $\kappa_{p,s,i} = \kappa_{p,s,i}^{'}E_{p0}^2$, the above equations can be simplified as

$$\frac{dE_p}{dz} = i\kappa_pE_p, \tag{4.4}$$

$$\frac{dE_s}{dz} = i\kappa_s[E_i^*e^{i(\Delta\beta+2\kappa_p)z} + 2E_s], \tag{4.5}$$

$$\frac{dE_i}{dz} = i\kappa_i[E_s^*e^{i(\Delta\beta+2\kappa_p)z} + 2E_i] - \gamma_iE_i \tag{4.6}$$

In order to verify our results and gain more insight into the physics of the proposed scheme, we investigate its dynamical evolution under the relevant initial conditions. To do so, we first scale Eqs. 4.4-4.6 according to $\xi = z/z_0$, $\tilde{\kappa} = \kappa z_0$, $\Delta\tilde{\beta} = \Delta\beta z_0$, $\tilde{\gamma}_i = \gamma_iz_0$, $a_{p,s,i} = \eta_{p,s,i}^{-1}E_{p,s,i}/E_0$, and $\eta_{p,s,i} = \sqrt{\kappa_{p,s,i}^{'}z_0E_0^2}$, where z_0 and E_0 are arbitrary length scale and reference electric field parameters, respectively. After some algebraic manipulation and assuming $\eta_p^2|a_p| = 1$, the normalized equations, expressed in terms of scaled quantities, take the following form (under the undepleted pump approximation, the pump power remains constant and therefore, not written here),

$$\frac{da_s}{d\xi} = 2i\frac{\eta_s^2}{\eta_p^2}a_s + i\frac{\eta_s\eta_i}{\eta_p^2}a_i^* e^{i(\Delta\tilde{\beta}+2)\xi}, \tag{4.7}$$

$$\frac{da_i}{d\xi} = 2i\frac{\eta_i^2}{\eta_p^2}a_i + i\frac{\eta_s\eta_i}{\eta_p^2}a_s^* e^{i(\Delta\tilde{\beta}+2)\xi} - \tilde{\gamma}_i a_i \tag{4.8}$$

Figures 4.1 (a) and (b) depict the dynamic evolution of the signal and idler beams under undepleted pump approximation for two different values of the normalized loss coefficient for the initial conditions $a_s = 1$ and $a_i = 0$. All design parameters are explained in the figure caption. As explained, adding the loss coefficient can lead to amplification even when the system is not phase matched.

Next we consider the depleted pump approximation where the undepleted pump approximation no longer holds. In this case, following the aforementioned normalization, the pump, signal, and idler equations are given by

$$\frac{da_p}{d\xi} = i\left(\eta_p^2|a_p|^2 + 2\eta_s^2|a_s|^2 + 2\eta_i^2|a_i|^2\right)\eta_p^2 a_p + i\eta_s\eta_i\eta_p^2 a_s a_i a_p^* e^{-i\Delta\tilde{\beta}\xi}, \tag{4.9}$$

$$\frac{da_s}{d\xi} = i\left(\eta_s^2|a_s|^2 + 2\eta_i^2|a_i|^2 + 2\eta_p^2|a_p|^2\right)\eta_s^2 a_s + i\eta_s\eta_i\eta_p^2 a_i^* a_p^2 e^{i\Delta\tilde{\beta}\xi}, \tag{4.10}$$

$$\frac{da_i}{d\xi} = i\left(\eta_i^2|a_i|^2 + 2\eta_s^2|a_s|^2 + 2\eta_p^2|a_p|^2\right)\eta_i^2 a_i + i\eta_s\eta_i\eta_p^2 a_s^* a_p^2 e^{i\Delta\tilde{\beta}\xi} - \tilde{\gamma}_i a_i. \tag{4.11}$$

In Figs. 4.1 (c) and (d) we plot the optical intensities for this case for different design parameters as listed on the figure and in the caption. Here the initial conditions were assumed to be $a_{p,s,i} = 100, 1, 0$, respectively. Again we observe that adding the optical loss of the idler component can lead unidirectional energy conversion from the pump beam to the signal wave, while the absence of loss leads to oscillation.

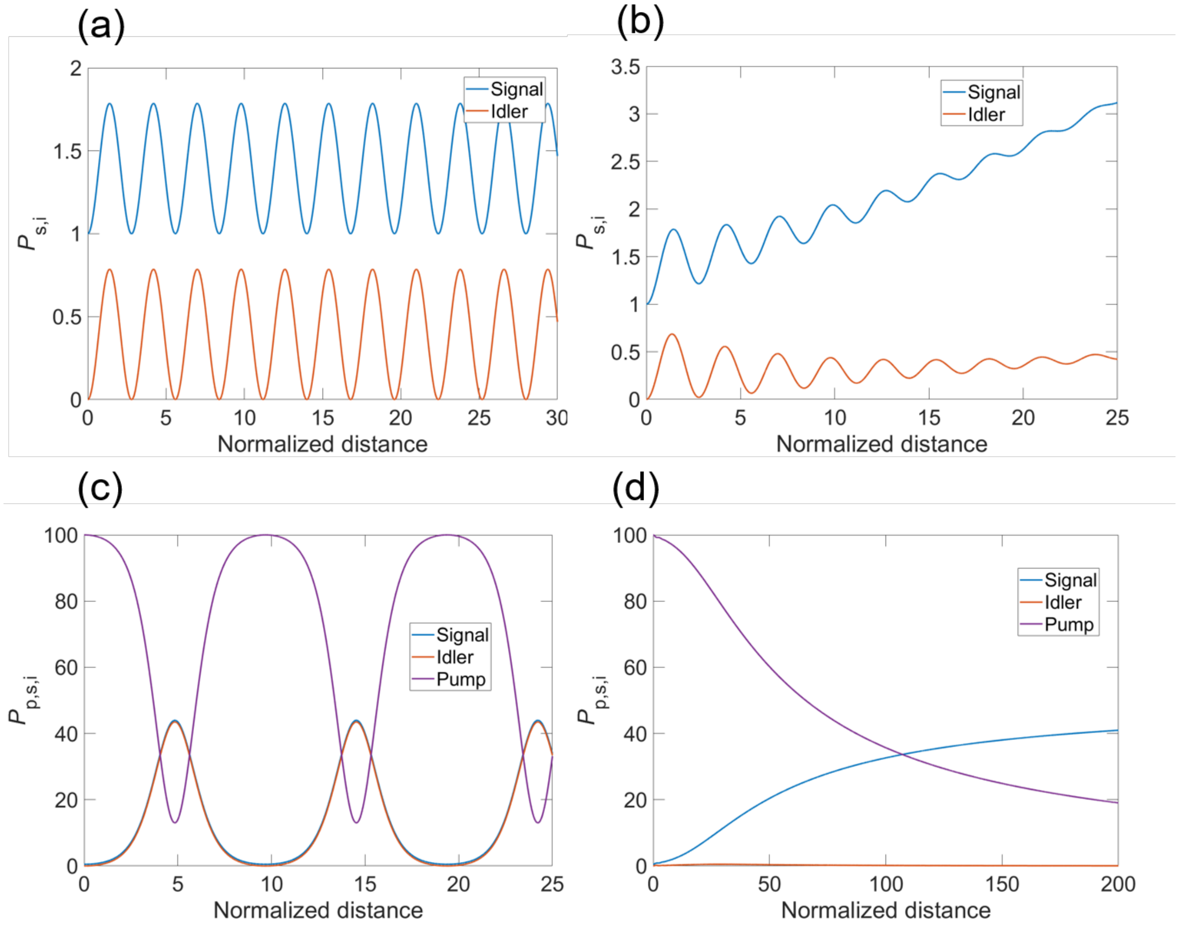

Figure 4.1: (a) and (b) Evolution of the normalized power of the signal (blue curve starting at one) and the idler (red curve starting at zero) beams under the undepleted pump approximation as a function of the normalized distance with the following different idler loss coefficients: (a)$\tilde{\gamma}_i = 0$ and (b)$\tilde{\gamma}_i = 0.1$. (c) and (d) Evolution of the normalized power of the pump (purple curve starting at 100), signal (blue curve starting at one) and the idler (red curve starting at zero) beams under the depleted pump approximation as a function of the normalized distance with the following different idler loss coefficients: (c)$\tilde{\gamma}_i = 0$ and (d)$\tilde{\gamma}_i = 0.5$. In all cases, $\Delta\tilde{\beta} = 5$. In our simulation, we assumed $\eta_p^2 |a_p| = 1$ and $\eta_{p,s,i}^2 = 0.1, 0.11, 0.09$, respectively, since $\eta_s^2 + \eta_i^2 = 2\eta_p^2$ according to $\omega_s + \omega_i = 2\omega_p$.

4.2.2 Coupled Medium

Next we investigate in detail a particular implementation of non-Hermitian parametric amplifiers based on quasi-$\mathcal{PT}$ symmetric coupled waveguide structures. As shown in Fig. 4.3, the system consists of two coupled asymmetric waveguides. The nonlinear interaction takes place in one of them (say the left one) which we will call the nonlinear guide. The second channel is designed to support a mode that matches only the idler component. Thus by introducing optical loss to this second waveguide, one can provide a dissipative coupling to the idler wave. Thus effectively, the nonlinear waveguide together with the reservoir channel constitute a passive $\mathcal{PT}$ symmetric structure [135] for the idler component.

Within the context of linear coupled mode theory between two waveguides and the nonlinear coupled wave analysis between the different components of the three wave mixing process, the system can be described by [30]

$$\frac{dE_p}{dz} = i\kappa'_p[2E_sE_iE_p^* e^{-i\Delta\beta z} + E_p(|E_p|^2 + 2|E_s|^2 + 2|E_i|^2)], \tag{4.12}$$

$$\frac{dE_s}{dz} = i\kappa'_s[E_p^2E_i^* e^{i\Delta\beta z} + E_s(|E_s|^2 + 2|E_i|^2 + 2|E_p|^2)], \tag{4.13}$$

$$\frac{dE_i}{dz} = i\kappa'_i[E_p^2E_i^* e^{i\Delta\beta z} + E_i(|E_i|^2 + 2|E_s|^2 + 2|E_p|^2)] + i\kappa'_d E_d, \tag{4.14}$$

$$\frac{dE_d}{dz} = -\gamma_d E_d + i\kappa'_d E_i, \tag{4.15}$$

where γ_d is the linear loss coefficient associated with the dissipative mode and κ'_d is the linear coupling between the idler and the dissipative modes.

As in the case of single medium described in Sec. 4.2.1, the above equations can be normalized using the same coefficients for both the undepleted and depleted cases as follow:

Undepleted Pump Approximation:

$$\frac{da_p}{d\xi} = ia_p, \tag{4.16}$$

$$\frac{da_s}{d\xi} = i\frac{\eta_s\eta_i}{\eta_p^2}a_i^* e^{i(\Delta\tilde{\beta}+2)\xi} + 2i\frac{\eta_s^2}{\eta_p^2}a_s, \tag{4.17}$$

$$\frac{da_i}{d\xi} = i\frac{\eta_s\eta_i}{\eta_p^2}a_s^* e^{i(\Delta\tilde{\beta}+2)\xi} + 2i\frac{\eta_i^2}{\eta_p^2}a_i + i\tilde{\kappa}_d a_d, \tag{4.18}$$

$$\frac{da_d}{d\xi} = -\tilde{\gamma}_d a_d + i\tilde{\kappa}_d a_i. \tag{4.19}$$

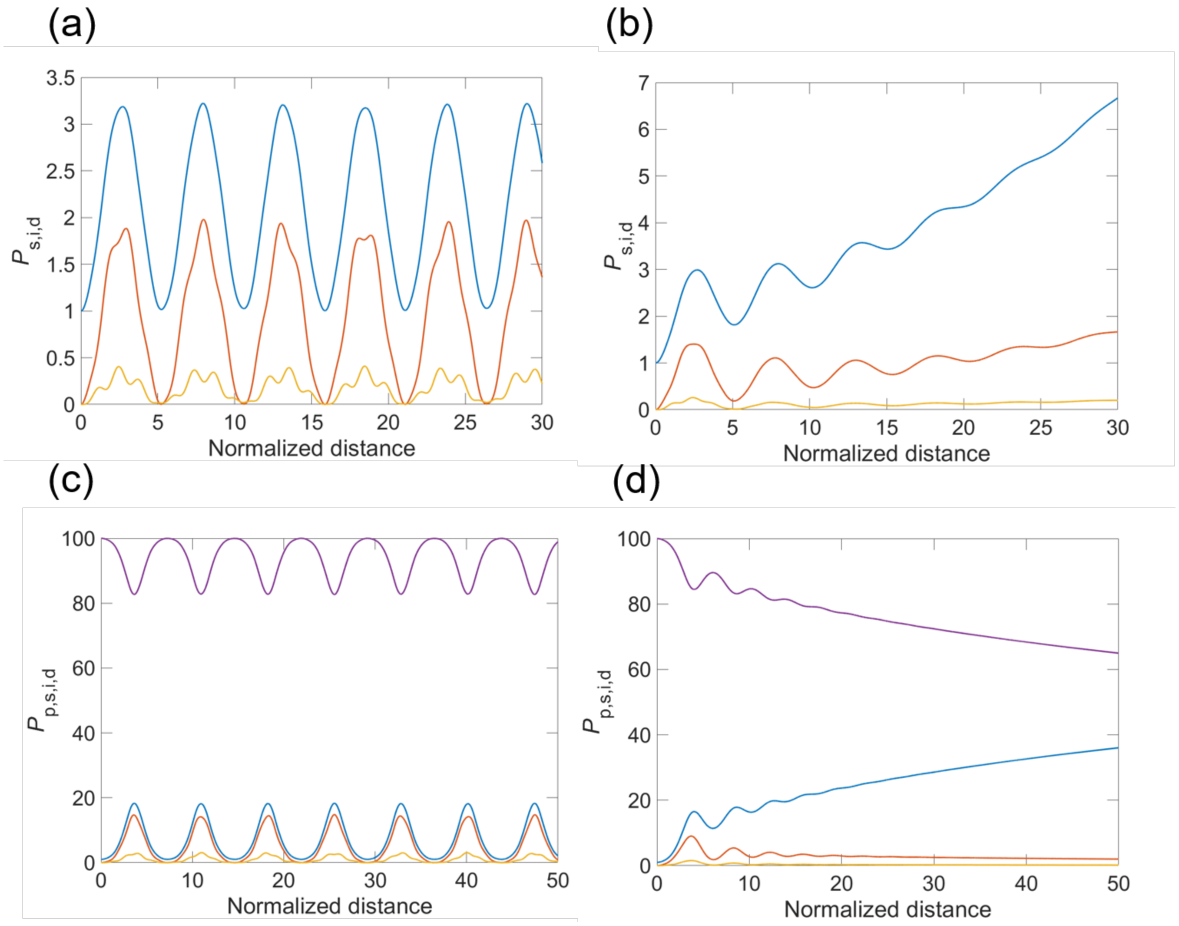

Figure 4.2: (a) and (b) Undepleted pump approximation for coupled-waveguide system: Evolution of the normalized power of the signal (blue curve starting at one), idler (red curve starting at zero), and auxiliary (orange curve starting at 0) beams as a function of the normalized distance with the following different idler loss coefficients: (a)$\tilde{\gamma}_d = 0$ and (b)$\tilde{\gamma}_d = 0.5$. In both cases, $\Delta\tilde{\beta} = 5$ and $\kappa_d = 1.5$. (c) and (d) Depleted pump approximation for coupled-waveguide system: Evolution of the normalized power of the pump (purple curve starting at 100), signal (blue curve starting at one), idler (red curve starting at zero), and auxiliary (orange curve starting at 0) beams as a function of the normalized distance with the following different idler loss coefficients: (a)$\tilde{\gamma}_d = 0$ and (b)$\tilde{\gamma}_d = 1$. In both cases, $\Delta\tilde{\beta} = 4$ and $\kappa_d = 1.5$.

Depleted Pump Approximation:

$$\frac{da_p}{d\xi} = i\left(\eta_p^2|a_p|^2 + 2\eta_s^2|a_s|^2 + \eta_i^2|a_i|^2\right)\eta_p^2 a_p + i\eta_s\eta_i\eta_p^2 a_s a_i a_p^* e^{-i\Delta\tilde{\beta}\xi}, \tag{4.20}$$

$$\frac{da_s}{d\xi} = i\frac{\eta_s\eta_i}{\eta_p^2} a_i^* e^{i\left(\Delta\tilde{\beta}+2\right)\xi} + 2i\frac{\eta_s^2}{\eta_p^2} a_s, \tag{4.21}$$

$$\frac{da_i}{d\xi} = i\frac{\eta_s\eta_i}{\eta_p^2}a_s^* e^{i\left(\Delta\tilde{\beta}+2\right)\xi} + 2i\frac{\eta_i^2}{\eta_p^2}a_i + i\tilde{\kappa}_d a_d, \tag{4.22}$$

$$\frac{da_d}{d\xi} = -\tilde{\gamma}_d a_d + i\tilde{\kappa}_d a_i. \tag{4.23}$$

The above equations are plotted in Fig. 4.2 for different conditions as mentioned in the caption. We note that the presence of the loss coefficient for the idler component always leads to signal amplification even in the absence of standard phase matching condition.

The evolutions of Figs. 4.1 and 4.2 were solved in temporal discretization using an unsymmetrical formula, namely fourth-order Runge-Kutta method. To achieve sufficient accuracy in the solution with minimum computational effort, we also employ adaptive step size control that results into step error several orders of power smaller than the correction.

4.3 Materials system and photonic structure

Now, we use full-vectorial FDTD technique to validate our analytical solution by considering silicon material system with realistic design parameters. As we mentioned in the introduction, several techniques can be employed to implement non-Hermitian wave mixing devices. *To date however, there has been a dearth of studies directed toward realizing such devices with a practical and well characterized photonic materials platform.* Here, motivated by the current commercial interest in Si photonics, we bridge this gap and investigate non-Hermitian parametric amplifiers in Si optical nanowires (with widths and heights on the order of several hundreds of nanometers). Particularly, the very large $\chi^{(3)}$ in this system (nearly three orders higher than silica glass) reduces the threshold for a variety of parametric processes.

To this end, we consider the process of third-order nonlinear interaction between a pump ($\lambda_p = 2\mu$m), a signal ($\lambda_s = 1.2\mu$m) and an idler ($\lambda_i = 6\mu$m) waves in the structure shown schematically in Fig. 4.3. It consists of two identical coupled Si waveguides surrounded by SiO_2 cladding. Each channel is 0.5 μm wide × 1.5 μm height; separation between the waveguides is of the order of few hundred nanometers. As we will see shortly, these dimensions allow only the idler component to tunnel from the main waveguide to the auxiliary channel with negligible coupling for the pump and signal. We note that in the absence of phase matching constraint, several other FWM components will be generated. However, all these components fall into the opaque window of silicon and therefore, they are being absorbed continually as they are being generated and propagating inside the waveguide. The refractive index of Si at the pump, signal and idler frequencies is $n_p = 3.45 + i7.271 \times 10^{-7}$, $n_s = 3.52 + i1.511 \times 10^{-6}$ and $n_i = 3.42 + i4.147 \times 10^{-7}$, respectively. In order to implement loss, the auxiliary waveguide is subject to an extra treatment that modifies the loss of that waveguide. This is readily implementable by various methods either via passive or active means. For passive cases, we can use material doping as mentioned in [28, 32] or via Si^+ implantation to form well defined defect states [136]. Active methods involve carrier injection by electrical or optical methods [137]. It is important to point out here that the loss only occurs in the auxiliary waveguide. Unlike the idler, the pump and signal waves are essentially uncoupled to the auxiliary waveguide thus the bandwidth of the loss in the auxiliary is immaterial, provided that the minimum bandwidth of the loss is equal to the linewidth of the idler beam. Once this condition is achieved it then becomes important that this loss becomes controllable.

Importantly, we note that Si does have a non-negligible two photon absorption (TPA) coefficient (β_{TPA}). However, at a wavelength of 2 μm (the pump wavelength in our simulations), the two-photon absorption coefficient is relatively weak, $\beta_{\mathrm{TPA}} \approx 0.3$ cm/GW [138]. Additionally, in our work, the pump intensity is low enough ($I_p \approx 3 \times 10^{-3} \mathrm{GW/cm}^2$) such that $\beta_{\mathrm{TPA}} I_p \approx 9 \times 10^{-4} \mathrm{cm}^{-1} \ll \alpha_p$, where $\alpha_p \equiv 4\pi \mathrm{Im}(n_p)/\lambda_p = 0.047\ \mathrm{cm}^{-1}$ is the bulk Si absorption coefficient at the pump wavelength. Thus we can safely neglect TPA in our simulations. More detailed discussions on the linear and nonlinear optical properties of Si-wire waveguides can be found in [29, 107, 139].

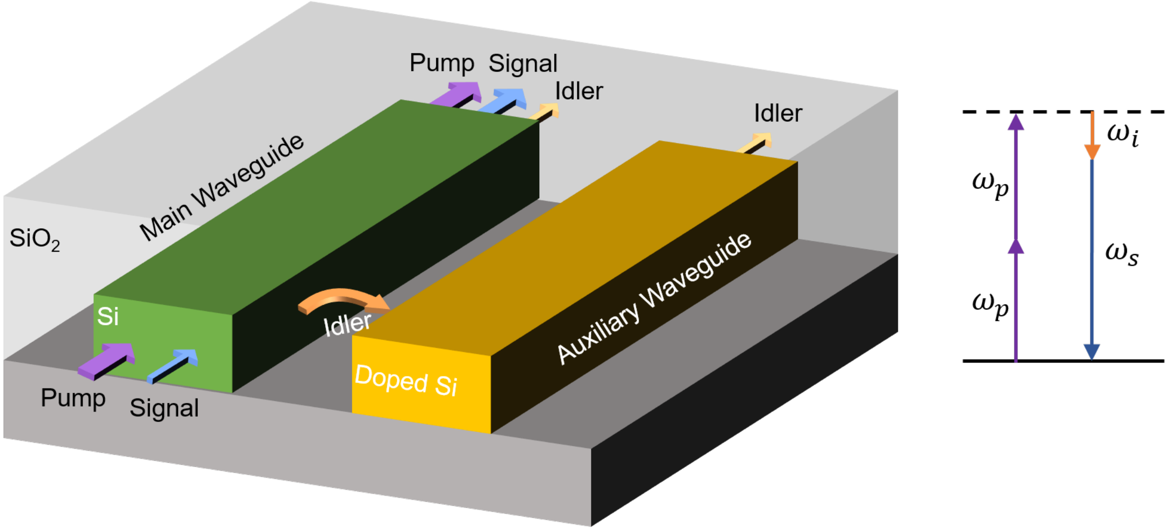

Figure 4.3: Schematic diagram of our optical parametric amplifier using a quasi-PT symmetric coupled-waveguide structure, consisting of a main waveguide and an auxiliary waveguide. Both pump and signal beams are launched into the main waveguide. Only the idler, incipiently generated in the main waveguide through the four-wave mixing (FWM) process, is coupled to the auxiliary waveguide. The auxiliary waveguide is lossy; this property has a two-fold objective: (1) to introduce loss into the secondary waveguide, which prevents coupling of the idler back to the main waveguide, and (2) to allow tunability of the degree of non-Hermiticity of the system, which will permit optimization of the signal gain. The inset denotes the quantum mechanical process of FWM.

4.4 Device Simulations

In this section, we present our computational results using vectorial full-wave analysis. These simulations are obtained by first using the effective index method to reduce the 3D structure into 2D, then performing FDTD. We first start our analysis by considering only the main waveguide in isolation, i.e., without coupling to the auxiliary channel. The left panel of Fig. 4.4 depicts the linear phase mismatch (blue line) between the different modes, as defined by $\Delta\beta = 2\beta_p - \beta_s - \beta_i$, where $\beta_{p,s,i}$ are the propagation constants of the pump, signal and idler waveguide modes, respectively. However, if we consider nonlinearity of the system induced by self-phase modulation and cross-phase modulation due to material nonlinear coefficient, the phase-matching condition must be modified to account for this variation [29] and becomes $\Delta\beta_{\text{total}} = \Delta\beta_{\text{NL}} - \Delta\beta$. The black dotted line indicates the nonlinear contribution to the phase mismatch and is given by $\Delta\beta_{\text{NL}} = 2\gamma P_p$ where $\gamma = n_2/\lambda_p A_{\text{eff}}$, where n_2 is the nonlinear refractive index and A_{eff} is the effective mode area [140]. The intersections of the two curves denote the phase-matching signal wavelengths for this geometry. The inset shows the nonlinear propagation in a single waveguide as calculated using FDTD for the frequencies defined in the previous section. Clearly, the strong phase mismatch prevents a net energy transfer between the interacting modes. The right panel plots the vertical (quasi-TM) electric field components associated with the mode profiles for the three different components.

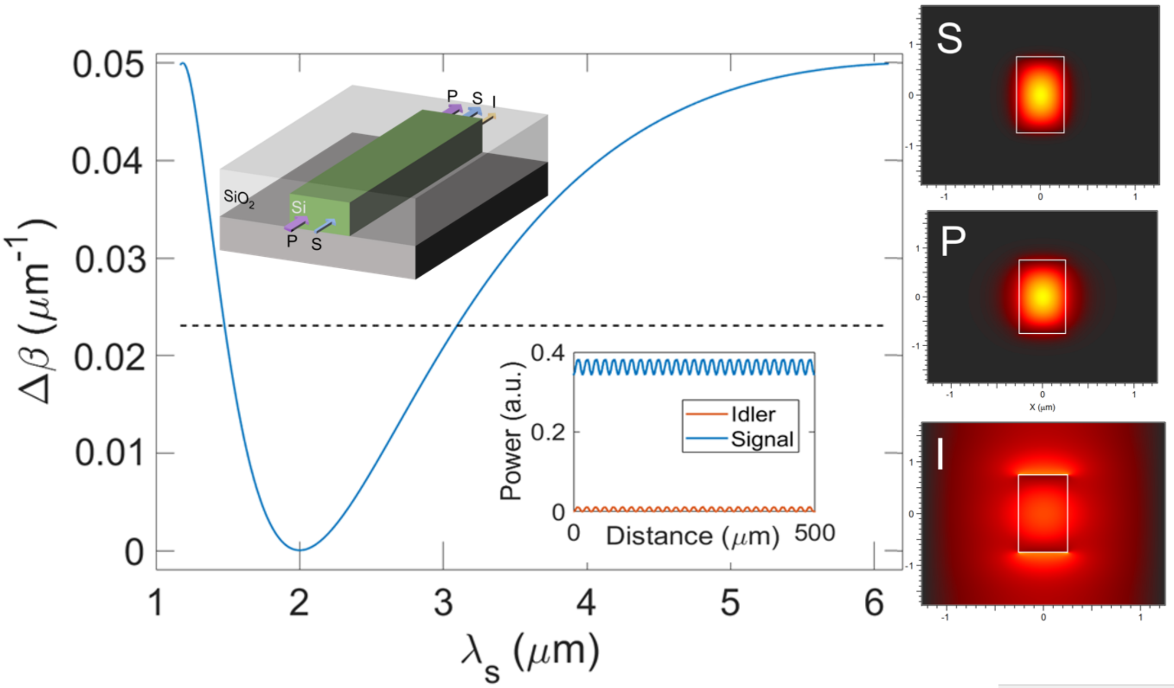

Figure 4.4: Wave-vector mismatch, $\Delta\beta$, as a function of the signal wavelength for the case of a single waveguide. The inset inside the main panel shows FDTD calculations indicating the evolution of the signal and idler beams through the main waveguide in the phase-mismatched case with a signal wavelength of 1.2 μm without any net amplification. The black dashed line is associated with the pump-power-induced nonlinear phase-mismatch term. The intersections of this line with the blue curve denote the phase-matching signal wavelengths for this geometry. The right-hand-side figures, from top to bottom, show the mode profile of the signal (1.2 μm), pump (2 μm), and idler (6 μm) waves.

Having carried out FWM analysis in an isolated waveguide, we now consider the combined coupled structure. Figure 4.5 plots the coupling coefficients for the three wave components as a function of the separation between the two waveguides. Clearly, the idler component experiences strong coupling while the signal and pump components experience very weak coupling. This is also evident from the mode profiles in Fig. 4.4 where the field distribution of the idler field extends considerably outside the waveguide. In the rest of this work, we will focus on a design having a separation gap of 0.5 μm, which yields the coupling coefficients $\kappa_{p,s,i}$ of values 6, 0.1, and 250 cm^{-1} respectively. These values correspond to coupling lengths of L_p=2.6 mm, L_s=16 cm, and L_i= 63 μm, associated with the pump, signal, and idler, respectively. Thus for a device length of few hundred microns, we can safely ignore the effects of the coupling for the pump and signal components and focus only on that of the idler.

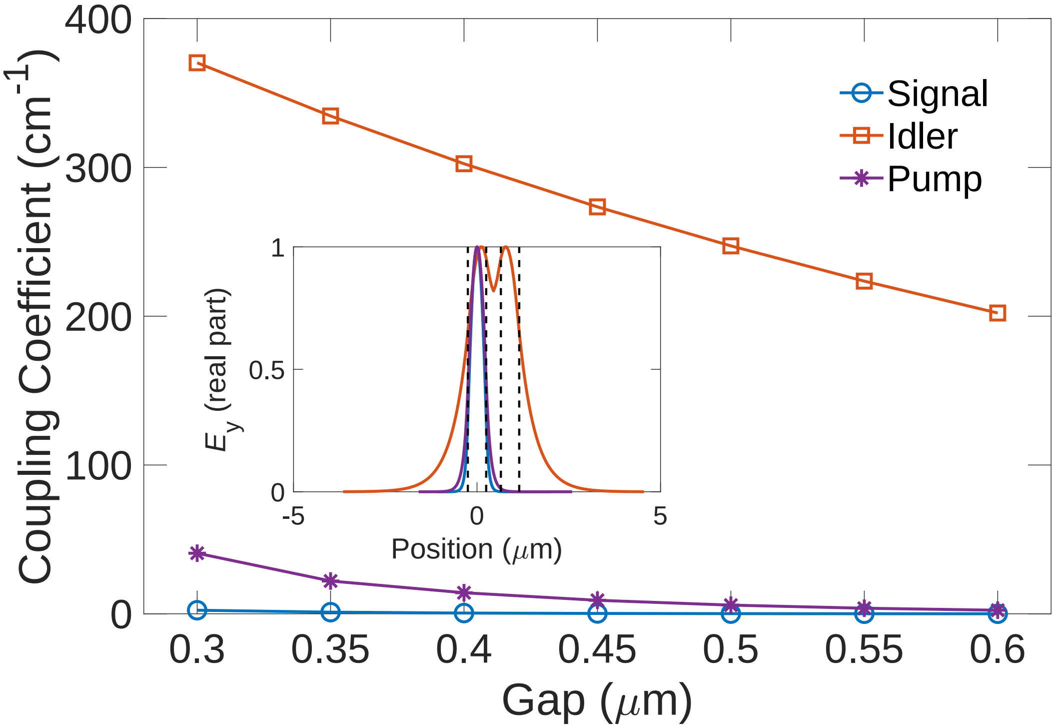

Figure 4.5: Coupling coefficients for signal (1.2 μm), idler (6 μm), and pump (2 μm) waves as a function of the gap between the two waveguides (lossless case). The inset shows the calculated field distribution after a propagation distance of 31.75 μm, when the pump, signal, idler are launched in the left waveguide under linear conditions.

We now employ full vectorial 2D-FDTD using the effective index method that is well known to be a close approximation of full-vectorial 3D-FDTD to study how the loss in the auxiliary waveguide can lead to signal amplification. In all our simulations, we used a continuous input pump and signal power densities of $\sim P_p = 22$ mW and $P_s = 0.22$ mW (corresponding to intensities I_p=0.003 GW/cm^2 and I_s=3×10^{-5} GW/cm^2). Figure 4.6 plots the nonlinear gain $G = (P_s^{\text{out}} - P_s^{\text{in}})/P_s^{\text{in}}$ as a function of the imaginary part of the effective refractive index of the doped Si in the auxiliary waveguide. In these simulations, the device length was taken to be 500 μm. The inset in Fig. 4.6 plots G as a function of L for a fixed loss factor of 0.103. These results show that G varies linearly with L when L varies from 500μm to 2 mm. Our calculations show that in our travelling (three) wave model, while the pump beam does in fact *couple* into the auxiliary waveguide it does not *interact* significantly with the other beams in this auxiliary waveguide. Note that the purpose of this guide (and any loss material) is to provide a loss mechanism for the idler wave. For the signal gain to be quadratic as calculated in [129], the length of the device needs to be in the order of several centimeters or even meters. Modeling much longer devices for each set of design parameters is very computationally expensive. In addition, there are other competing nonlinear optical processes that directly affect the gain. The previous theories dealt with second-order nonlinearity while this work deals with third-order nonlinearity hence the onset of the quadratic behavior is different for the two cases.

4.5 Discussions

The device simulations, obtained in the previous section by using rigorous full-wave simulations, indicate that realistic implementations of on-chip non-Hermitian FWM devices in silicon platforms are indeed possible. It is important however to compare the performance of the device proposed in this work with its Hermitian counterpart. As we discussed previously, one clear advantage of non-Hermitian devices is that it relaxes the stringent phase matching condition. In addition, our simulations shows that our proposed device can provide gain values up to 224% or ~5 dB after a propagation distance of only 2 mm, which is much shorter than Hermitian devices reported in literature. In particular, Mathlouthi et al. proposed a 2.5-cm-long SOI waveguide with a conversion efficiency of 5.5 dB [141], while Fukuda et

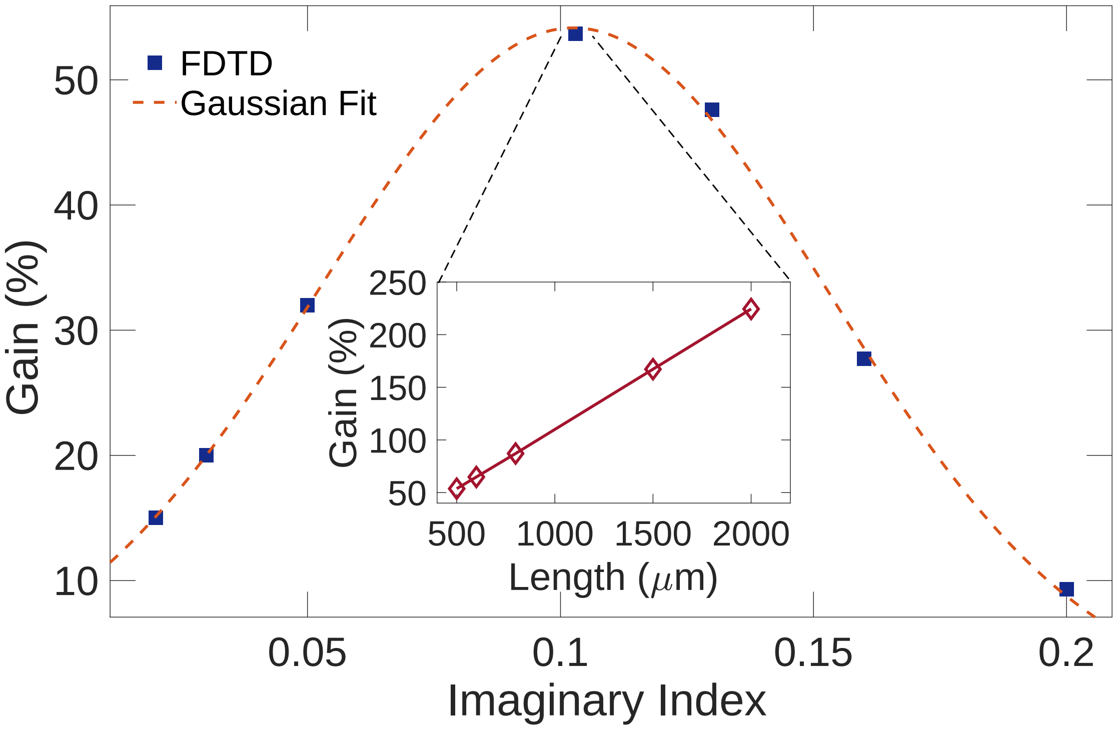

Figure 4.6: The 1.2-μm signal gain as a function of intrinsic loss in the auxiliary waveguide (actually the imaginary component of the refractive index) for a coupled-waveguide length of 500 μm. The inset shows the signal gain versus waveguide length at the optimal imaginary component of the refractive index of 0.103. The dashed line is a Gaussian fit to the calculated points as a guide to the eye.

al. achieved similar efficiency in a 1.58-cm device [118]. We note that while the aforementioned works focus on conversion efficiency rather than gain, the required length for useful signal evolution (be it conversion, generation, or gain) in a phase-matched scenario is on the order of cm, while PT symmetry can bring it down in mm scale, which is essential for integrated circuits as it implies smaller footprints of the fabricated devices. Our results thus indicated that generally comparable performance is obtained in devices with either standard phase matching and with non-Hermitian devices. Thus the realization of the non-Hermitian devices in silicon appears to be promising.

An attractive and significant feature of our proposed scheme is the large attainable bandwidth (BW). This feature is enabled particularly because of the spatial separation between the gain and loss optical components i.e., the main and auxiliary waveguides, respectively.

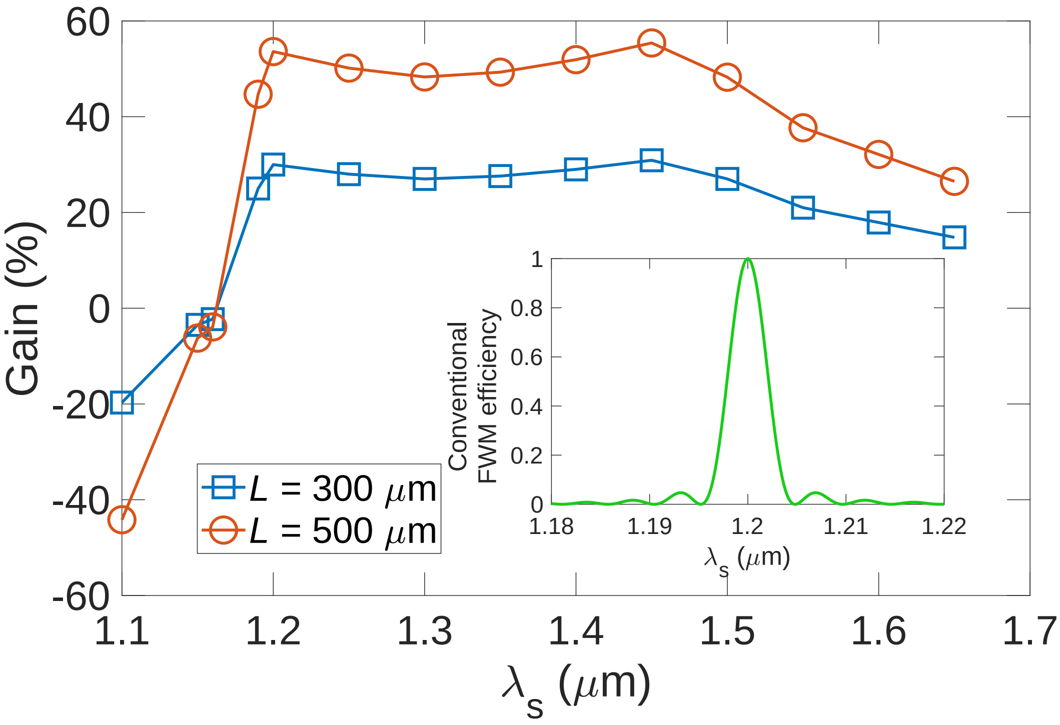

Figure 4.7: Signal gain versus signal wavelength for a 300 and 500-μm-long FWM directional-coupler amplifier at the optimally tuned imaginary component of the refractive index of 0.103. Here we obtain a full width of half maximum signal gain bandwidth of $\sim$ 450 nm. The gain decreases strongly for decreasing signal wavelengths less than 1.2 μm, while moderately decreasing for increasing wavelength larger than 1.5 μm. The lower wavelength threshold near 1.2 μm corresponds to the fact that the cutoff wavelength value of the idler in the auxiliary waveguide is 6.4 μm that corresponds to the signal wavelength of 1.185 μm. On the other hand, the higher wavelength threshold near 1.5 μm corresponds to the fact that the corresponding idler wavelength (3 μm) has decreased to the point where it is confined mostly in the main waveguide. Inset: Conversion efficiency in Hermitian FWM for a single waveguide using our waveguide parameters.

For instance, one can dope the auxiliary waveguide with a dopant material (or a mix between different materials) to provide optical losses over a large bandwidth. This will automatically lead to efficient energy conversion over a large signal bandwidth. To demonstrate this possibility, in Fig. 4.7 we plot the nonlinear gain G as a function of the signal frequency for a device length of 300 and 500 μm when loss coefficient in the auxiliary waveguide $\alpha = 0.2\ \mu\text{m}^{-1}$ is held constant at the corresponding idler frequency. We note that this is similar to presenting gain as a function of the phase mismatch ($\Delta\beta$) since

$\Delta\beta = 2\pi\left(2n_p/\lambda_p - n_s/\lambda_s - n_i/\lambda_i\right)$. Below the 1.185 μm signal wavelength (corresponding to a 6.4 μm idler cutoff wavelength), the gain decreases quickly since the longer idler wavelengths are no longer being guided inside the waveguide. On the other hand, for large signal wavelengths ($>$ 1.5 μm) the gain decreases because the idler component becomes more confined inside the main waveguide. Clearly, this strategy can enable a wide BW of operation over several hundred nanometers (450 nm in our case) as compared to only a few nm in Hermitian devices that rely on conventional phase matching in integrated silicon platforms, as shown in the inset of Fig. 4.7 where we have calculated the standard phase-matched FWM efficiency as a function of signal wavelength following the method outlined in [142], which yields a BW of ~4 nm. We note that while our gain is reduced from that seen in any lossless case, one gains by not having to deal with the significant limitations of waveguide and material dispersion.

4.6 Concluding Remarks

The concept of phase matching has been the bedrock of nonlinear optics since its formal inception in the early 1960s. In this paper, we have thus shown that the restriction imposed by phase matching in nonlinear optics can be circumvented using insights developed from principles of PT symmetry and that this process can be achieved in a realistic nanophotonic structure. This idea is based upon the incorporation of loss, which can lead to gain in a nonlinear optical system. This counter-intuitive idea reveals that in a parametric amplifier, addition of loss in the idler channel gives rise to amplification in the signal, even in the presence of a strong phase mismatch. In particular, we have demonstrated the feasibility of constructing a non-Hermitian parametric amplifier in a silicon-based materials platform consisting of a pair of quasi-PT symmetric coupled waveguides, by using rigorous full wave simulations. Our study has shown that by tuning the optical loss of the idler component, one can achieve efficient unidirectional energy conversion from the pump beam to signal component via FWM.

Furthermore our results indicate that signal gains of 5 dB for waveguide lengths of a few mm are possible over a large BW of several 100 nm, which is nearly two orders of magnitude larger BW than what is achievable in a typical phase-matched silicon-photonics FWM system. Thus we expect novel devices developed on principles of non-Hermitian nonlinear optics to have significant potential advantages over their Hermitian counterparts in terms of size, efficiency, and operational bandwidth.

Chapter 5

Dispersion Engineering in Si/Plasmonic Hybrid Waveguides

5.1 Introduction

There are increasing demands on optical interconnections to have high-bandwidth, low-latency, and low-power consumption [143]. Due to the technological advances and increased complexity in optical networks, which provide high-quality connectivity for the optical network is critical. For example, the problem of pulse broadening due to chromatic dispersion is becoming an increasingly important factor for signal degradation. This problem becomes even more serious as the data transmission scales to higher rates [144]. Many techniques have been explored to compensate for interconnect dispersion so as to achieve high-data transmission rates at long-span-length optical-network systems; these includes adding conformal dielectric overlayers to silicon waveguides [145] or using silicon strip/slot hybrid waveguide [146, 147, 148].

In this chapter, we investigate in detail the dispersion properties of a silicon/plasmonics hybrid optical interconnect structure, which also has the advantage of sending both electric and photonic signals along the same circuitry. This hybrid interconnect approach provides a natural "network-on-chip" platform, which is fully compatible with semiconductor fabrication techniques and which incorporate electric and photonic interconnects that achieve large capacity with low power losses [149, 150]. With an optimal design, this hybrid structure can provide a flat dispersion with zero dispersion not only at C-band communications wavelengths (Table 5.1), which is significant for wavelength-division-multiplexed optical network systems [151], but also for any wavelength band by changing the material and geometry of the hybrid structure.

Table 5.1: Telecom Optical Wavelength Bands

Band Name	Wavelengths	Description
O-band	1260 – 1360 nm	Original band, Passive Optical Network (PON) upstream
E-band	1360 – 1460 nm	Extended band, Water peak band
S-band	1460 – 1530 nm	Short band, PON downstream
C-band	1530 – 1565 nm	Conventional band, compatible with fiber amplifiers
L-band	1565 – 1625 nm	Long band, low attenuation
U-band	1625 – 1675 nm	Ultra-long band

5.2 Theory and Simulations

Our hybrid structure for optical interconnects consists of a high-refractive-index silicon nanowire separated from a plasmonic waveguide by a nanoscale low-refractive-index dielectric gap. At the 1.55 μm communication wavelength, a standard waveguide mode is supported in the silicon nanowire, as shown in Fig. 5.1(a), while the surface plasmon polaritons (SPP) are supported by the metal-dielectric interfaces, as indicated in Fig. 5.1(b). For a hybrid structure, the coupling between the plasmonic and waveguide modes across the gap enables a gap-mode that allows energy confinement and propagation through the low-index-gap region with a mode size that is much smaller than the diffraction limit. This gap mode shown in Fig. 5.1(c) arises from the continuity of the displacement field at the material interface, thus a strong normal electric field component occurs in the gap. The low-index gap also leads to lower long-range SPP propagation loss compared to that obtainable with higher-index materials [152]. Thus, the photonic signals propagate over large distances with low losses. Due to the hybridization mechanism, the analysis in this paper is focused upon the properties of the fundamental quasi-TM mode. Based on coupled-mode theory, the hybrid mode can be described as a superposition of the waveguide mode and the SPP mode,

$$\Psi = a\Psi_{\mathrm{Si}} + b\Psi_{\mathrm{SPP}} \tag{5.1}$$

where a and b are the amplitudes of the constituent waveguide $\Psi_{\mathrm{Si}} = \{1\ 0\}^T$ and SPP $\Psi_{\mathrm{SPP}} = \{0\ 1\}^T$ basis modes, respectively.

The modes of the coupled system are characterized by the system of equations discussed in [152, 153]

$$n_{\mathrm{Si}}a + \kappa b = n_{\mathrm{eff}}a \tag{5.2}$$

$$\kappa a + n_{\mathrm{SPP}}b = n_{\mathrm{eff}}b \tag{5.3}$$

where κ is the coupling strength between waveguide and SPP modes and n_{Si}, n_{SPP} are the effective refractive indices of the silicon and SPP waveguides, respectively. The index parameter, n_{eff}, is the eigenvalue of this hybrid system, which quantifies the phase velocity of the direction of propagation.

5.3 Results

The eigenmodes and effective indices of the hybrid nanostructure are computed using a full-vectorial finite-element mode solver (FemSim, RSoft) over a broad wavelength range. The

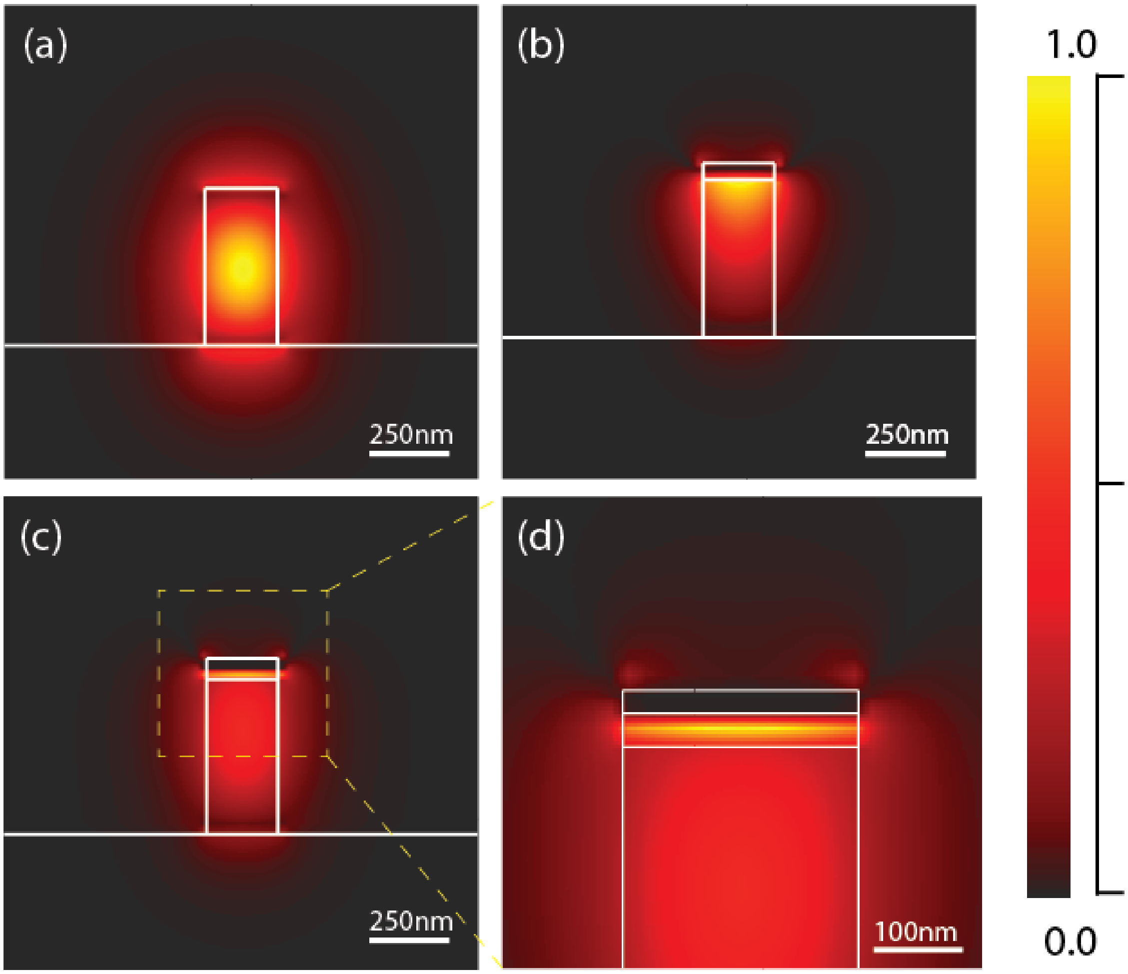

Figure 5.1: The mode profile at 1.55 μm for (a) waveguide mode silicon waveguide on SiO_2 substrate; (b) SPP mode with Au plasmonic waveguide on top of silicon waveguide; (c) hybrid gap mode with SiO_2 acting as a low dielectric spacer between plasmonic and silicon waveguides; (d) shows a zoom-in of the hybrid mode, which is confined mainly in the SiO_2 region.

dispersion properties of each material are automatically taken into considerations in our numerical simulations. The resulting raw effective-index data are fitted with a higher-order polynomial, in order to smooth out small numerical discontinuities introduced by the mode solver. The group velocity dispersion can be obtained according to [145]

$$D_\lambda = -\frac{\lambda}{c_0}\frac{d^2 n_{eff}}{d\lambda^2} \tag{5.4}$$

where n_{eff} is the effective index of the structure at free-space wavelength λ and c_0 is the speed of light.

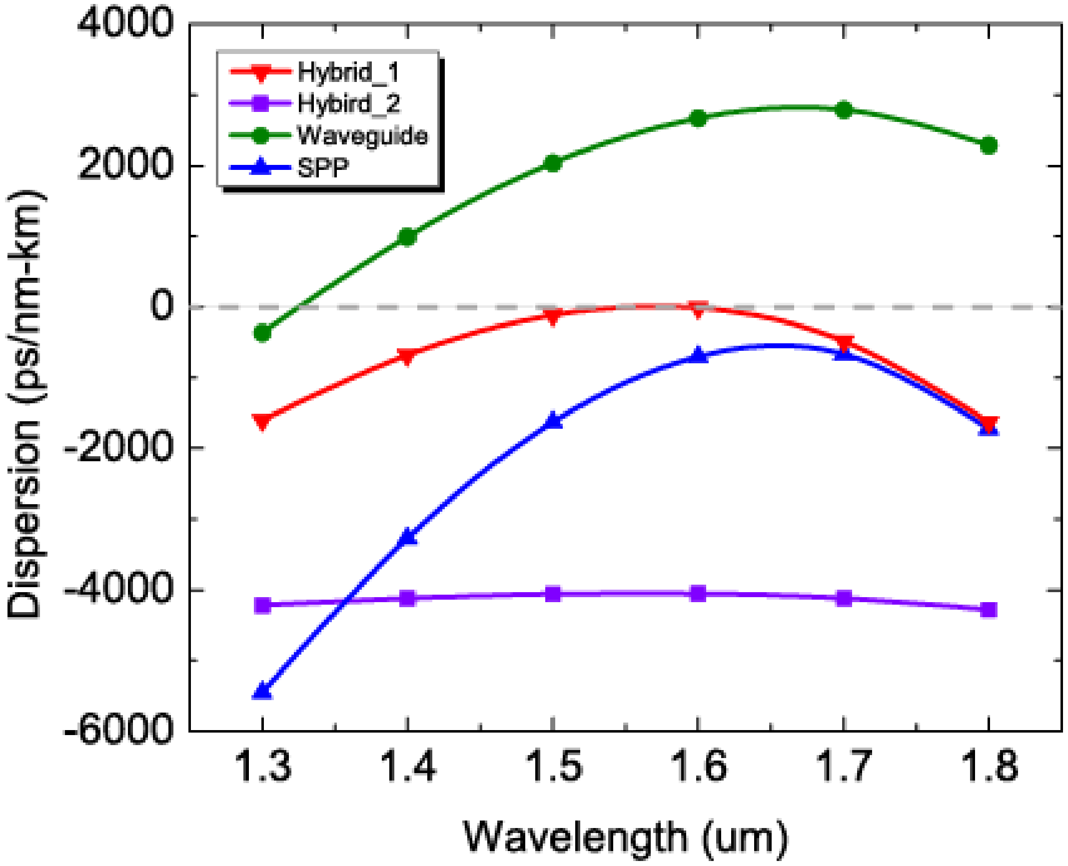

Figure 5.2: The dispersion properties for waveguide mode silicon waveguide on SiO_2 substrate (green); SPP mode with Au plasmonic waveguide on top of silicon waveguide (blue); and hybrid gap mode with SiO_2 acting as a low-dielectric spacer between the plasmonic and silicon waveguides, where we tune the dimensions so that (i) zero-dispersion is at 1.55 μm (red) and (ii) flat-dispersion across 1.3 – 1.8 μm.

Figure 5.2 plots the calculated GVD versus wavelength for different waveguides. The green (waveguide) curve shows the dispersion properties for the waveguide mode, which corresponds to a silicon waveguide placed on top of the SiO_2 substrate; the blue (SPP) curve shows the SPP-mode dispersion, in which a 40 nm-thick gold layer acting as a plasmonic waveguide is on top of the silicon waveguide, where this plasmonic waveguide can also propagate electronic signals. The calculated dispersion of the first hybrid gap mode is demonstrated using the red (Hybrid 1) curve. Our results show that with proper dispersion-engineering, and interconnect of zero dispersion is found at the communications wavelength. For this particular waveguide, we use 480 nm × 440 nm (height × width) silicon waveguide with 30-nm SiO_2 gap, which has a propagation length over 120 μm. We also demonstrated another hybrid gap mode in purple (Hybrid 2) curve, in which we have flat dispersion (i.e. 54ps/km-nm) across 1.3 – 1.8 μm. This hybrid structure has 300 nm × 220 nm (height × width) silicon waveguide with 30 nm SiO_2 gap and the propagation length is about 45 μm.

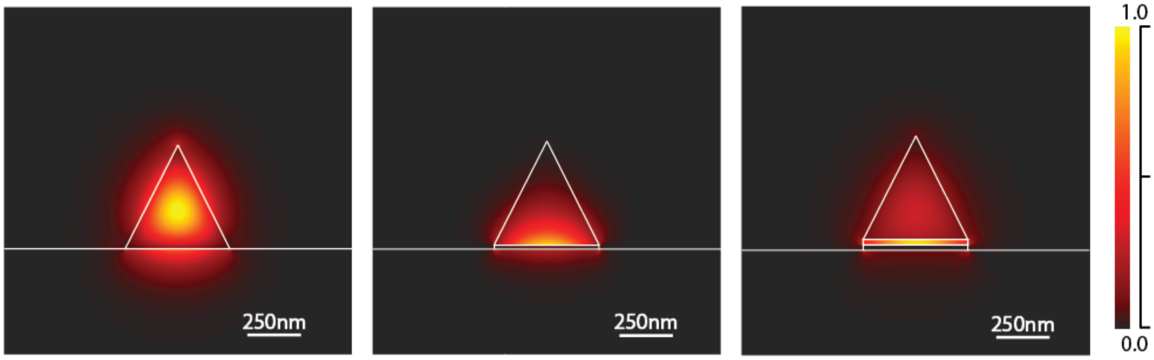

Figure 5.3: The mode profile at 1.55 μm for (a) waveguide mode triangular silicon waveguide on SiO_2 substrate; (b) SPP mode with Au plasmonic waveguide beneath triangular silicon waveguide; (c) hybrid gap mode with SiO_2 acting as a low dielectric spacer between plasmonic and triangular silicon waveguides.

Furthermore, we also investigated other geometry such as triangular silicon/plasmonics waveguide hybrid structure, which is indicated in Fig. 5.3. Fig. 5.3(a) depicts the silicon waveguide mode inside the triangular shaped structure. Fig. 5.3(b) depicts the SPP mode beneath the triangular silicon waveguide with Au as the plasmonic material. And finally, Fig. 5.3(c) depicts the hybrid gap mode with SiO_2 acting as a low dielectric spacer between the Au plasmonic and triangular silicon waveguide. As in the case of rectangular waveguides, the geometry of the hybrid structure affects the tuning of the zero-GVD point as seen in Fig. 5.4.

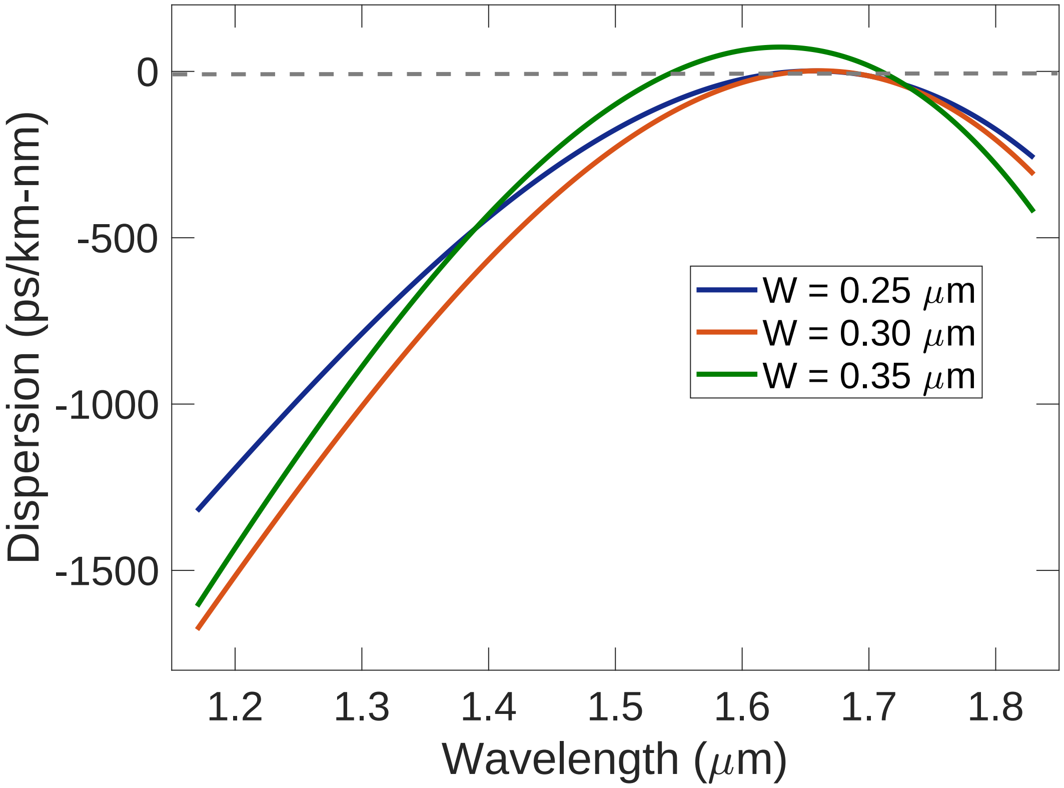

Figure 5.4: The dispersion properties for triangular hybrid waveguide mode. In all cases, the height of the triangle is 0.25 μm, the SiO_2 gap is 40 nm. The width (base) of the triangle is different in each case as follows: 0.25 μm (blue curve), 0.30 μm (red curve), 0.35 μm (green curve).

5.4 Concluding Remarks

The waveguide geometry can effectively change the dispersion properties of the hybrid mode, which can potentially tune the flat dispersion at zero dispersion rate. Such flat and low chromatic dispersion over a wide wavelength range can be crucial for enhancing nonlinear interactions of optical waves. In addition, they can be a crucial element for optical interconnects, which are arguably the most important applications for silicon photonics.

Chapter 6

Conclusion and Future Work

6.1 Conclusion

From the very early studies concerning light in Ancient Greece to the very recent researches in optics in twenty-first century, we have come a long way trying to understand vision as light radiating from our eyes, to the description of light as rays, then as particles, and then waves, and finally exhibiting both particle and wave natures. After the invention of laser several decades ago, essentially all of our long distance telecommunications are being handled by lasers coupled with optical fibers. This scheme has led to remarkable increases in information capacity and data rate. In recent years, the use of optics for shorter distances has progressively increased, even, all the way down to the electronic chips themselves or for connections on the chips. Since today's computer chips are based solely on silicon material due to its low-cost bulk manufacturing capability, conversion from electronic to photonic domain is most suitable by the utilization of this existing technology. Therefore, silicon photonics today has a vast research and development history along with many novel applications including hybrid laser technology, high-density optical interconnects, and optical integration platforms [154]. However, with a growing number of approaches available, the question remains as to in how many novel applications we can exploit silicon photonics as an obvious solution and how it can easily be integrated with an electronic chip. This dissertation answers these questions by describing three such applications for optical communications using silicon nanophotonics.

In **Chapter 2** we summarize the fundamental theory and concept of differential phase shift keying, coherent perfect absorption, four wave mixing, and dispersion that are essential to this thesis work. We also provide a concise description of various simulation tools. They are 1) finite element method, used to compute modes and their effective indices inside optical waveguides, 2) finite difference time domain, used to perform calculations regarding propagation of electromagnetic waves inside optical media, and 3) effective index method, used to approximate a computationally exhaustive three dimensional simulation into a faster two dimensional analysis. Finally, processing steps for fabrication of silicon photonic circuits, as performed at Brookhaven National Laboratories, have been detailed.

Differential phase shift keying is an increasingly important optical modulation format for long-haul fiber communications and short-haul on-chip communications. **Chapter 3** of this thesis deals with such a DPSK demodulator circuit. At the heart of the circuit is a ring resonator. We have thoroughly designed such circuit, simulated it extensively and demonstrated that using the phenomenon known as coherent perfect absorption we can indeed demodulate a DPSK encoded signal at a data rate of 10 Gbps. This photonic circuit has several advantages including small device footprint, existing fabrication technology compatibility, tunable wavelength through temperature sensitivity, control of loss through carrier injection, and being an active component of all-optical logic devices.

Nonlinear optics is an important part of optical science, especially silicon photonics due to the presence of third-order nonlinear susceptibility of silicon. Four wave mixing is a significant process that occur inside silicon waveguides. While this process is imperative to obtain gain for a signal component at a particular wavelength, there exists a phase-matching condition between the different propagation constants that must be satisfied. This condition, in turn, limits the number of wavelengths that can be amplified through such FWM process that depends on the specific waveguide geometry and familiar. In **Chapter 4** of this dissertation we have shown that this stringent requirement can be eased if we exploit what is known as non-Harmitian phase-matching and $\mathcal{PT}$ symmetry. It implies that a loss component is added for the idler component through a coupled-waveguide structure and as the three waves (pump, signal, and idler) propagate inside the main waveguide, the signal achieves gain at the expense of decreasing idler. We have meticulously investigated FWM dynamics of both a stand-alone waveguide and a coupled-waveguide. After exploring the dynamics on a free-space optics using analytical method, namely, Runge-Kutta method, we have designed a coupled-waveguide geometry and simulated it using FDTD method in a realistic material system, namely, silicon photonics. Through our study we have found that by tuning the optical loss of the idler component, one can achieve efficient unidirectional energy conversion from the pump beam to signal component via FWM. Furthermore our results indicate that signal gains of 5 dB for waveguide lengths of a few mm are possible over a large bandwidth of several 100 nm, which is nearly two orders of magnitude larger than what is achievable in a typical phase-matched silicon-photonics FWM system.

Dispersion is a very well-known and thoroughly studied phenomenon that causes the problem of pulse broadening through signal degradation. While there have been many propositions to offset the effect of dispersion through innovative structures and material, using silicon waveguides is the most straight-forward and cost effective method. In **Chapter 5**, we propose a silicon-plasmonic hybrid optical waveguide that has the ability to suppress group velocity dispersion at a wavelength of choice from the communication C-band by changing the waveguide geometry. The silicon waveguide is separated from a plasmonic waveguide through a low-index gap of silica. The electric field is confined inside this low-index region. Through the various dimensions of this hybrid structure we have shown that the zero-GVD point can be tuned in a broad wavelength range from $1.2 - 1.9\ \mu$m.

6.2 Future Work

We have demonstrated DPSK demodulation using CPA in a microring resonator for a data rate of 10 Gbps. For higher bit rates the device can be further made smaller in size since higher the bit rate, shorter the path difference. For example, we can easily make the device to work at a data rate of 20 Gbps by halving the path difference between the two input waveguides. This would not only be beneficial to work at higher data rates, but also make the footprint of the device considerably smaller. Another important application of this demodulation scheme would be to extend it to other formats of integrated demodulators, e.g., differential quadrature phase shift keying (DQPSK) and 8-ary PSK. In addition, while this application is illuminative, the use of CPA for DPSK demodulation is not limited to the specific resonator geometry used here. Indeed, CPA is generalizable to any resonant cavity and has been explored for Fabry-Perot cavities [81], photonic crystal cavities [82], and plasmonic structures [155]. Therefore, the advantages and tradeoffs of different cavity designs in terms of device footprint, efficiency, and OSNR as compared to other DPSK demodulation techniques requires further exploration.

We have comprehensively investigated the gain of signal via FWM using non-Hermitian phase matching technique in a coupled-waveguide system made of a realistic material (silicon). While this scheme shows the effectiveness of loss as a way to achieve gain, there are several other waveguide geometries that need to be investigated, for example, Bragg grating. After ascertaining the existence of a sufficient level of gain, one can further look into other important parameters like efficiency. Also, since this non-Hermitian parametric process occurs for second-order optical parametric amplification and third-order four wave mixing, it is inferable that other important nonlinear phenomena like second harmonic generation, third harmonic generation, self and cross phase modulation, Raman amplification can be investigated under similar formulism. In addition, the first ever experimental demonstration of such a system is yet to be executed.

Lastly, we have analyzed the effect of waveguide geometry for a Si/plasmonics hybrid optical interconnect structure on its zero group velocity dispersion points. Further analysis is possible in terms of the effect of different plasmonic materials and low-index gap materials. In addition, similar dispersion analysis can be performed by changing the material platform for mid and far-infrared region of electromagnetic spectrum that has a considerable amount of sensing applications.

Bibliography

[1] T. Baehr-Jones, T. Pinguet, P. L. Guo-Qiang, S. Danziger, D. Prather, and M. Hochberg, “Myths and rumours of silicon photonics,” *Nature Photonics*, vol. 6, no. 4, pp. 206–208, Apr. 2012.

[2] R. Soref, “The past, present, and future of silicon photonics,” *IEEE Journal of Selected Topics in Quantum Electronics*, vol. 12, no. 6, pp. 1678–1687, Nov. 2006.

[3] A. Rickman, “The commercialization of silicon photonics,” *Nature Photonics*, vol. 8, no. 8, pp. 579–582, aug 2014.

[4] H. D. Thacker, R. Shafiiha, J. Lexau, X. Zheng, S. S. Djordjevic, S. Lin, J. Simons, A. Abed, P. Amberg, E. Chang, I. Shubin, J.-H. Lee, Y. Luo, J. Yao, F. Liu, H. Liang, D. Feng, M. Asghari, R. Ho, K. Raj, A. V. Krishnamoorthy, and J. E. Cunningham, “Hybrid integration and packaging of an energy-efficient WDM silicon photonic chip-to-chip interconnect,” in *2015 IEEE 65th Electronic Components and Technology Conference (ECTC)*. IEEE, May 2015.

[5] B. Kuyken, X. Liu, R. M. Osgood, R. Baets, G. Roelkens, and W. M. J. Green, “Mid-infrared to telecom-band supercontinuum generation in highly nonlinear silicon-on-insulator wire waveguides,” *Optics Express*, vol. 19, no. 21, p. 20172, Sep. 2011.

[6] F. F. Yassa, J. R. Jasica, R. I. Hartley, and S. E. Noujaim, “A silicon compiler for digital signal processing: Methodology, implementation, and applications,” *Proceedings of the IEEE*, vol. 75, no. 9, pp. 1272–1282, 1987.

[7] A. Biberman, K. Preston, G. Hendry, N. Sherwood-Droz, J. Chan, J. S. Levy, M. Lipson, and K. Bergman, “Photonic network-on-chip architectures using multilayer deposited silicon materials for high-performance chip multiprocessors,” *ACM Journal on Emerging Technologies in Computing Systems*, vol. 7, no. 2, pp. 1–25, Jun. 2011.

[8] F. Schuster, D. Coquillat, H. Videlier, M. Sakowicz, F. Teppe, L. Dussopt, B. Giffard, T. Skotnicki, and W. Knap, “Broadband terahertz imaging with highly sensitive silicon CMOS detectors,” *Optics Express*, vol. 19, no. 8, p. 7827, Apr. 2011.

[9] A. Márquez, F. J. Martínez, S. Gallego, M. Ortuño, J. Francés, A. Beléndez, and I. Pascual, “Averaged stokes polarimetry applied to characterize parallel-aligned liquid crystal on silicon displays,” in *Optics and Photonics for Information Processing VIII*, A. A. S. Awwal, K. M. Iftekharuddin, M. A. Matin, and A. Márquez, Eds. SPIE, sep 2014.

[10] M. H. Khan, H. Shen, Y. Xuan, L. Zhao, S. Xiao, D. E. Leaird, A. M. Weiner, and M. Qi, “Ultrabroad-bandwidth arbitrary radiofrequency waveform generation with a silicon photonic chip-based spectral shaper,” *Nature Photonics*, vol. 4, no. 2, pp. 117–122, jan 2010.

[11] K. I. Chen, B. R. Li, and Y. T. Chen, “Silicon nanowire field-effect transistor-based biosensors for biomedical diagnosis and cellular recording investigation,” *Nano Today*, vol. 6, no. 2, pp. 131–154, Apr. 2011.

[12] A. V. Velasco, P. Cheben, P. J. Bock, A. Delâge, J. H. Schmid, J. Lapointe, S. Janz, M. L. Calvo, D.-X. Xu, M. Florjańczyk, and M. Vachon, “High-resolution fourier-transform spectrometer chip with microphotonic silicon spiral waveguides,” *Optics Letters*, vol. 38, no. 5, p. 706, feb 2013.

[13] F. Costantini, A. Nascetti, R. Scipinotti, F. Domenici, S. Sennato, L. Gazza, F. Bordi, N. Pogna, C. Manetti, D. Caputo, and G. de Cesare, “On-chip detection of multiple

serum antibodies against epitopes of celiac disease by an array of amorphous silicon sensors," *RSC Adv.*, vol. 4, no. 4, pp. 2073–2080, 2014.

[14] M. E. Zaghloul, J. L. Meador, and R. W. Newcomb, Eds., *Silicon Implementation of Pulse Coded Neural Networks*. Springer Science & Business Media, 2012.

[15] M. Green, J. Zhao, A. Wang, and S. Wenham, "Progress and outlook for high-efficiency crystalline silicon solar cells," *Solar Energy Materials and Solar Cells*, vol. 65, no. 1-4, pp. 9–16, jan 2001.

[16] Y. Fu, X. Hu, and Q. Gong, "Silicon photonic crystal all-optical logic gates," *Physics Letters A*, vol. 377, no. 3-4, pp. 329–333, Jan. 2013.

[17] L. Vivien and L. Pavesi, Eds., *Handbook of Silicon Photonics*. CRC Press, 2013.

[18] W. N. Ye and Y. Xiong, "Review of silicon photonics: history and recent advances," *Journal of Modern Optics*, vol. 60, no. 16, pp. 1299–1320, sep 2013.

[19] H. Park, A. W. Fang, S. Kodama, and J. E. Bowers, "Hybrid silicon evanescent laser fabricated with a silicon waveguide and III-v offset quantum wells," *Optics Express*, vol. 13, no. 23, p. 9460, 2005.

[20] J. Liu, X. Sun, D. Pan, X. Wang, L. C. Kimerling, T. L. Koch, and J. Michel, "Tensile-strained, n-type ge as a gain medium for monolithic laser integration on si," *Optics Express*, vol. 15, no. 18, p. 11272, 2007.

[21] O. Boyraz and B. Jalali, "Demonstration of a silicon raman laser," *Optics Express*, vol. 12, no. 21, p. 5269, 2004.

[22] H. Park, A. W. Fang, R. Jones, O. Cohen, O. Raday, M. N. Sysak, M. J. Paniccia, and J. E. Bowers, "A hybrid AlGaInAs-silicon evanescent waveguide photodetector," *Optics Express*, vol. 15, no. 10, p. 6044, 2007.

[23] P. R. A. Binetti, X. J. M. Leijtens, T. de Vries, Y. S. Oei, L. D. Cioccio, J.-M. Fedeli, C. Lagahe, J. V. Campenhout, D. V. Thourhout, P. J. van Veldhoven, R. Ntzel, and M. K. Smit, "InP/InGaAs photodetector on SOI photonic circuitry," *IEEE Photonics Journal*, vol. 2, no. 3, pp. 299–305, jun 2010.

[24] J. Osmond, L. Vivien, J.-M. Fédéli, D. Marris-Morini, P. Crozat, J.-F. Damlencourt, E. Cassan, and Y. Lecunff, "40 gb/s surface-illuminated ge-on-si photodetectors," *Applied Physics Letters*, vol. 95, no. 15, p. 151116, oct 2009.

[25] L. Vivien, A. Polzer, D. Marris-Morini, J. Osmond, J. M. Hartmann, P. Crozat, E. Cassan, C. Kopp, H. Zimmermann, and J. M. Fédéli, "Zero-bias 40gbit/s germanium waveguide photodetector on silicon," *Optics Express*, vol. 20, no. 2, p. 1096, jan 2012.

[26] X. Sun, J. Liu, L. C. Kimerling, and J. Michel, "Room-temperature direct bandgap electroluminesence from ge-on-si light-emitting diodes," *Optics Letters*, vol. 34, no. 8, p. 1198, apr 2009.

[27] R. R. Grote, K. Padmaraju, B. Souhan, J. B. Driscoll, K. Bergman, and R. M. Osgood, "10 gb/s error-free operation of all-silicon ion-implanted-waveguide photodiodes at 1.55 μm," *IEEE Photonics Technology Letters*, vol. 25, no. 1, pp. 67–70, jan 2013.

[28] B. Souhan, C. P. Chen, R. R. Grote, J. B. Driscoll, N. Ophir, K. Bergman, and R. M. Osgood, "Error-free operation of an all-silicon waveguide photodiode at 1.9 μm," *IEEE Photonics Technology Letters*, vol. 25, no. 21, pp. 2031–2034, nov 2013.

[29] R. M. Osgood, N. C. Panoiu, J. I. Dadap, X. Liu, X. Chen, I.-W. Hsieh, E. Dulkeith, W. M. Green, and Y. A. Vlasov, "Engineering nonlinearities in nanoscale optical systems: physics and applications in dispersion-engineered silicon nanophotonic wires," *Advances in Optics and Photonics*, vol. 1, no. 1, p. 162, Jan. 2009.

[30] R. W. Boyd, *Nonlinear Optics*. Elsevier LTD, Oxford, 2008.

[31] B. Chmielak, M. Waldow, C. Matheisen, C. Ripperda, J. Bolten, T. Wahlbrink, M. Nagel, F. Merget, and H. Kurz, "Pockels effect based fully integrated, strained silicon electro-optic modulator," *Optics Express*, vol. 19, no. 18, p. 17212, aug 2011.

[32] R. Soref and B. Bennett, "Electrooptical effects in silicon," *IEEE Journal of Quantum Electronics*, vol. 23, no. 1, pp. 123–129, jan 1987.

[33] S. E. Miller, "Integrated optics: An introduction," *Bell System Technical Journal*, vol. 48, no. 7, pp. 2059–2069, sep 1969.

[34] G. T. Reed, W. R. Headley, and C. E. J. Png, "Silicon photonics: the early years," in *Optoelectronic Integration on Silicon II*, J. A. Kubby and G. E. Jabbour, Eds. SPIE, mar 2005.

[35] H. Z. Massoud, Ed., *Ultra Large Scale Integration Science & Technology: 6th International Symposium (Proceedings / Electrochemical Society)*. Electrochemical Society, 1997.

[36] F. Namavar, E. Cortesi, and P. Sioshansi, "Low-defect, high-quality simox produced by multiple oxygen implantation with substoichiometric total dose," *MRS Proceedings*, vol. 128, jan 1988.

[37] M. Bruel, "Silicon on insulator material technology," *Electronics Letters*, vol. 31, no. 14, p. 1201, 1995.

[38] E. Cortesi, F. Namavar, and R. A. Soref, in *IEEE SOS/SOI Technology Conference*, Stateline, NV, Oct. 1989.

[39] R. Soref, "Silicon-based optoelectronics," *Proceedings of the IEEE*, vol. 81, no. 12, pp. 1687–1706, 1993.

[40] R. Soref and J. Larenzo, "All-silicon active and passive guided-wave components for

λ = 1.3 and 1.6 μm," *IEEE Journal of Quantum Electronics*, vol. 22, no. 6, pp. 873–879, Jun. 1986.

[41] J. S. Foresi, M. R. Black, A. M. Agarwal, and L. C. Kimerling, "Losses in polycrystalline silicon waveguides," *Applied Physics Letters*, vol. 68, no. 15, pp. 2052–2054, Apr. 1996.

[42] X. Wang, "Silicon photonic waveguide bragg gratings," pp. –, 2013.

[43] L. Vivien, S. Laval, B. Dumont, S. Lardenois, A. Koster, and E. Cassan, "Polarization-independent single-mode rib waveguides on silicon-on-insulator for telecommunication wavelengths," *Optics Communications*, vol. 210, no. 1-2, pp. 43–49, sep 2002.

[44] W. Ye, D.-X. Xu, S. Janz, P. Cheben, M.-J. Picard, B. Lamontagne, and N. Tarr, "Birefringence control using stress engineering in silicon-on-insulator (SOI) waveguides," *Journal of Lightwave Technology*, vol. 23, no. 3, pp. 1308–1318, Mar. 2005.

[45] J. H. Schmid, M. Ibrahim, P. Cheben, J. Lapointe, S. Janz, P. J. Bock, A. Densmore, B. Lamontagne, R. Ma, W. N. Ye, and D.-X. Xu, "Temperature-independent silicon subwavelength grating waveguides," *Optics Letters*, vol. 36, no. 11, p. 2110, May 2011.

[46] J. Heebner, R. Grover, and T. Ibrahim, *Optical Microresonators: Theory, Fabrication, and Applications*. SPRINGER VERLAG GMBH, 2007.

[47] L. Rayleigh, "The problem of the whispering gallery," *Philosophical Magazine*, pp. 1001–1004, 1910.

[48] E. A. J. Marcatili, "Bends in optical dielectric guides," *Bell System Technical Journal*, vol. 48, no. 7, pp. 2103–2132, Sep. 1969.

[49] H. P. Weber and R. Ulrich, "A thin-film ring laser," *Applied Physics Letters*, vol. 19, no. 2, pp. 38–40, Jul. 1971.

[50] D. Chu, M. Chin, N. Sauer, Z. Xu, T. Chang, and S. Ho, "1.5 μm InGaAs/InAlGaAs quantum-well microdisk lasers," *IEEE Photonics Technology Letters*, vol. 5, no. 12, pp. 1353–1355, Dec. 1993.

[51] C. R. Abernathy, S. J. Pearton, J. D. MacKenzie, J. R. Mileham, S. R. Bharatan, V. Krishnamoorthy, K. S. Jones, M. Hagerott-Crawford, R. J. Shul, S. P. Kilcoyne, J. M. Zavada, D. Zhang, and R. M. Kolbas, "Growth and fabrication of gan-ingan microdisk laser structures," *Solid-State Electronics*, vol. 39, pp. 311–313, 1996.

[52] Q. Xu and M. Lipson, "All-optical logic based on silicon micro-ring resonators," *Optics Express*, vol. 15, no. 3, p. 924, 2007.

[53] J. M. Rothenberg, C. P. Chen, J. J. Ackert, J. I. Dadap, A. P. Knights, K. Bergman, R. M. Osgood, and R. R. Grote, "Experimental demonstration of coherent perfect absorption in a silicon photonic racetrack resonator," *Optics Letters*, vol. 41, no. 11, p. 2537, May 2016.

[54] K. D. Vos, J. Girones, S. Popelka, E. Schacht, R. Baets, and P. Bienstman, "SOI optical microring resonator with poly(ethylene glycol) polymer brush for label-free biosensor applications," *Biosensors and Bioelectronics*, vol. 24, no. 8, pp. 2528–2533, apr 2009.

[55] P. J. Pauzauskie, D. J. Sirbuly, and P. Yang, "Semiconductor nanowire ring resonator laser," *Physical Review Letters*, vol. 96, no. 14, Apr. 2006.

[56] I. Matsushima, H. Yashiro, and T. Tomie, "10 kHz 40 w ti:sapphire regenerative ring amplifier," *Optics Letters*, vol. 31, no. 13, p. 2066, jul 2006.

[57] I. Wolff, "Microstrip bandpass filter using degenerate modes of a microstrip ring resonator," *Electronics Letters*, vol. 8, no. 12, p. 302, 1972.

[58] Z. Qiang, W. Zhou, and R. A. Soref, "Optical add-drop filters based on photonic crystal ring resonators," *Optics Express*, vol. 15, no. 4, p. 1823, Feb. 2007.

[59] A. H. J. Yang and D. Erickson, “Optofluidic ring resonator switch for optical particle transport,” *Lab on a Chip*, vol. 10, no. 6, p. 769, 2010.

[60] N. Sherwood-Droz, H. Wang, L. Chen, B. G. Lee, A. Biberman, K. Bergman, and M. Lipson, “Optical 4x4 hitless slicon router for optical networks-on-chip (NoC),” *Optics Express*, vol. 16, no. 20, p. 15915, Sep. 2008.

[61] M. L. Clifford Pollock, *Integrated Photonics*. SPRINGER VERLAG GMBH, 2003.

[62] E. A. J. Marcatili, “Dielectric rectangular waveguide and directional coupler for integrated optics,” *Bell System Technical Journal*, vol. 48, no. 7, pp. 2071–2102, Sep. 1969.

[63] H. Kogelnik, “Switched directional couplers with alternating $\delta\beta$,” *IEEE Journal of Quantum Electronics*, vol. 12, no. 7, pp. 396–401, Jul. 1976.

[64] Z. Lu, H. Yun, Y. Wang, Z. Chen, F. Zhang, N. A. F. Jaeger, and L. Chrostowski, “Broadband silicon photonic directional coupler using asymmetric-waveguide based phase control,” *Optics Express*, vol. 23, no. 3, p. 3795, feb 2015.

[65] D. Thomson, A. Zilkie, J. E. Bowers, T. Komljenovic, G. T. Reed, L. Vivien, D. Marris-Morini, E. Cassan, L. Virot, J.-M. Fédéli, J.-M. Hartmann, J. H. Schmid, D.-X. Xu, F. Boeuf, P. O’Brien, G. Z. Mashanovich, and M. Nedeljkovic, “Roadmap on silicon photonics,” *Journal of Optics*, vol. 18, no. 7, p. 073003, Jun. 2016.

[66] D. Liang and J. E. Bowers, “Recent progress in lasers on silicon,” *Nature Photonics*, vol. 4, no. 8, pp. 511–517, Jul. 2010.

[67] M. Liu, X. Yin, E. Ulin-Avila, B. Geng, T. Zentgraf, L. Ju, F. Wang, and X. Zhang, “A graphene-based broadband optical modulator,” *Nature*, vol. 474, no. 7349, pp. 64–67, May 2011.

[68] C. Koos, W. Freude, T. J. Kippenberg, J. Leuthold, L. R. Dalton, J. Pfeifle, C. Weimann, M. Lauermann, R. Palmer, S. Koeber, S. Wolf, P. Schindler, V. Brasch, and D. Elder, "Terabit/s optical transmission using chip-scale frequency comb sources," in *2014 The European Conference on Optical Communication (ECOC)*. IEEE, Sep. 2014.

[69] Y. Tang, J. D. Peters, and J. E. Bowers, "Over 67 GHz bandwidth hybrid silicon electroabsorption modulator with asymmetric segmented electrode for 13 μm transmission," *Optics Express*, vol. 20, no. 10, p. 11529, May 2012.

[70] C. Haffner, W. Heni, Y. Fedoryshyn, J. Niegemann, A. Melikyan, D. L. Elder, B. Baeuerle, Y. Salamin, A. Josten, U. Koch, C. Hoessbacher, F. Ducry, L. Juchli, A. Emboras, D. Hillerkuss, M. Kohl, L. R. Dalton, C. Hafner, and J. Leuthold, "All-plasmonic mach–zehnder modulator enabling optical high-speed communication at the microscale," *Nature Photonics*, vol. 9, no. 8, pp. 525–528, Jul. 2015.

[71] D. J. Thomson, F. Y. Gardes, Y. Hu, G. Mashanovich, M. Fournier, P. Grosse, J.-M. Fedeli, and G. T. Reed, "High contrast 40gbit/s optical modulation in silicon," *Optics Express*, vol. 19, no. 12, p. 11507, May 2011.

[72] T. Yin, R. Cohen, M. M. Morse, G. Sarid, Y. Chetrit, D. Rubin, and M. J. Paniccia, "31 GHz ge n-i-p waveguide photodetectors on silicon-on-insulator substrate," *Optics Express*, vol. 15, no. 21, p. 13965, 2007.

[73] B. Souhan, R. R. Grote, C. P. Chen, H.-C. Huang, J. B. Driscoll, M. Lu, A. Stein, H. Bakhru, K. Bergman, W. M. J. Green, and R. M. Osgood, "Si^+-implanted si-wire waveguide photodetectors for the mid-infrared," *Optics Express*, vol. 22, no. 22, p. 27415, Oct. 2014.

[74] L. Tsybeskov, D. Lockwood, and M. Ichikawa, "Silicon photonics: CMOS going

optical [scanning the issue]," *Proceedings of the IEEE*, vol. 97, no. 7, pp. 1161–1165, jul 2009.

[75] A. E.-J. Lim, J. Song, Q. Fang, C. Li, X. Tu, N. Duan, K. K. Chen, R. P.-C. Tern, and T.-Y. Liow, "Review of silicon photonics foundry efforts," *IEEE Journal of Selected Topics in Quantum Electronics*, vol. 20, no. 4, pp. 405–416, Jul. 2014.

[76] M. Hochberg, N. C. Harris, R. Ding, Y. Zhang, A. Novack, Z. Xuan, and T. Baehr-Jones, "Silicon photonics: The next fabless semiconductor industry," *IEEE Solid-State Circuits Magazine*, vol. 5, no. 1, pp. 48–58, 2013.

[77] [Online]. Available: http://phoenixbv.com/news.php

[78] B. P. Lathi and Z. Ding, *Modern Digital and Analog Communication Systems*. Oxford University Press, 2008.

[79] S. Ferber, R. Ludwig, C. Boerner, A. Wietfeld, B. Schmauss, J. Berger, C. Schubert, G. Unterboersch, and H. Weber, "Comparison of DPSK and OOK modulation format in 160 gbps transmission system," *Electronics Letters*, vol. 39, no. 20, p. 1458, 2003.

[80] A. H. Gnauck and P. J. Winzer, "Optical phase-shift-keyed transmission," *J. Lightwave Technol.*, vol. 23, no. 1, p. 115, Jan 2005. [Online]. Available: http://jlt.osa.org/abstract.cfm?URI=jlt-23-1-115

[81] W. Wan, Y. Chong, L. Ge, H. Noh, A. D. Stone, and H. Cao, "Time-reversed lasing and interferometric control of absorption," *Science*, vol. 331, no. 6019, pp. 889–892, Feb. 2011.

[82] R. R. Grote, J. B. Driscoll, and R. M. Osgood, "Integrated optical modulators and switches using coherent perfect loss," *Optics Letters*, vol. 38, no. 16, p. 3001, Aug. 2013.

[83] H. A. Haus, *Waves and Fields in Optoelectronics (Prentice-Hall series in solid state physical electronics)*. Prentice Hall, 1983.

[84] A. Yariv and P. Yeh, *Photonics: Optical Electronics in Modern Communications (The Oxford Series in Electrical and Computer Engineering)*. Oxford University Press, 2006.

[85] M. C. T. Bahaa E.A. Saleh, *Fundamentals of Photonics*. Wiley John and Sons, 2001.

[86] M. S. Wartak, *Computational Photonics: An Introduction with MATLAB*. CAMBRIDGE UNIV PR, 2013.

[87] J.-M. Jin, *Theory and Computation of Electromagnetic Fields*. Wiley-IEEE Press, 2010.

[88] J. M. Jin, *The Finite Element Method in Electromagnetics*. JOHN WILEY & SONS INC, 2014.

[89] S. M. Rao, Ed., *Time Domain Electromagnetics*. Elsevier Science, 1999.

[90] K. Yee, “Numerical solution of initial boundary value problems involving maxwell's equations in isotropic media,” *IEEE Transactions on Antennas and Propagation*, vol. 14, no. 3, pp. 302–307, may 1966.

[91] G. B. Hocker and W. K. Burns, “Mode dispersion in diffused channel waveguides by the effective index method,” *Applied Optics*, vol. 16, no. 1, p. 113, Jan. 1977.

[92] “At the heart of electronics.” [Online]. Available: https://www.soitec.com/en

[93] “Hmds prime ovens.” [Online]. Available: http://www.yieldengineering.com/products/hmds-prime-ovens

[94] “Dow corning xr 1541 e-beam resist.” [Online]. Available: http://www.dowcorning.com/content/publishedlit/11-1547e-01.pdf

[95] B. Souhan, “Defect mediated sub-bandgap optical absorption in ion-implanted silicon nano-wire waveguide photodetectors,” pp. –, 2015.

[96] J. Driscoll, “Silicon photonics: All-optical devices for linear and nonlinear applications,” pp. –, 2014.

[97] “Jeol usa jbx-6300fs electron beam lithography system.” [Online]. Available: http://www.jeolusa.com/PRODUCTS/SemiconductorEquipment/ElectronBeamLithography/JBX6300FS/tabid/244/Default.aspx

[98] “Rsoft.” [Online]. Available: https://www.synopsys.com/optical-solutions/rsoft.html

[99] “Beamer.” [Online]. Available: https://genisys-gmbh.com/web/products/beamer.html

[100] “Oxford plasmalab.” [Online]. Available: https://www.oxford-instruments.com/

[101] “Trion pecvd.” [Online]. Available: http://triontech.com/deposition-products/orion-pecvd/

[102] G. Contestabile, P. Velha, and N. Andriolli, “High-speed InP-integrated pre-amplified demodulator for WDM-DPSK signals,” *IEEE Photonics Technology Letters*, vol. 27, no. 24, pp. 2547–2550, Dec. 2015.

[103] L. Zheng, J. Du, K. Xu, X. Wu, H. K. Tsang, and Z. He, “High speed DPSK modulation up to 30 gbps for short reach optical communications using a silicon microring modulator,” in *2017 16th International Conference on Optical Communications and Networks (ICOCN)*. IEEE, Aug. 2017.

[104] J. Ge, H. Feng, and M. P. Fok, “High-speed wavelength tunable DPSK demodulation using a phase modulator based loop mirror filter,” *Optics Letters*, vol. 39, no. 12, p. 3500, Jun. 2014.

[105] K. Vyrsokinos, C. Vagionas, C. Mitsolidou, M. Cherchi, M. Harjanne, S. Ylinen, M. Kapulainen, T. Aalto, and A. Miliou, “Dpsk-demodulation based on ultra-compact

micron-scale soi platform," in *2015 Optical Fiber Communications Conference and Exhibition (OFC)*, Mar. 2015, pp. 1–3.

[106] P. Velha, N. Andriolli, and G. Contestabile, "Preamplified demodulation of 56-gb/s WDM-DPSK signals by an AWG-based InP PIC," *IEEE Photonics Journal*, vol. 8, no. 2, pp. 1–8, Apr. 2016.

[107] J. I. Dadap, N. C. Panoiu, X. Chen, I.-W. Hsieh, X. Liu, C.-Y. Chou, E. Dulkeith, S. J. McNab, F. Xia, W. M. J. Green, L. Sekaric, Y. A. Vlasov, and R. M. Osgood, "Nonlinear-optical phase control in dispersion-engineered si photonic wires," *Optics Express*, vol. 16, no. 2, p. 1280, 2008.

[108] A. Shacham, K. Bergman, and L. P. Carloni, "On the design of a photonic network-on-chip," in *First International Symposium on Networks-on-Chip (NOCS'07)*. IEEE, May 2007.

[109] J. E. Bowers and A. Y. Liu, "A comparison of four approaches to photonic integration," in *2017 Optical Fiber Communications Conference and Exhibition (OFC)*, Los Angeles, CA, 2017.

[110] C. A. Barrios and M. Lipson, "Modeling and analysis of high-speed electro-optic modulation in high confinement silicon waveguides using metal-oxide-semiconductor configuration," *Journal of Applied Physics*, vol. 96, no. 11, pp. 6008–6015, dec 2004.

[111] Q. Xu, B. Schmidt, S. Pradhan, and M. Lipson, "Micrometre-scale silicon electro-optic modulator," *Nature*, vol. 435, no. 7040, pp. 325–327, may 2005.

[112] L. Zhang, J.-Y. Yang, M. Song, Y. Li, B. Zhang, R. G. Beausoleil, and A. E. Willner, "Microring-based modulation and demodulation of DPSK signal," *Optics Express*, vol. 15, no. 18, p. 11564, 2007.

[113] L. Xu, C. Li, C. Wong, and H. K. Tsang, “Optical differential-phase-shift-keying demodulation using a silicon microring resonator,” *IEEE Photonics Technology Letters*, vol. 21, no. 5, pp. 295–297, mar 2009.

[114] Y. D. Chong, L. Ge, H. Cao, and A. D. Stone, “Coherent perfect absorbers: Time-reversed lasers,” *Physical Review Letters*, vol. 105, no. 5, Jul. 2010.

[115] H. Nishihara, M. Haruna, and T. Suhara, *Optical Integrated Circuits*. McGraw-Hill Professional, 1989.

[116] P. Dong, W. Qian, H. Liang, R. Shafiiha, D. Feng, G. Li, J. E. Cunningham, A. V. Krishnamoorthy, and M. Asghari, “Thermally tunable silicon racetrack resonators with ultralow tuning power,” *Optics Express*, vol. 18, no. 19, p. 20298, Sep. 2010.

[117] R. L. Espinola, J. I. Dadap, R. M. Osgood, S. J. McNab, and Y. A. Vlasov, “C-band wavelength conversion in silicon photonic wire waveguides,” *Opt. Express*, vol. 13, no. 11, p. 4341, 2005.

[118] H. Fukuda, K. Yamada, T. Shoji, M. Takahashi, T. Tsuchizawa, T. Watanabe, J.-i. Takahashi, and S.-i. Itabashi, “Four-wave mixing in silicon wire waveguides,” *Opt. Express*, vol. 13, no. 12, pp. 4629–4637, 2005.

[119] M. A. Foster, A. C. Turner, J. E. Sharping, B. S. Schmidt, M. Lipson, and A. L. Gaeta, “Broad-band optical parametric gain on a silicon photonic chip,” *Nature*, vol. 441, no. 7096, pp. 960–963, jun 2006.

[120] X. Liu, B. Kuyken, G. Roelkens, R. Baets, R. M. Osgood, and W. M. J. Green, “Bridging the mid-infrared-to-telecom gap with silicon nanophotonic spectral translation,” *Nature Photonics*, vol. 6, no. 10, pp. 667–671, Sep. 2012. [Online]. Available: http://dx.doi.org/10.1038/NPHOTON.2012.221

[121] J. B. Driscoll, X. Liu, S. Yasseri, I. Hsieh, J. I. Dadap, and R. M. Osgood, “Large longitudinal electric fields (e_z) in silicon nanowire waveguides,” *Opt. Express*, vol. 17, no. 4, p. 2797, feb 2009.

[122] H. Zhou, T. Gu, J. F. McMillan, N. Petrone, A. van der Zande, J. C. Hone, M. Yu, G. Lo, D.-L. Kwong, G. Feng, S. Zhou, and C. W. Wong, “Enhanced four-wave mixing in graphene-silicon slow-light photonic crystal waveguides,” *Appl. Phys. Lett.*, vol. 105, no. 9, p. 091111, Sep. 2014. [Online]. Available: http://dx.doi.org/10.1063/1.4894830

[123] R.-J. Essiambre, M. A. Mestre, R. Ryf, A. H. Gnauck, R. W. Tkach, A. R. Chraplyvy, Y. Sun, X. Jiang, and R. Lingle, “Experimental investigation of inter-modal four-wave mixing in few-mode fibers,” *IEEE Photonics Technology Letters*, vol. 25, no. 6, pp. 539–542, Mar. 2013. [Online]. Available: http://dx.doi.org/10.1109/LPT.2013.2242881

[124] Y.-H. Lin and G.-R. Lin, “Kelly sideband variation and self four-wave-mixing in femtosecond fiber soliton laser mode-locked by multiple exfoliated graphite nano-particles,” *Laser Physics Letters*, vol. 10, no. 4, p. 045109, Mar. 2013. [Online]. Available: http://dx.doi.org/10.1088/1612-2011/10/4/045109

[125] H. Suchowski, K. O'Brien, Z. J. Wong, A. Salandrino, X. Yin, and X. Zhang, “Phase mismatch-free nonlinear propagation in optical zero-index materials,” *Science*, vol. 342, no. 6163, pp. 1223–1226, Dec. 2013. [Online]. Available: http://dx.doi.org/10.1126/science.1244303

[126] R. El-Ganainy, K. G. Makris, M. Khajavikhan, Z. H. Musslimani, S. Rotter, and D. N. Christodoulides, “Non-hermitian physics and pt symmetry,” *Nat. Phys.*, vol. 14, p. 11, 2018.

[127] L. Feng, R. El-Ganainy, and L. Ge, “Non-hermitian photonics based on parity-time symmetry,” *Nat. Photonics*, vol. 11, no. 12, pp. 752–762, 2017.

[128] R. El-Ganainy, J. I. Dadap, and R. M. Osgood, “Optical parametric amplification via non-hermitian phase matching,” *Optics Letters*, vol. 40, no. 21, p. 5086, Oct. 2015. [Online]. Available: http://dx.doi.org/10.1364/OL.40.005086

[129] Q. Zhong, A. Ahmed, J. I. Dadap, R. M. O. JR, and R. El-Ganainy, “Parametric amplification in quasi-pt symmetric coupled waveguide structures,” *New Journal of Physics*, vol. 18, no. 12, p. 125006, 2016. [Online]. Available: http://stacks.iop.org/1367-2630/18/i=12/a=125006

[130] A. Ahmed, X. Meng, J. I. Dadap, R. El-Ganainy, and R. M. Osgood, “Non-hermitian parametric amplification via four wave mixing,” in *Frontiers in Optics 2016*. Optical Society of America, 2016, p. FTu2D.4. [Online]. Available: http://www.osapublishing.org/abstract.cfm?URI=FiO-2016-FTu2D.4

[131] B. E. Little, “A variational coupled-mode theory including radiation loss for grating-assisted couplers,” *J. Lightwave Technol.*, vol. 14, no. 2, pp. 188–195, 1996.

[132] A. Pasquazi, Y. Park, J. Azaña, F. Légaré, R. Morandotti, B. E. Little, S. T. Chu, and D. J. Moss, “Efficient wavelength conversion and net parametric gain via four wave mixing in a high index doped silica waveguide,” *Optics Express*, vol. 18, no. 8, p. 7634, mar 2010.

[133] B. Kuyken, X. Liu, G. Roelkens, R. Baets, J. Richard M. Osgood, and W. M. J. Green, “50 dB parametric on-chip gain in silicon photonic wires,” *Optics Letters*, vol. 36, no. 22, p. 4401, nov 2011.

[134] X. M. Liu, “Broad and tunable multiwavelength fiber laser at the assistance of modulation-instability-assisted four-wave mixing,” *Laser Physics*, vol. 20, no. 4, pp. 842–846, mar 2010.

[135] A. Guo, G. J. Salamo, D. Duchesne, R. Morandotti, M. Volatier-Ravat, V. Aimez, G. A. Siviloglou, and D. N. Christodoulides, "Observation of pt-symmetry breaking in complex optical potentials," *Physical Review Letters*, vol. 103, no. 9, aug 2009.

[136] P. J. Foster, J. K. Doylend, P. Mascher, A. P. Knights, and P. G. Coleman, "Optical attenuation in defect-engineered silicon rib waveguides," *J. Appl. Phys.*, vol. 99, no. 7, p. 073101, apr 2006.

[137] T. K. Liang and H. K. Tsang, "Role of free carriers from two-photon absorption in raman amplification in silicon-on-insulator waveguides," *Appl. Phys. Lett.*, vol. 84, no. 15, pp. 2745–2747, Apr. 2004.

[138] A. D. Bristow, N. Rotenberg, and H. M. v. Driel, "Two-photon absorption and kerr coefficients of silicon for 850-2200nm," *Appl. Phys. Lett.*, vol. 90, no. 19, p. 191104, 2007.

[139] J. B. Driscoll, R. M. Osgood, R. R. Grote, J. I. Dadap, and N. C. Panoiu, "Squeezing light in wires: Fundamental optical properties of si nanowire waveguides," *Journal of Lightwave Technology*, vol. 33, no. 14, pp. 3116–3131, Jul. 2015. [Online]. Available: http://dx.doi.org/10.1109/JLT.2015.2431984

[140] G. P. Agrawal, *Nonlinear Fiber Optics*, 4th ed. Academic Press, 2007.

[141] W. Mathlouthi, H. Rong, and M. Paniccia, "Characterization of efficient wavelength conversion by four-wave mixing in sub-micron silicon waveguides," *Opt. Express*, vol. 16, no. 21, pp. 16 735–16 745, 2008.

[142] K. Inoue, "Four-wave mixing in an optical fiber in the zero-dispersion wavelength region," *J. Lightwave Technol.*, vol. 10, no. 11, pp. 1553–1561, 1992.

[143] O. Liboiron-Ladouceur, "Efficient interconnection for modern computing systems," in *Frontiers in Optics 2014*. OSA, 2014.

[144] A. Mohan, N. P. Saranya, S. B. Johnson, and A. Sangeetha, “Compensation of dispersion in 5 gbps WDM system by using DCF,” in *2014 International Conference on Green Computing Communication and Electrical Engineering (ICGCCEE)*. IEEE, mar 2014.

[145] X. Liu, W. M. J. Green, X. Chen, I.-W. Hsieh, J. I. Dadap, Y. A. Vlasov, and R. M. Osgood, “Conformal dielectric overlayers for engineering dispersion and effective nonlinearity of silicon nanophotonic wires,” *Optics Letters*, vol. 33, no. 24, p. 2889, dec 2008.

[146] V. R. Almeida, Q. Xu, C. A. Barrios, and M. Lipson, “Guiding and confining light in void nanostructure,” *Optics Letters*, vol. 29, no. 11, p. 1209, jun 2004.

[147] L. Zhang, Y. Yue, R. G. Beausoleil, and A. E. Willner, “Flattened dispersion in silicon slot waveguides,” *Optics Express*, vol. 18, no. 19, p. 20529, sep 2010.

[148] L. Zhang, Q. Lin, Y. Yue, Y. Yan, R. G. Beausoleil, and A. E. Willner, “Silicon waveguide with four zero-dispersion wavelengths and its application in on-chip octave-spanning supercontinuum generation,” *Optics Express*, vol. 20, no. 2, p. 1685, jan 2012.

[149] X. Meng, R. R. Grote, J. I. Dadap, N. C. Panoiu, and R. M. Osgood, “Engineering metal-nanoantennae/dye complexes for maximum fluorescence enhancement,” *Optics Express*, vol. 22, no. 18, p. 22018, sep 2014.

[150] M. Petracca, B. G. Lee, K. Bergman, and L. P. Carloni, “Design exploration of optical interconnection networks for chip multiprocessors,” in *2008 16th IEEE Symposium on High Performance Interconnects*. IEEE, 2008.

[151] B. G. Lee, A. Biberman, P. Dong, M. Lipson, and K. Bergman, “All-optical comb switch for multiwavelength message routing in silicon photonic networks,” *IEEE Photonics Technology Letters*, vol. 20, no. 10, pp. 767–769, may 2008.

[152] R. F. Oulton, V. J. Sorger, D. A. Genov, D. F. P. Pile, and X. Zhang, “A hybrid plasmonic waveguide for subwavelength confinement and long-range propagation,” *Nature Photonics*, vol. 2, no. 8, pp. 496–500, jul 2008.

[153] J. B. Driscoll, R. R. Grote, B. Souhan, J. I. Dadap, M. Lu, and R. M. Osgood, “Asymmetric y junctions in silicon waveguides for on-chip mode-division multiplexing,” *Optics Letters*, vol. 38, no. 11, p. 1854, may 2013.

[154] “Intel silicon photonics.” [Online]. Available: https://www.intel.com/content/www/us/en/architecture-and-technology/silicon-photonics/silicon-photonics-overview.html

[155] R. Bruck and O. L. Muskens, “Plasmonic nanoantennas as integrated coherent perfect absorbers on SOI waveguides for modulators and all-optical switches,” *Optics Express*, vol. 21, no. 23, p. 27652, nov 2013.

Appendix

List of Publications

Below is a list of publications based on this thesis in reverse chronological order.

- A. Ahmed, H. Yang, J. M. Rothenberg, B. Souhan, Z. Wang, N. C. Abrams, K. A. Ingold, C. C. Evans, J. M. Hensley, K. Bergman, R. R. Grote, A. P. Knights, J. I. Dadap, and R. M. Osgood, Jr., "Coherent-Perfect-Absorption-based DPSK Demodulator for Silicon Photonics," in IEEE Photonics Conference 2018 (under review).
- A. Ahmed, H. Yang, J. M. Rothenberg, B. Souhan, Z. Wang, N. C. Abrams, K. A. Ingold, C. C. Evans, J. M. Hensley, K. Bergman, R. R. Grote, A. P. Knights, J. I. Dadap, and R. M. Osgood, Jr., "Differential Phase-Shift Keying Demodulation by Coherent Perfect Absorption in Silicon Photonics," Optics Letters (accepted on 10 July, 2018).
- A. Ahmed, X. Meng, Q. Zhong, R. El-Ganainy, J. I. Dadap, R. M. Osgood, Jr., "Non-Hermitian Signal Amplification via Four-Wave Mixing in Silicon Nanowires," Physical Review A (under review).
- A. Ahmed, J. I. Dadap, R. El-Ganainy, R. M. Osgood, Jr., "Non-Hermitian Amplification via Four-Wave Mixing in Silicon Photonics," in APS March Meeting 2018, Bulletin of the American Physical Society, abstract K07.00005.

- A. Ahmed, H. Yang, B. Souhan, Z. Wang, C. Evans, J. M. Hensley, J. I. Dadap, A. P. Knights, R. Grote, and R. M. Osgood, Jr., “Characterization of a Coherent-Perfect-Absorption-based DPSK Demodulator for Si Photonics,” in Frontiers in Optics 2017, OSA Technical Digest (online) (Optical Society of America, 2017), paper FW5A.4.
- Q. Zhong, A. Ahmed, J. I. Dadap, R. M. Osgood, Jr., R. El-Ganainy, “Parametric amplification in quasi-PT symmetric coupled waveguide structures,” New Journal of Physics, vol. 18, pp. 125006(1)- 125006(7), Dec. 2016.
- A. Ahmed, X. Meng, J. I. Dadap, R. El-Ganainy, R. M. Osgood, Jr., “Non-Hermitian Parametric Amplification via Four Wave Mixing,” in Frontiers in Optics 2016, OSA Technical Digest (online) (Optical Society of America, 2016), paper FTu2D.4.
- R. M. Osgood, Jr., J. I. Dadap, A. Ahmed, X. Meng, “New Advances in Nanophotonic Device Physics,” in NANOCOM16 Proceedings of the 3rd ACM International Conference on Nanoscale Computing and Communication, New York, USA.
- J. M. Rothenberg, C. P. Chen, J. J. Ackert, A. Ahmed, A. P. Knights, R. R. Grote, K. Bergman, R. M. Osgood, Jr., “Coherent Perfect Absorption in a Silicon Photonic Ring Resonator,” in Frontiers in Optics 2015, OSA Technical Digest (online) (Optical Society of America, 2015), paper FW3E.3.
- X. Meng, A. Ahmed, J. I. Dadap, K. Bergman, R. M. Osgood, Jr., “Dispersion Engineering of Silicon/Plasmonics Hybrid Optical Interconnections,” in Advanced Photonics 2015, OSA Technical Digest (online) (Optical Society of America, 2015), paper IW2A.2.